UNCLASSIFIED

AD NUMBER

AD877594

NEW LIMITATION CHANGE

TO

Approved for public release, distribution unlimited

FROM

Distribution authorized to U.S. Gov't. agencies and their contractors; Critical Technology; SEP 1970. Other requests shall be referred to U.S. Army Aviation Materiel Laboratories, Fort Eustis, VA 23604.

AUTHORITY

USAAMRDL ltr, 30 Jul 1971

THIS PAGE IS UNCLASSIFIED

AD 877254

AD No. ____
DDC FILE COPY

AD

USAAVLABS TECHNICAL REPORT 70-32B

2400°F UNCOOLED TURBINE/MATERIAL PROGRAM

VOLUME II

AERODYNAMIC AND MECHANICAL DESIGN

By

G. E. Lindstrom
J. J. Rebeske
F. Weber

September 1970

U. S. ARMY AVIATION MATERIEL LABORATORIES
FORT EUSTIS, VIRGINIA

CONTRACT DA 44-177-AMC-183(T)

AiRESEARCH MANUFACTURING COMPANY
A DIVISION OF THE GARRETT CORPORATION
PHOENIX, ARIZONA

This document is subject to special export controls, and each transmittal to foreign governments or foreign nationals may be made only with prior approval of U.S. Army Aviation Materiel Laboratories, Fort Eustis, Virginia 23604.

DDC
RETURNED
B

DISCLAIMERS

The findings in this report are not to be construed as an official Department of the Army position unless so designated by other authorized documents.

When Government drawings, specifications, or other data are used for any purpose other than in connection with a definitely related Government procurement operation, the United States Government thereby incurs no responsibility nor any obligation whatsoever; and the fact that the Government may have formulated, furnished, or in any way supplied the said drawings, specifications, or other data is not to be regarded by implication or otherwise as in any manner licensing the holder or any other person or corporation, or conveying any rights or permission, to manufacture, use, or sell any patented invention that may in any way be related thereto.

DISPOSITION INSTRUCTIONS

Destroy this report when no longer needed. Do not return it to the originator.

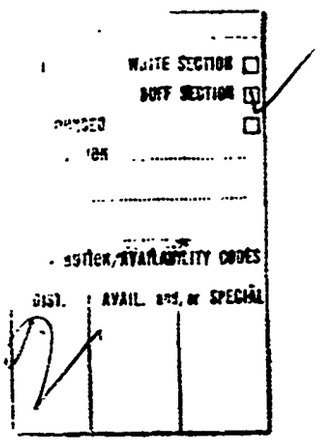

DEPARTMENT OF THE ARMY
HEADQUARTERS US ARMY AVIATION MATERIEL LABORATORIES
FORT EUSTIS, VIRGINIA 23604

The research described herein was conducted by the AiResearch Manufacturing Company, Phoenix, Arizona, under U. S. Army Contract DA 44-177-AMC-183(T). The work was performed under the technical management of Lawrence E. Bell, Jr., Propulsion Division, U. S. Army Aviation Materiel Laboratories.

Appropriate technical personnel of this Command have reviewed the report and concur with the conclusions and recommendations contained herein.

This document is Volume II of a three-volume report and covers the aerodynamic and mechanical design of a 2400°F uncooled turbine component. Volume I covers the high-temperature materials investigations, and Volume III covers the evaluation of a fluidic temperature sensor system.

Task 1G162204A01409
Contract DA 44-177-AMC-183(T)
USAAVLABS TECHNICAL REPORT 70-32B
September 1970

2400°F UNCOOLED TURBINE/MATERIAL PROGRAM

Final Report

VOLUME II

AERODYNAMIC AND MECHANICAL DESIGN

By

G. E. Lindstrom
J. J. Rebeske
F. Weber

Prepared by

AiResearch Manufacturing Company
A Division of The Garrett Corporation
Phoenix, Arizona

for

U. S. ARMY AVIATION MATERIEL LABORATORIES
FORT EUSTIS, VIRGINIA

This document is subject to special export controls, and each transmittal to foreign governments or foreign nationals may be made only with prior approval of U. S. Army Aviation Materiel Laboratories, Fort Eustis, Virginia 23604.

ABSTRACT

In May 1964, a USAAVLABS-sponsored turbine/material research program was initiated by the AiResearch Manufacturing Company of Arizona. The overall program objective was to perform design studies and materials investigations to advance technology for a 2400°F uncooled turbine component. The effort was to culminate in preliminary design of an uncooled turbine stage.

The design activities of the uncooled-turbine program reported in this document (Volume II of the three-volume final report) were conducted concurrently with a materials research activity to document the material-property values of IN-100 and AiResist 13 and also to develop a high-temperature turbine material from intermetallic compositions of beryllide. The mechanical analyses conducted for the turbine design were based on estimates of the IN-100 and beryllide material properties.

Preliminary design studies were conducted to define a number of feasible aerodynamic turbine designs for efficiency comparisons and centrifugal blade stress analyses. From these studies, a candidate turbine design was selected. Preliminary disk-shape studies, thermal analyses, and centrifugal and thermal elastic stress analyses were conducted for each rotor disk of the candidate turbine.

The design determined for the uncooled turbine evaluations was a three-stage axial-flow turbine with an equal work split among the stages. Each turbine rotor was designed for 40 blades, with the first 2 stages using hollow blades of beryllide material attached to IN-100 rotor disks by means of a 2-lobe fir-tree attachment method. The third-stage turbine rotor was designed to be a one-piece casting of IN-100 with integral blades. The first-stage stator was designed as a three-piece-per-vane configuration consisting of a platform, hollow vane, and outer shroud--each piece to be fabricated from beryllide material. It was anticipated that the second-stage stator design would be based on the use of beryllide material and that the third-stage stator material would be IN-100. However, design studies were not conducted for either the second- or third-stage stators. Additional design features include a turbine inlet temperature (TIT) of 2400°F, a rotational speed of 38,000 rpm, an airflow rate of 5.0 pounds per second, a rotor disk cooling-air flow rate of 2.0 percent, a turbine pressure ratio of 9.5:1, and a predicted total-to-total turbine efficiency of 88 percent.

The feasibility of the uncooled turbine design was evaluated by mechanical and thermal studies made on the first-stage turbine components. Extensive thermal and stress studies were conducted to evaluate the mechanical configurations of the rotor blade, disk/blade attachment, and disk, as well as the stator vane and vane attachment.

Design studies for the uncooled turbine were terminated when it became apparent that the proposed beryllide turbine material was inadequate to satisfy design requirements. As reported in Volume I (Materials Research) of the final report, the beryllide compositions that were developed and tested lacked sufficient stress-rupture strength for rotor application and did not possess adequate ductility for either the stator or the rotor application.

FOREWORD

The effort reported herein was conducted by the AiResearch Manufacturing Company under the terms of Contract DA 44-177-AMC-183(T), Task 1G162204A01409.

The analytical, experimental, and development efforts that were conducted under the uncooled turbine program are described in the three volumes of the final report.

Volume I presents the results of material investigations (both USAAVLABS- and company-sponsored) that were conducted to develop a material that would be suitable for the turbine components of a 2400°F uncooled turbine.

Volume II presents the results of the aerodynamic, thermodynamic, and mechanical design activities that were conducted for the design of a 2400°F uncooled turbine.

Volume III presents the results of a test-evaluation program that was conducted to determine the feasibility of a fluidic temperature-sensing system for the measurement of TIT's in a 2400°F gas turbine engine.

The manager of the Small Gas Turbine Engine Project was Mr. D. G. Furst, and the program manager of this uncooled-turbine program was Mr. F. Weber. Principal investigators were Messrs. R. W. Elliott, J. L. Helmbrecht, G. E. Lindstrom, J. J. Rebeske, and A. E. Wilson. The principal engineering consultants were Messrs. R. O. Bullock and E. L. Wheeler. The overall guidance and technical direction provided by Messrs. J. White, H. Morrow, L. Bell, and D. Cale of USAAVLABS are gratefully acknowledged.

TABLE OF CONTENTS

	Page
ABSTRACT	iii
FOREWORD	v
LIST OF ILLUSTRATIONS	ix
LIST OF TABLES	xiv
LIST OF SYMBOLS	xvi
1. INTRODUCTION	1
2. PRELIMINARY DESIGN STUDIES	3
2.1 General Information	3
2.2 Cycle Calculations	4
2.3 Last-Stage Exit Critical Velocity Ratio	5
2.3.1 Effect of Last-Stage Exit Critical Velocity Ratio on Attainable Turbine Efficiency	5
2.3.2 Effect of Last-Stage Exit Axial Velocity and Rotative Speed on Rotor Blade Centrifugal Stress	7
2.3.3 Effect on Disk Stress of Stage Work Coefficient and Number of Stages	13
2.4 Choice of Stage Work Coefficients	14
2.5 Candidate Turbine Designs for Stress and Efficiency Evaluations	17
2.5.1 Stress Evaluations of the Candidate Turbine Designs	17
2.5.1.1 Blade Geometry	19
2.5.1.2 Blade Metal Temperatures	19
2.5.1.3 Material Properties and Blade Attachment Method	20
2.5.1.4 Results of Centrifugal Blade Stress Evaluations	22
2.5.2 Efficiency Evaluations of the Candidate Turbine Designs	22
2.6 Selection of Preliminary Turbine Design	28
2.7 Preliminary Disk Shapes	29
2.8 Preliminary Thermal Analyses - Rotor Disks	34
2.8.1 Phase I Studies	34
2.8.2 Phase II Studies	36
2.9 Preliminary Centrifugal - and Thermal-Stress Analysis	41

Page

3. Final Design and Evaluation 45
3.1 General 45
3.2 Aerodynamic Final Design Activities . . . 45
3.2.1 Gas-Flow-Path Refinement 45
3.2.2 Detailed Stator-Vane Shape 48
3.2.3 Detailed Rotor Blade Shape 48
3.3 Mechanical Studies 53
3.3.1 Rotor--Mechanical Design Studies . . 56
3.3.1.1 Rotor Blade 57
3.3.1.2 Rotor Disk/Blade Attachment 64
3.3.1.2.1 Dovetail Attachment Design and Analyses . . 65
3.3.1.2.2 Fir-Tree Attachment Design and Analyses 69
3.3.1.3 Rotor Disk 75
3.3.2 Stator--Mechanical Design Studies . 80
3.3.2.1 Two-Dimensional Thermal and Thermal-Stress Transient Analyses of the Stator Vane 80
3.3.2.2 Stator-Vane Bending Stress Studies 87
3.3.2.3 Stator-Vane Attachment Studies 87
3.3.2.4 Three-Dimensional Thermal Analyses of the Offset-Hollow Stator Vane . . . 90
3.3.2.5 Multiple-Piece Stator-Vane Studies 93
3.3.2.6 Summation of the Stator Mechanical Studies and Cascade Test Evaluation . . 95

4. Conclusions 96

5. Recommendations 97

APPENDIX I. Generation of Preliminary Blade Profiles 98

APPENDIX II. Method for Estimating Turbine Aerodynamic Efficiency 103

APPENDIX III. Photoelastic Test Program 109

APPENDIX IV. Thermal-Conduction Test Program . . . 131

DISTRIBUTION 137

LIST OF ILLUSTRATIONS

Figure		Page
1	Loss in Attainable Efficiency	8
2	Variation of Flow per Unit of Annular Area and δ_{re} With $\frac{V_x}{a'_{cr}}$	11
3	Rotor Blade Centrifugal Stress Relationship to $\frac{V_x}{a'_{cr}}$	12
4	Typical Hub Vector Diagram and Station Identification	15
5	INCO 713C Stress-Rupture Values	21
6	200-Hour Life Design Stress Level Versus Temperature	21
7	Preliminary Centrifugal Blade Stress Analysis for Exit Stage of Turbine Design A-338-5	23
8	Preliminary Centrifugal Blade Stress Analysis for Exit Stage of Turbine Design A-342-5	24
9	Preliminary Centrifugal Blade Stress Analysis for Exit Stage of Turbine Design A-442-4	25
10	Comparison of Efficiencies for Three Candidate Turbine Designs	27
11	Preliminary Disk Shape and Calculated Centrifugal Stresses of First-Stage Turbine	31
12	Preliminary Disk Shape and Calculated Centrifugal Stresses of Second-Stage Turbine	32
13	Preliminary Disk Shape and Calculated Centrifugal Stresses of Third-Stage Turbine	33

Figure		Page
14	Preliminary Thermal Analysis of First-Stage Rotor	37
15	Preliminary Thermal Analysis of Second-Stage Rotor	38
16	Preliminary Thermal Analysis of Third-Stage Rotor	40
17	Preliminary Centrifugal- and Thermal-Stress Distributions of First-Stage Rotor Disk	42
18	Preliminary Centrifugal- and Thermal-Stress Distributions of Second-Stage Rotor Disk	43
19	Preliminary Centrifugal- and Thermal-Stress Distributions of Third-Stage Rotor Disk	44
20	Representative Vector Diagrams for First-Stage Turbine	47
21	Meridional View of First-Stage Turbine	50
22	First-Stage Stator Vane Shape and Corresponding Surface Velocity Distribution for R = 3.5694 Inches	51
23	First-Stage Stator Vane Shape and Corresponding Surface Velocity Distribution for R = 3.9694 Inches	52
24	First-Stage Rotor Blade Shape and Corresponding Surface Velocity Distribution for R = 3.5694 Inches	54
25	First-Stage Rotor Blade Shape and Corresponding Surface Velocity Distribution for R = 4.1057 Inches	55
26	Rotor Blade Radial Hole Shape and the Calculated Static-Pressure Distribution	58

Figure		Page
27	Calculated First-Stage TIT Variation With Time	59
28	Steady-State Heat-Transfer-Coefficient Distribution and Relative Gas-Temperature Distribution Around the Blade	61
29	Transient Thermal Study of Rotor Blade Section at R = 4.1057 Inches (Blade Tip)	62
30	Transient Temperature and Stress Distribution of Rotor Blade Section at R = 4.1057 Inches (Blade Tip)	63
31	General Configuration, Stress Point Locations, and Pertinent Dimension Locations of Dovetail Attachment	66
32	General Configuration, Stress Point Locations, and Pertinent Dimension Locations of Fir-Tree Attachment	71
33	Temperature Distributions of Rotor With and Without Shim Stock in Place . . .	77
34	Calculated Centrifugal Stresses of Rotor Disk Without Shim in Place	78
35	Calculated Combined Centrifugal and Thermal Elastic Stresses of Rotor Disk Without Shim in Place	79
36	Steady-State Heat-Transfer Coefficient and Relative Gas-Temperature Distributions Around the Stator Vane at Section, R = 3.5694 Inches.	82
37	Transient Thermal Study of Solid Stator Vane at Section, R = 3.5694 Inches	83
38	Stress and Temperature Distributions in Solid Stator Vane at Section, R = 3.5694 Inches	84

Figure		Page
39	Transient Thermal Study of Offset-Hollow Stator Vane at Section, R = 3.5694 Inches .	85
40	Stress and Temperature Distributions in Offset-Hollow Stator Vane at Section, R = 3.5694 Inches	86
41	Locations and Positions of Principal Axis on Offset-Hollow and Solid Stator Vanes at Section, R = 3.5694 Inches	88
42	Stator Attachment Designs	89
43	Assumed Compressor Discharge Temperature Variation With Time	91
44	Three-Dimensional, Steady-State Temperature Distribution in Offset-Hollow Vane and Attachment Configuration B . . .	92
45	Comparison of Two-Dimensional and Three-Dimensional Calculated Temperatures for Offset-Hollow Vane at Points of Maximum Stresses	94
46	Blade Profile Layout	99
47	Turbine Blade Area Distribution Turbine Design A-338-5, Third Stage, Showing Comparison Between Different Numbers of Blades	101
48	Turbine Blade Area Distribution Turbine Design A-338-5, Third Stage, Showing Comparison Between Different TC/CX Ratios .	102
49	Blade Aerodynamic Loading Diagrams . . .	105
50	Attainable Turbine Efficiency	108
51	Layout of Fir-Tree Rotor Disk/Blade Attachment	111
52	Photoelastic Test Model of Fir-Tree Attachment	113

Figure		Page
53	Photoelastic Test Setup of Fir-Tree Attachment Model	114
54	Photoelastic Fringe Pattern Illustrating Higher Load Carried by Lower Lobes (Dark Field)	115
55	Typical Dark-Field Photoelastic Pattern at High Load	117
56	Light-Field Photoelastic Pattern Corresponding to Internal Load Range . .	118
57	Maximum Root Stress Versus Fractional Load (Upper Lobe)	121
58	Model Stress Above Upper Blade Lobes (Load on Upper)	124
59	Model Stress Above Upper Blade Lobes (Load on Lower)	125
60	Model Stress Between Upper and Lower Blade Lobes (Load on Lower).	125
61	Model Stress in Disk Versus Load in Upper Lobes	127
62	Maximum Disk Stress Versus Percentage of Load Carried	128
63	Maximum Blade Stress Between Upper and Lower Lobes and Above Upper Lobes . . .	129
64	Loading Considered in Fir-Tree Analysis .	130
65	Conduction Rig Test Setup	132
66	Thermocouple Installation	133
67	Thermal Conductivity of Beryllide and IN-100	135

LIST OF TABLES

Table		Page
I	Design Activity Sequential Logic Flow Chart	2
II	Nine Candidate Preliminary Aerodynamic Designs	18
III	Summary of Pertinent Turbine-Rotor Data for Turbine Design A-338-5	30
IV	Calculated Values of Thermal Parameters for First- and Second-Stage Analyses	35
V	Calculated Values of Thermal Parameters for Third-Stage Analyses	39
VI	Preliminary Calculations for Margins of Safety	46
VII	Turbine A-338-5 Stage Dimensions	49
VIII	Comparison of Beryllide Physical Properties Estimated and Measured at 800°F	56
IX	Pertinent Dimensions and Calculated Stresses of Dovetail Disk/Blade Attachment, Configuration No. 1	68
X	Pertinent Dimensions and Calculated Stresses of the Optimized Dovetail Disk/ Blade Attachment Design, Configuration No. 8	70
XI	Pertinent Dimensions and Calculated Stresses of Fir-Tree Disk/Blade Attachment, Configuration No. 1	72
XII	Pertinent Dimensions and Calculated Stresses of the Optimized Fir-Tree Attachment Design	73
XIII	SCF Between Upper and Lower Lobes	116
XIV	SCF Between Upper Lobes and Blades	117

Table		Page
XV	Comparison of Thermal Contact Resistance as Measured in Reported Tests With Published Data for Surfaces of Approximately Similar RMS Values	136

LIST OF SYMBOLS

Where the symbol has more than one meaning, the meanings are listed in the order in which they appear in the report.

Symbols

A	cross-sectional area of pertinent neck section of disk/blade attachment
A_A	rotor annulus area, sq in.
a	blade neck thickness in dovetail attachment
a'_{cr}	critical velocity of sound, ft/sec
C	fractional load carried by lower lobes when both pair of lobes are sharing the total blade load
CX	blade axial chord
C_p	specific heat at constant pressure
c	1. parameter obtained from photoelastic studies dovetail type disk/blade attachment and used to obtain the fillet stress from the neck and tang stresses
	2. rotor-tip clearance
D_p	pressure-side diffusion parameter
D_s	suction-side diffusion parameter
D_t	total surface diffusion parameter
d	disk neck thickness in dovetail attachment
E	modulus of elasticity, psi
F	1. total blade load
	2. load carried by lobe pair
F_o	simulated total blade load
g	gravitational constant, ft/sec^2
h	rotor blade height

J	conversion constant, ft-lb/Btu
K	1. ratio of relative tangential velocity to relative velocity
	2. thermal conductivity
K_a	apparent stress concentration factor
K_{eff}	effective stress concentration factor
k	equation constant dependent on tip shroud geometry
L_a	flank length in dovetail attachment
L_d	same as L_a
ℓ	1. dimension in plane of rotation, in.
	2. mean camber-line length of blade section
N	same as c l
n	number of stages
P	1. pressure, psia
	2. load, lb
P_{amb}	ambient pressure, psia
P'_{re}	total pressure at rotor exit
R	1. gas constant, ft-lb/lb-°R
	2. fraction of total load at which the upper lobe pair first become engaged
R_B	location of fillet radius in dovetail attachment
R_D	same as R_B
RT	temperature, °R
R_c	total temperature recovery factor
Re_ℓ	blade row Reynolds number based on camber-line length

R_p	diffuser static-pressure-recovery coefficient
r	radius
r_i	radius of blade section
r_m	rotor mean radius
r_s	radius of suction surface
r_t	rotor-tip radius
s	blade spacing
T	1. temperature
	2. same as c 1
T_{AW}	adiabatic wall temperature
TC	mid-blade thickness
T'_R	total gas temperature relative to the blade
T_S	static gas temperature
T_{amb}	ambient temperature
t	1. time
	2. dimension in axial direction, in.
t_a	leading-edge thickness
t_c	blade camber thickness
t_e	trailing-edge thickness
U	blade speed, ft/sec
U_H	hub tangential velocity, ft/sec
u	tangential direction
V	absolute velocity, ft/sec
V_x	rotor exit axial velocity, ft/sec

W	velocity of gas relative to the blade, ft/sec
w	actual exit flow, lb/sec
x	axial direction
Z	number of blades
α	1. absolute flow angle
	2. coefficient of thermal expansion
	3. dovetail broad angle
β	relative flow angle
γ	ratio of specific heats
ΔH	enthalpy change, Btu/lb
$\Delta\eta$	efficiency increment
η_{3D}	stage efficiency for rotor tip clearance
$\eta_{3D,\ A}$	predicted efficiency with zero tip clearance
θ_t	total trailing-edge momentum thickness
λ	angular separation between the tang and neck stress locations, deg
λ_s	stage work coefficient
ρ	density
ρ_M	blade material density
σ	1. average blade root stress, psi
	2. stress, psi
σ_a	neck stress in disk/blade attachment
σ_f	fillet stress in disk/blade attachment
σ_m	maximum stress where A is determined

σ_t tang stress in disk/blade attachment

Ψ 1. blade stress taper factor

2. angle defining location of maximum tang stress

3. aerodynamic loading coefficient

ω rotational velocity, radians/sec

Subscripts

m refers to model

p refers to prototype

Superscripts

' denotes stagnation conditions

" denotes relative stagnation conditions

1. INTRODUCTION

This document describes the aerodynamic, thermodynamic, and mechanical design activities that were conducted to evolve an acceptable uncooled-turbine design with the following characteristics:

1. TIT - 2400°F
2. Turbine airflow - approximately 5.0 pounds per sec
3. Turbine efficiency total to total (T-T) - 88 percent, total to static (T-S) - 85 percent
4. Turbine stages - 3 to 5
5. Turbine rotational speed - 38,000 to 46,000 rpm
6. Turbine configuration - axial-flow rotors on a common shaft
7. Turbine component materials - IN-100, AiResist 13 and an intermetallic beryllide composition that was concurrently being developed

It was expected that the turbine would eventually be used in a small gas turbine driving an 8:1 to 10:1 compressor and furnishing power for single-shaft engine application. The objectives of this activity were to establish the best design consistent with high efficiency, mechanical considerations, and practicality of manufacture for the uncooled turbine.

Table I presents a sequential logic flow chart that portrays the scope of the overall design activities, shows the interrelationship of the individual tasks, and, in addition, lists the numbers of paragraphs in which applicable discussion can be found in this document.

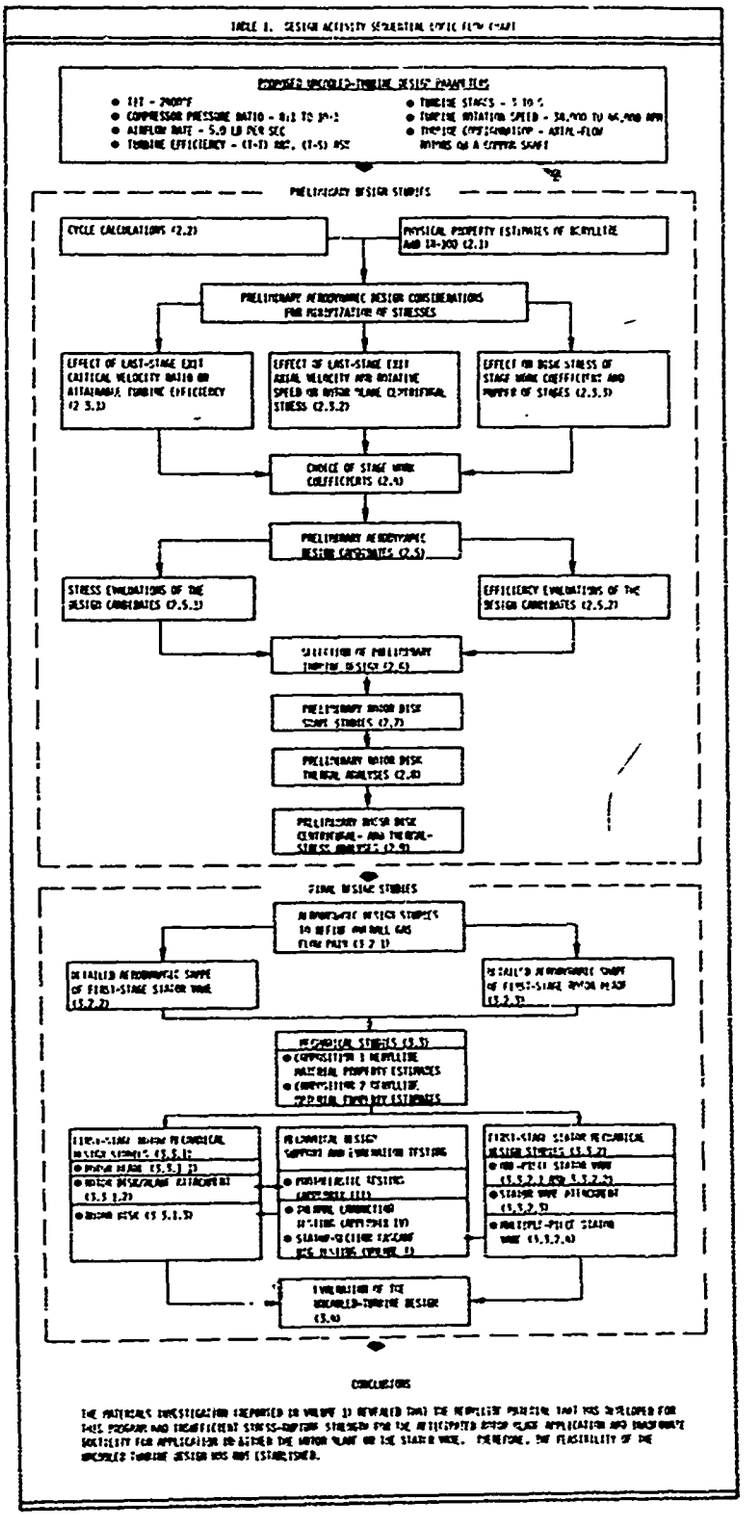
PROPOSED UNCOOLED-TURBINE DESIGN PARAMETERS
• IIT - 2000°F
• COMPRESSOR PRESSURE RATIO - 8:1 TO 10:1
• AIRFLOW RATE - 5.0 LB PER SEC
• TURBINE EFFICIENCY - (T-T) REF. (T-S) ASS
• TURBINE STAGES - 3 TO 5
• TURBINE ROTATION SPEED - 30,000 TO 60,000 RPM
• TURBINE CONFIGURATION - AXIAL-FLOW
PRELIMINARY DESIGN STUDIES
CYCLE CALCULATIONS (2.2)
PHYSICAL PROPERTY ESTIMATES OF BERYLLIUM AND IN-100 (2.3)
PRELIMINARY AERODYNAMIC DESIGN CONSIDERATIONS FOR EXTRAPOLATION OF STRESSES
EFFECT OF LAST-STAGE EXIT CRITICAL VELOCITY RATIO ON ATTAINABLE TURBINE EFFICIENCY (2.3.1)
EFFECT OF LAST-STAGE EXIT AXIAL VELOCITY AND ROTATIVE SPEED ON ROTOR BLADE CENTRIFUGAL STRESS (2.3.2)
EFFECT ON DISK STRESS OF STAGE WORK COEFFICIENT AND NUMBER OF STAGES (2.3.3)
CHOICE OF STAGE WORK COEFFICIENTS (2.4)
PRELIMINARY AERODYNAMIC DESIGN CANDIDATES (2.5)
STRESS EVALUATIONS OF THE DESIGN CANDIDATES (2.5.1)
EFFICIENCY EVALUATIONS OF THE DESIGN CANDIDATES (2.5.2)
SELECTION OF PRELIMINARY TURBINE DESIGN (2.6)
PRELIMINARY ROTOR DISK STRESS STUDIES (2.7)
PRELIMINARY ROTOR DISK THERMAL ANALYSES (2.8)
PRELIMINARY ROTOR DISK CENTRIFUGAL- AND THERMAL-STRESS ANALYSES (2.9)
FINAL DESIGN STUDIES
AERODYNAMIC DESIGN STUDIES TO REFINE AND DEFINE GAS FLOW PATH (3.2.1)
DETAILED AERODYNAMIC SHAPE OF FIRST-STAGE STATOR VANE (3.2.2)
DETAILED AERODYNAMIC SHAPE OF FIRST-STAGE ROTOR BLADE (3.2.3)
MECHANICAL STUDIES (3.3)
• COMPOSITION 1 BERYLLIUM MATERIAL PROPERTY ESTIMATES
• COMPOSITION 2 BERYLLIUM MATERIAL PROPERTY ESTIMATES
FIRST-STAGE ROTOR MECHANICAL DESIGN STUDIES (3.3.1)
• ROTOR BLADE (3.3.1.1)
• ROTOR DISK/BLADE ATTACHMENT (3.3.1.2)
• ROTOR DISK (3.3.1.3)
MECHANICAL DESIGN SUPPORT AND EVALUATION TESTING
• POST-FABRICATION TESTING (ANTICIPATED)
• ENGINE CONNECTED OPERATING EXPERIENCE (?)
• STATOR-VEHICLE VIBRATION DYNAMIC RESPONSE (OPTIONAL)
FIRST-STAGE STATOR MECHANICAL DESIGN STUDIES (3.3.2)
• END-PIECE STATOR VANE (3.3.2.1 AND 3.3.2.2)
• STATOR VANE ATTACHMENT (3.3.2.3)
• MULTIPLE-PIECE STATOR VANE (3.3.2.4)
EVALUATION OF THE UNCOOLED-TURBINE DESIGN (3.4)
CONCLUSIONS
THE MATERIALS INVESTIGATION REPORTED IN VOLUME II INDICATED THAT THE BERYLLIUM MATERIAL THAT WAS DEVELOPED FOR THIS PROGRAM HAD SUFFICIENT STRESS-RUPTURE STRENGTH FOR THE ANTICIPATED ROTOR BLADE APPLICATION AND SHOWED SUITABILITY FOR APPLICATION AS EITHER THE ROTOR BLADE OR THE STATOR VANE. THEREFORE, THE FEASIBILITY OF THE UNCOOLED TURBINE DESIGN HAS NOT ESTABLISHED.

2. PRELIMINARY DESIGN STUDIES

2.1 GENERAL INFORMATION

The objective of developing an uncooled turbine with design features of 2400°F TIT, 10:1 pressure ratio, and 5.0-pound-per-second airflow required a turbine design that was optimized from a stress standpoint in addition to the development of an advanced turbine material. As reported in Volume I, a materials research program was being concurrently conducted with the turbine design studies to develop a beryllide composition with sufficient material properties for use as a high-temperature turbine material. Since material-property design data were not yet available for the beryllide material, the preliminary design studies placed emphasis on reducing the inherent stress levels in the turbine design. The resulting stress levels then became the objective of the materials research program. It was assumed that the beryllide composition material when developed would be adequate for use in the rotor blades of the first two turbine stages and also for use in the first- and second-stage stators.

Designs for the first- and second-stage rotor disks, all subsequent stage rotors, and all stage stators except for the first two stages were based on the premise that the turbine material would be IN-100. Extensive literature research was conducted to determine the present availability of material properties for IN-100. The results revealed that current stress-rupture data for IN-100 showed considerable scatter. The IN-100 data scatter was found to lie both above and below the current minimum stress-to-rupture values for as-cast INCO 713C. Therefore, it was decided that INCO 713C data would be used for the design studies until such time as reliable IN-100 data became available from the IN-100 materials test program, reported in Volume I. Thus, if IN-100 failed to meet expectations, it would not be unreasonable, from a stress consideration, to substitute as-cast INCO 713C.

The preliminary design studies were directed to define a group of candidate aerodynamic turbine designs, from which one design could be selected on the basis of centrifugal blade stress evaluations and attainable turbine efficiency comparisons.

It was believed that the last stage of the turbine would have the most critical centrifugal blade stress levels. This opinion was based on (1) the assumption that the conventional material of the last-stage components would be more vulnerable than the beryllide material of the upstream stages with respect to estimated stress conditions, and (2), the fact that the last-stage annular area requirement results in greater blade length. Therefore, the preliminary centrifugal blade stress evaluations were conducted on the exit stage only.

To initiate the preliminary design studies, cycle calculations were performed to establish the turbine exit temperature, average gas properties, total-to-ambient pressure ratio, and turbine inlet equivalent flow. The last-stage exit critical velocity and diffuser static-pressure-recovery coefficient were then selected, with consideration given to turbine efficiency loss and to centrifugal stresses related to the resulting exit annulus area established. The number of turbine stages, stage work split, and rotational rpm were then varied to establish the physical size of the turbines and the attendant vector diagrams and hub speeds (i.e., rotor disk rim speeds). Nine candidate preliminary aerodynamic turbine designs were defined by these procedures for further evaluation, comparisons, and finally, selection of one design to critique for final design studies.

2.2 CYCLE CALCULATIONS

Cycle calculations were made to establish the overall requirements of the turbine in terms of turbine flow and work output. A single-spool engine with the following operational cycle for a sea-level standard day was selected:

1. Compressor pressure ratio, 10:1
2. Compressor airflow, 5.0 pounds per second
3. Compressor efficiency, 82 percent (T-T)
4. Turbine rotor disk cooling airflow, 2 percent of compressor airflow
5. Burner pressure loss $\Delta P/P$, 0.05
6. Burner efficiency, 98 percent
7. Lower heating value, 18,400 Btu per pound
8. TIT, 2400°F

9. Turbine efficiency, - (T-T) 88 percent, (T-S) 85 percent

With use of the above-listed cycle parameters, the overall turbine design requirements were calculated to be:

1. Turbine exit temperature, 1381°F

2. Turbine inlet equivalent flow, 1.247 pounds per second

3. Turbine pressure ratio (total-to-ambient), 9.5:1

In addition, a speed range of 30,000 to 42,000 rpm was specified. It was judged that feasible compressor designs could be obtained in this speed range, with the higher speeds being more desirable from the compressor design point of view and the lower speeds being more desirable from a turbine stress point of view.

With these general turbine requirements defined and the speed range specified, turbine studies were made to determine the quantitative dependence of turbine efficiency and last-stage centrifugal blade stress on the choice of exit axial critical velocity ratio, exhaust diffuser static-pressure-recovery coefficient, and rotative speed.

2.3 LAST-STAGE EXIT CRITICAL VELOCITY RATIO

For the subject uncooled-turbine design, selection of the exit-stage critical velocity ratio was made by determining the best compromise between exhaust loss in terms of attainable turbine efficiency and the centrifugal stresses directly related to the rotor exit annulus area. The following subparagraphs detail the studies that were made to select an exit-stage velocity ratio of 0.45.

2.3.1 Effect of Last-Stage Exit Critical Velocity Ratio on Attainable Turbine Efficiency

Any kinetic energy leaving the exhaust plane of a shaft-power engine diffuser exit is considered to be a loss. This loss can be expressed as the ratio of two isentropic available energies across the turbine. First, if it is assumed that a perfect diffuser and infinite area are present, the velocity at the exit plane of the engine can be made zero. For this case, the available energy to the turbine is based on the inlet total-to-ambient pressure. The second is the case where a real diffuser is considered. The isentropic available energy here will be defined by the inlet total-to-exit

total pressure ratio and is smaller than the first case by the real diffuser losses. This pressure ratio can in turn be related to the axial critical velocity ratio at the exit of the turbine and a diffuser static-pressure-recovery coefficient.

For a given TIT and average gas properties, the ratio of the isentropic available energies can be expressed as

$$\frac{\Delta H_{(\text{total-total})}}{\Delta H_{(\text{total-ambient})}} = \frac{C_p T'_{in}\left[1 - \left(\frac{P'_{exit}}{P_{in}}\right)^{\frac{\gamma-1}{\gamma}}\right]}{C_p T'_{in}\left[1 - \left(\frac{P_{amb}}{P'_{in}}\right)^{\frac{\gamma-1}{\gamma}}\right]} \tag{1}$$

The decrease in attainable efficiency on an isentropic basis is therefore

$$\Delta\eta = 1 - \frac{\Delta H_{(\text{total to total})}}{\Delta H_{(\text{total to static})}} \tag{2}$$

For a fixed overall pressure ratio $\frac{P'_{in}}{P_{amb}}$, the total-to-total pressure ratio is

$$\frac{P'_{exit}}{P'_{in}} = \left(\frac{P_{amb}}{P'_{in}}\right)\left(\frac{P'_{exit}}{P_{amb}}\right) \tag{3}$$

The diffuser static pressure recovery as the ratio of the static pressure rise to the difference in total-to-static pressure at the turbine exit is defined as

$$\frac{P_{amb} - P_{exit}}{P'_{exit} - P_{exit}} = R_p \tag{4}$$

and

$$\frac{P'_{exit}}{P_{amb}} = \frac{(P'/P)_{exit}}{1 + R_p\left[\left(\frac{P'}{P}\right)_{exit} - 1\right]} \tag{5}$$

For the condition of no exit swirl, the ratio of the total-to-static pressure at the turbine rotor exit is a function of only the exit axial critical velocity ratio,

$$\frac{P'}{P_{exit}} = \frac{1}{\left[1 - \frac{\gamma-1}{\gamma+1}\left(\frac{V_x}{a'_{cr}}\right)^2\right]^{\frac{\gamma}{\gamma-1}}} \tag{6}$$

Figure 1 shows the decrease in attainable efficiency as a function of exit axial critical velocity ratio for an overall total-to-ambient pressure ratio of 9.5 and a diffuser static-pressure-recovery coefficient $R_p = 0.6$. Experience has shown that this value of R_p is about the maximum value that can be expected for an annular diffuser operating at the turbine exit.

2.3.2 Effect of Last-Stage Exit Axial Velocity and Rotative Speed on Rotor Blade Centrifugal Stress

The average blade-root centrifugal stress may be represented as a function of the rotative speed and exit annular area by the following equation for centrifugal loading:

$$\sigma = \frac{\rho_M \Phi \omega^2 A_A}{24\pi q} \tag{7}$$

where ρ_M = blade material density, lb/cu in.

Φ = blade taper factor, dimensionless

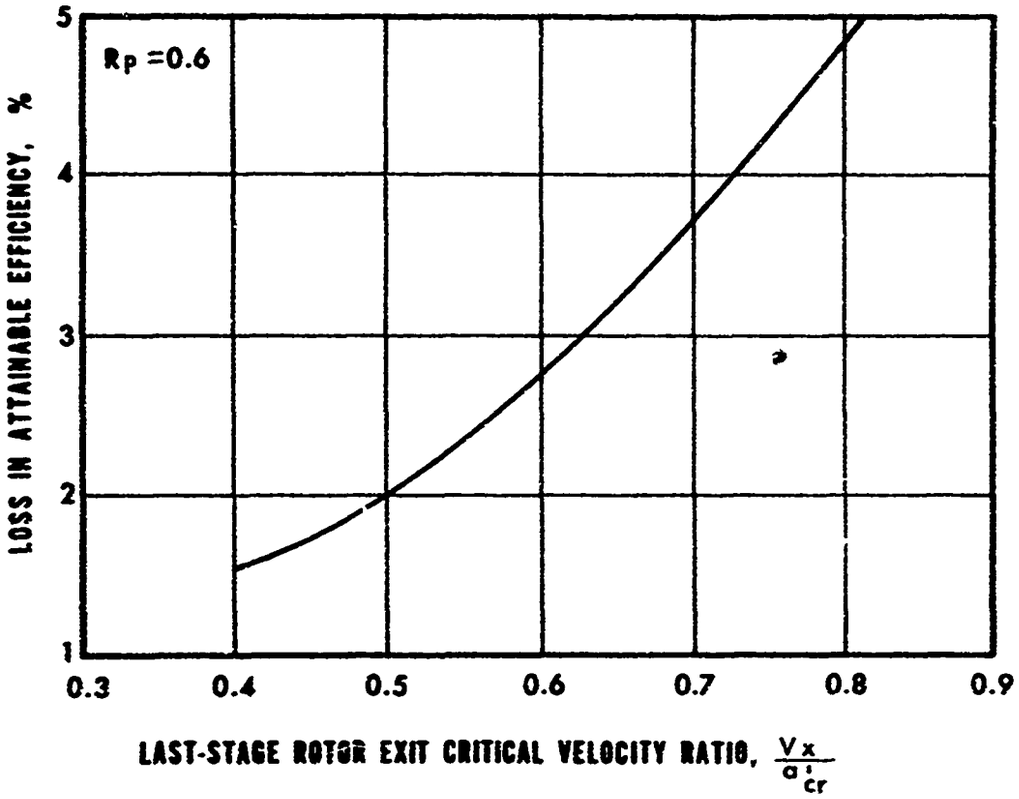

Figure 1. Loss in Attainable Efficiency.

ω = rotational velocity, radians/sec

A_A = rotor annulus area, sq in.

g = acceleration of gravity, ft/sec

σ = average blade root stress, psi

The annular area in this equation can be expressed (again for the case of no exit swirl component of velocity) as a function of the rotor exit axial critical velocity ratio, the diffuser static-pressure-recovery coefficient, and the equivalent flow required at the last-stage rotor exit. The exit equivalent flow required is expressed as

$$\frac{w\sqrt{\theta_e}}{\delta_{re}} \tag{8}$$

where w = actual exit flow, lb/sec

$\delta_{re} = P'_{re}/P_{amb} = f\left(\frac{V_x}{a'_{cr}}\right)$, and R_p

$\theta = T'_e/T_{amb}$

The equivalent flow per unit of area is expressed in terms of $\frac{V_x}{a'_{cr}}$ as follows:

$$\frac{w\sqrt{\theta}}{\delta A_A} = \left[1 - \frac{\gamma-1}{\gamma+1}\left(\frac{V_x}{a'_{cr}}\right)^2_{re}\right]^{\frac{1}{\gamma-1}} \left(\frac{V_x}{a'_{cr}}\right)_{re} \rho'_{std}\, a'_{cr,\,std} \tag{9}$$

where $$a'_{cr,\,std} = \left[\frac{2\gamma}{\gamma+1}\, g\, RT_{std}\right]^{1/2}$$

$$\rho'_{std} = \frac{P_{std}}{R\, T_{std}}$$

For the assumed static-pressure-recovery coefficient of 0.6, Figure 2 shows δ_{re} and $\frac{w\sqrt{\theta}}{\delta A_A}$ as a function of $\frac{V_x}{a_{cr}}$. The required annular area then is simply

$$A_A = \frac{w\sqrt{\theta}_e}{\delta_{re}} \Big/ \frac{w\sqrt{\theta}}{A_A \delta} \tag{10}$$

For assumed values of rpm, blade material density, and blade stress taper factor, it is now possible to obtain the blade root stresses as a function of $\frac{V_x}{a_{cr}}$ at the rotor exit. Such a plot for blade root stress is shown in Figure 3 for a range of rpm, a conventional blade material density of 0.3 pound per cubic inch (the density of INCO 713C), a diffuser recovery factor of 0.6, and an assumed blade taper factor of 0.73.

Figure 3 shows that for any rotative speed, the rotor blade centrifugal stress can be significantly reduced by going to a higher rotor exit critical velocity ratio. Figure 1, however, shows that there is an accompanying decrease in attainable turbine efficiency associated with increasing exit velocity. For this cycle, a two-point decrease in turbine efficiency would decrease the specific power by 8.5 percent or, for a given specific power, increase the inlet temperature by 60°F. Based on these considerations, a value of 0.45 was selected as a reasonable compromise for the rotor exit axial critical velocity ratio despite the indicated higher blade stresses in Figure 3.

It would also appear from Figure 3 that the turbine speed is uniquely defined by the specification of $\frac{V_x}{a_{cr}}$ and a blade centrifugal stress, and to a large extent this is true. However, the blade taper factor ϕ assumes a linear blade profile area variation with respect to radius and can have an effect on the calculated centrifugal stress. For instance, a logarithmic or hyperbolic blade taper would result in reduced centrifugal stress for the same exit velocity and rpm. For this reason, more exact knowledge of the turbine blading is required before the centrifugal stresses can be known for a given exit velocity and rpm.

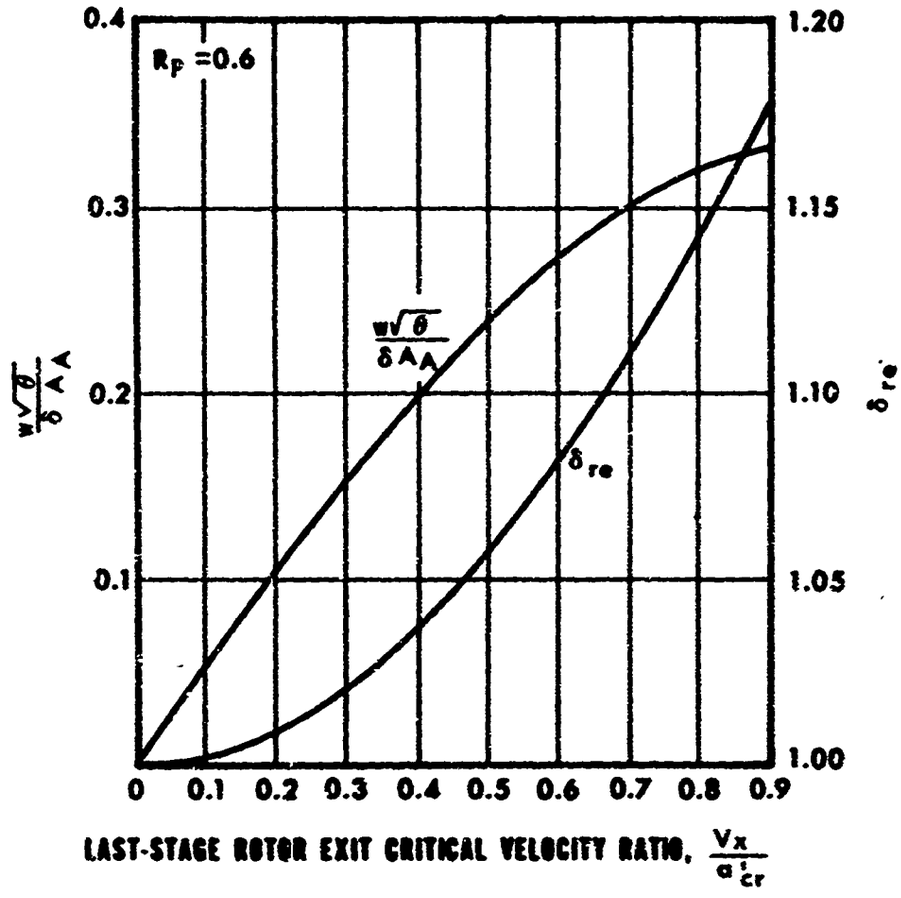

Figure 2. Variation of Flow per Unit of Annular Area and δ_{re} With $\frac{V_x}{a'_{cr}}$.

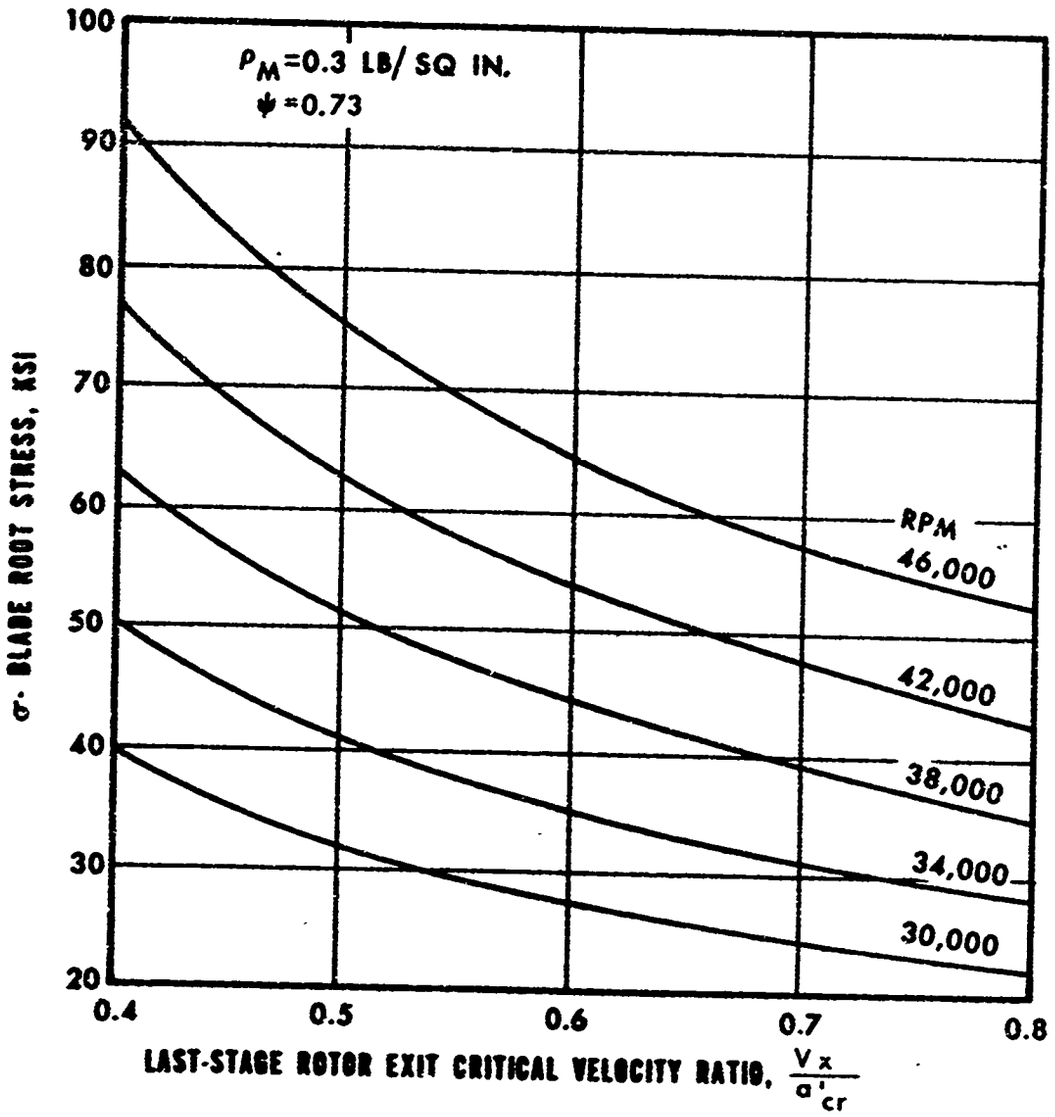

Figure 3. Rotor Blade Centrifugal Stress Relationship to $\frac{V_x}{a'_{cr}}$.

2.3.3 Effect on Disk Stress of Stage Work Coefficient and Number of Stages

The average tangential disk stress is dependent upon (among other factors) the rim load, which is the product of the blade centrifugal stress and the total blade profile area at the rim, and the rim velocity or turbine hub speed. Therefore, lower hub speed would result in a lower disk stress. The hub speed of the turbine for a given work requirement is dependent upon the product of the number of stages and the stage work coefficient. For a turbine of free vortex design and constant hub radius, the total work output can be expressed by:

$$\text{Required work} = gJ\Delta H = U_H^2 \sum_{1}^{n} \lambda_s \qquad (11)$$

where

$\lambda_s = \Delta V_u / U_H$ = stage work coefficient

ΔV_u = change in tangential component of velocity through the rotor

U_H = hub tangential velocity, ft per sec

n = number of stages

or

$$U_H^2 = \text{required work} / \sum_{1}^{n} \lambda_s$$

The work requirement can be met at a given hub velocity either by increasing the stage work coefficient or by increasing the number of stages with a given work coefficient.

Quantitative evaluations of these effects on disk stress, however, required more detailed knowledge of the turbine geometry for a given number of stages and individual stage work coefficients.

2.4 CHOICE OF STAGE WORK COEFFICIENTS

Figure 4 shows a typical vector diagram (nondimensionalized by the hub speed) and station identification. For a constant hub radius from Station 2 to 3 and with assumption of a free-vortex distribution of velocity with respect to radius, the stage work coefficient can be expressed (from Euler's work equation) as

$$\lambda_{stage} = \lambda_{2,H} - \lambda_{3,H} \tag{12}$$

where

$$\lambda_{2,H} = \left(\frac{V_u}{U_H}\right)_{2,H}$$

$$\lambda_{3,H} = \left(\frac{V_u}{U_H}\right)_{3,H} \tag{13}$$

It is also apparent from the vector diagram that

$$\left(\frac{W_u}{U_H}\right)_2 = \left(\frac{V_u}{U_H}\right)_2 - 1 \tag{14}$$

and therefore

$$\lambda_{2,H} = \left(\frac{W_u}{U_H}\right)_2 + 1 \tag{15}$$

and

$$\lambda_{3,H} = \left(\frac{W_u}{U_H}\right)_3 + 1 \tag{16}$$

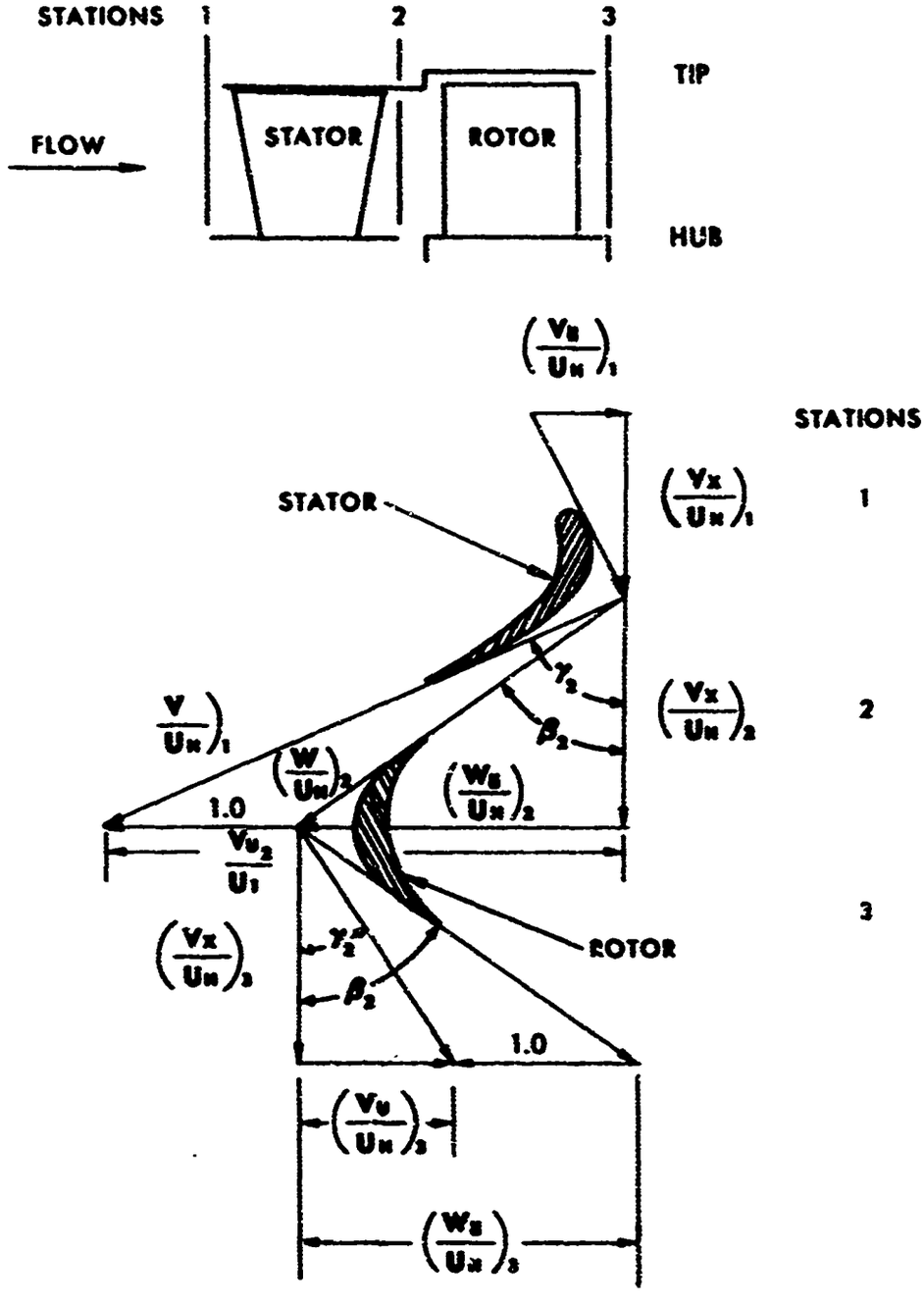

Figure 4. Typical Hub Vector Diagram and Station Identification.

If, for the sake of simplicity, constant axial velocity is assumed at Stations 2 and 3, then the ratio of the relative tangential velocity is the same as the ratio of the relative velocity. Letting K be this ratio, we find that

$$-\left(\frac{W_u}{U_H}\right)_3 = K\left(\frac{W_u}{U_H}\right)_2 \qquad \text{(negative sign required for change in vector direction)} \qquad (17)$$

where

$$K = \left(\frac{W_u}{U_H}\right)_3 \Big/ \left(\frac{W_u}{U_H}\right)_2$$

For $K > 1$, there is an accelerating flow through the rotor--i.e., a reaction design. For $K = 1.0$, the relative velocities entering or leaving the rotor are equal--i.e., an impulse design. For $K < 1.0$, there is a velocity deceleration across the rotor--i.e., a negative reaction design. Without proper boundary-layer control, velocity deceleration across the rotor is to be avoided, since separation is likely to occur, with large attendant losses. In terms of the relative tangential velocities, then, the stage work coefficient is

$$\lambda_s = \left(\frac{W_u}{U_H}\right)_2 (1 + K) \qquad (18)$$

and

$$\lambda_{2,H} = 1 + \frac{\lambda_s}{1 + K} \qquad (19)$$

Now, if we specify zero exit swirl ($\lambda_3 = 0$), then $\lambda_s = \lambda_{2,H}$ and rotor hub impulse conditions (i.e., $K = 1.0$), it then follows that

$$\lambda_s = \lambda_{2,H} = 2.0 \qquad (20)$$

For $\lambda_s > 2.0$ and $K = 1.0$, λ_3 takes on negative values, which decreases the reaction available and increases the turning requirement on the following downstream stator. If the stage is a last stage, the kinetic energy represented by the tangential component of velocity cannot be recovered in an annular diffuser and is therefore a loss. For these reasons, turbines with stage work coefficients greater than 2.0 generally exhibit lower aerodynamic efficiencies than those with stage work coefficients equal to, or less than, 2.0.

Additionally, equal entering and leaving relative velocity at the rotor hub ($K = 1.0$--impulse design) is usually accepted as being a limiting aerodynamic condition that is consistent with good efficiency. Impulse designs can also produce higher work output for a given rotor blade hub speed than can reaction designs.

2.5 CANDIDATE TURBINE DESIGNS FOR STRESS AND EFFICIENCY EVALUATIONS

Nine candidate turbine designs were prepared for centrifugal blade stress and efficiency analyses, from which the most advantageous design was to be selected for final design studies. Based on the reasoning presented in the preceding paragraphs, each of the designs had an exit-stage critical velocity ratio of 0.45 and impulse conditions specified at the rotor blade hubs. Additionally, most of the designs had stage work coefficients of 2.0.

Table II presents a summary of the candidate turbine designs whose gas paths were defined in detail and shows the speed range, number of stages, and stage work coefficients considered.

Subsequent paragraphs report the stress and efficiency analyses that were conducted to select the most advantageous design.

2.5.1 Stress Evaluations of the Candidate Turbine Designs

Before the blade centrifugal stress, stress-rupture life, and average tangential stress in the rotor disk can be accurately determined, a number of variables must be known. Among these variables are an accurate and complete geometrical description of the blade, blade metal temperatures, material properties, and the method by which the blade is attached to the disk. Therefore, prior to initiation of stress evaluations of the candidate designs, efforts were conducted to either determine

TABLE II. NINE CANDIDATE PRELIMINARY AERODYNAMIC DESIGNS

Turbine Design Identification Number	RPM	Stage Number 1	2	3	4	5	$\Sigma\lambda_s$
		Stage Work Coefficients					
A-338-5	38,000	2.0	2.0	2.0	-	-	6.0
A-438-5	38,000	2.0	2.0	2.0	2.0	-	8.0
A-538-5	38,000	2.0	2.0	2.0	2.0	2.0	10.0
A-342-5	42,000	2.0	2.0	2.0	-	-	6.0
A-442-4	42,000	2.0	2.0	2.0	2.0	-	8.0
A-346-4	46,000	2.0	2.0	2.0	-	-	6.0
A-446-5	46,000	2.0	2.0	2.0	2.0	-	8.0
B-338-9	38,000	3.0	3.0	2.0	-	-	8.0
B-338-10*	38,000	3.0	3.0	2.0	-	-	8.0

*Same blade heights as Turbine A-338-5.

or estimate the required information for the subject variables. The following subparagraphs report these efforts and also the results of the stress evaluations.

2.5.1.1 Blade Geometry

A sizable man-hour effort is required to define a complete and suitable three-dimensional blade shape. The procedure is to specify a two-dimensional profile shape of a given radius, determine the surface velocity distribution from a channel flow solution, and subject the profile shape to perturbation until a suitable velocity distribution is obtained. This procedure is repeated at a number of specified radii between the hub and tip shrouds of the flow passage. The two-dimensional profiles are then stacked with their center of gravity on a radial line and faired radially from hub to tip. If a smooth three-dimensional fairing does not result, the procedure is repeated until a smooth three-dimensional shape is evolved. This blade is then further analyzed with a complete three-dimensional flow solution.

Thus, the work involved in completing a three-dimensional blade shape for each of the nine candidate turbine designs for stress analyses would have been prohibitive for this study. Therefore, a method was conceived to generate two-dimensional blade profiles at each radial station uniquely specified by the entering and leaving angles of the local vector diagram and Zweifel's* solidity requirements. The blade section areas were then calculated and integrated, together with their radial moments, to obtain blade volumes and radial centroids as reported in Appendix 1 of this document.

2.5.1.2 Blade Metal Temperatures

In addition to the centrifugal blade stresses calculated based on the blade geometry study discussed above, it was necessary to determine the blade metal temperatures before the blade stress-rupture life could be determined. For this study, the blade metal temperatures were assumed to be equal

---

* Zweifel, O., OPTIMUM BLADE PITCH FOR TURBOMACHINES WITH SPECIAL REFERENCE TO BLADES OF GREAT CURVATURE, Brown Boveri Review, Vol. 37, No. 12, December 1945, pp. 436-444.

to the adiabatic wall temperature at each radial section. A "flat" temperature profile (total gas temperature constant across the annulus) was assumed at the rotor inlet. The adiabatic wall temperature (T_{AW}) was then determined from the static gas temperature (T_S), total gas temperature relative to the blade (T'_R), and an appropriate recovery factor (R_c) at each radial section. The relationship between these quantities is shown below:

$$T'_R = T_S + \frac{W^2}{2gJc_p} \tag{21}$$

$$T_{AW} = T_S + R_c \frac{W^2}{2gJc_p} = T_S + R_c \ (T'_R - T_S) \tag{22}$$

where R_c is equal to the cube root of the Prandtl number for turbulent flow, and the term $\frac{W^2}{2gJcp}$ represents the kinetic energy of the gas relative to the blade.

2.5.1.3 Material Properties and Blade Attachment Method

For the reasons given in Paragraph 2.1 of the preliminary design studies, the centrifugal blade stress analyses were conducted only on the exit stage of the candidate turbine designs. The exit-stage rotor designs for each of the candidate turbines were of a one-piece rotor configuration with integrally cast blades.

INCO 713C material property data were used for the analyses. Stress-rupture values for INCO 713C are presented in the Larson-Miller diagram of Figure 5. The design-life objective of the uncooled turbine was 200 hours at 2400°F first-stage TIT. Substituting a value of 200 hours for the time variable in Figure 5 results in the plot of design stress level versus temperature shown in Figure 6. Included in Figure 6 is the same plot for IN-100 data that was later obtained from the materials test program reported in Volume I.

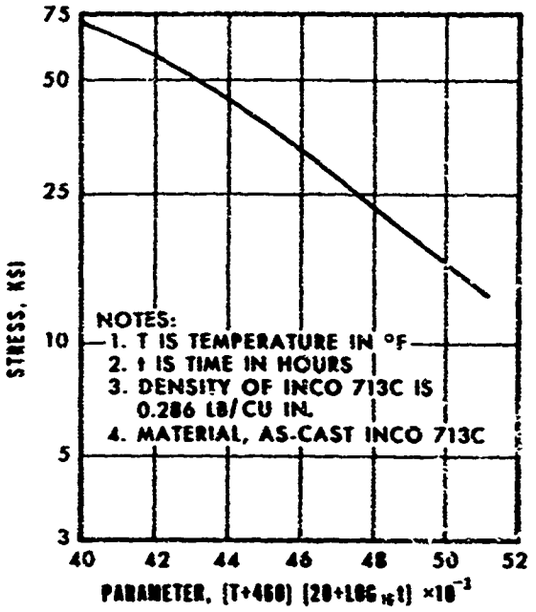

Figure 5. INCO 713C Stress-Rupture Values.

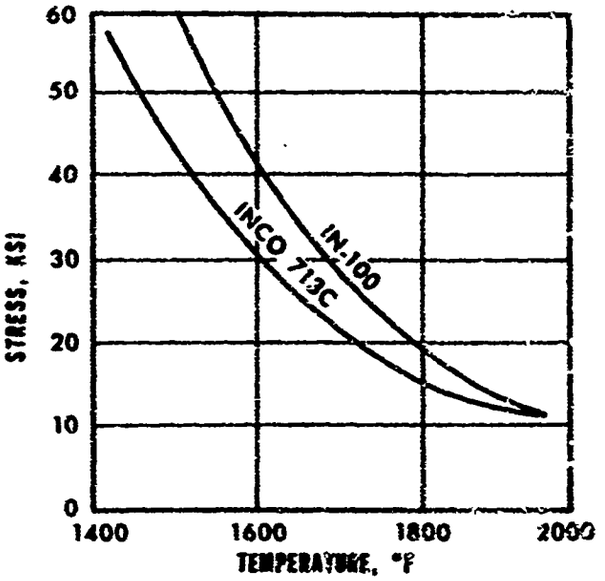

Figure 6. 200-Hour Life Design Stress Level Versus Temperature.

2.5.1.4 Results of Centrifugal Blade Stress Evaluations

The three-stage, equal-work-split, 38,000-rpm turbine (Design A-338-5) was found to have the greatest stress-rupture life (in excess of the 200-hour design goal); thus, from a stress standpoint, it became the most promising configuration. Candidate turbine designs eliminated from further consideration because they did not meet the design life goal were:

1. Design A-342-5
2. Design A-346-4
3. Design A-446-5

Additionally, it was decided to eliminate Design A-442-4. Although the last stage of this four-stage design met the design life goal, the lack of adequate stress margin dictated beryllide blading in the first three stages. The added complexity of an additional stage with beryllide blading and the additional weight of a fourth stage were the reasons for eliminating this design from further consideration. The remaining candidate turbine designs all seemed feasible from a stress standpoint and were submitted for turbine efficiency evaluations.

Representative data for these centrifugal blade stress analyses are shown in Figures 7, 8, and 9 for Designs A-338-5, A-342-5, and A-442-4, respectively.

2.5.2 Efficiency Evaluations of the Candidate Turbine Designs

When the candidate turbine designs were being defined for submittal to stress analyses, an attempt was made to keep blade heights, turning angles, and blockage factors within the regions of known good efficiencies. However, it could not be expected that the various designs would yield identical turbine efficiencies. Therefore, the candidate turbine designs that were determined to be feasible from the centrifugal blade stress analyses (Paragraph 2.5.1) were subjected to turbine efficiency evaluations and comparisons.

It was determined during preliminary evaluations that the five-stage Turbine Design A-538-5 would not provide sufficient efficiency improvements over other candidate designs to offset the disadvantages of the increased weight and additional rotating hardware. Therefore, Turbine Design A-538-5 was

NOTES

1. ROTOR SPEED=38,000 RPM, TIP SPEED=1630 FPS
2. TIP RADIUS=4.9142 IN
3. MATERIAL=INCO 713C, AS CAST
4. INLET TEMPERATURE=1752 °F
5. THIRD STAGE
6. NO. OF BLADES=40

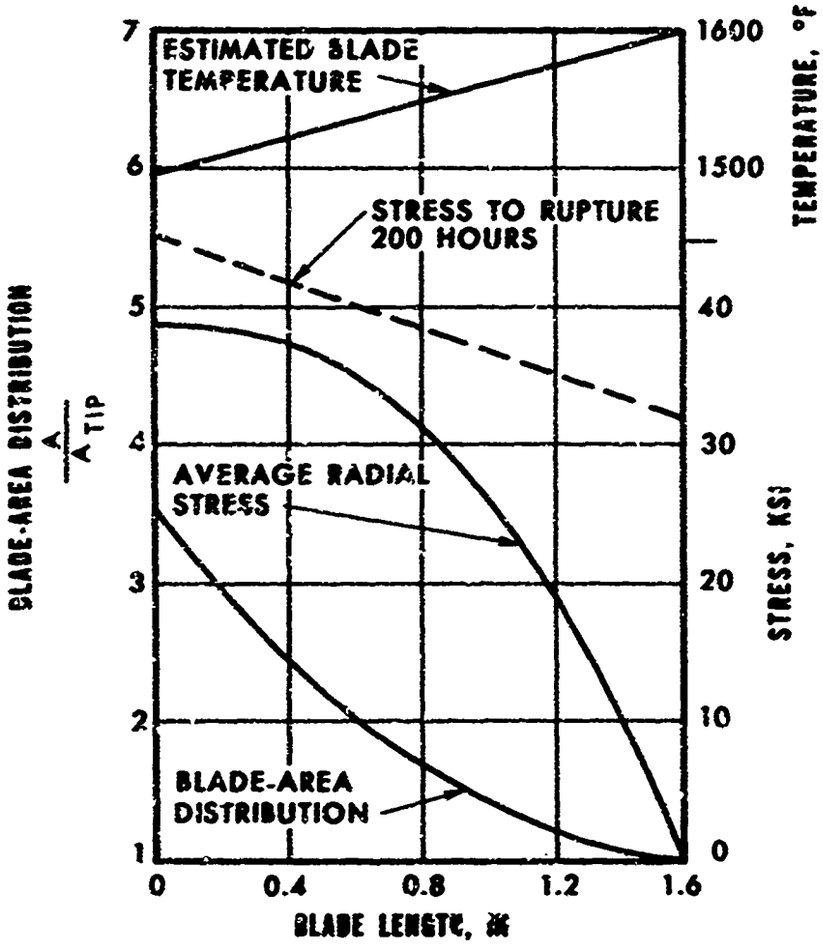

Figure 7. Preliminary Centrifugal Blade Stress Analysis for Exit Stage of Turbine Design A-338-5.

NOTES
1. ROTOR SPEED=42,000 RPM, TIP SPEED=1712 FPS
2. TIP RADIUS=4.6715 IN
3. MATERIAL=INCO 713C, AS CAST
4. INLET TEMPERATURE=1752 °F
5. THIRD STAGE
6. NO. OF BLADES=40

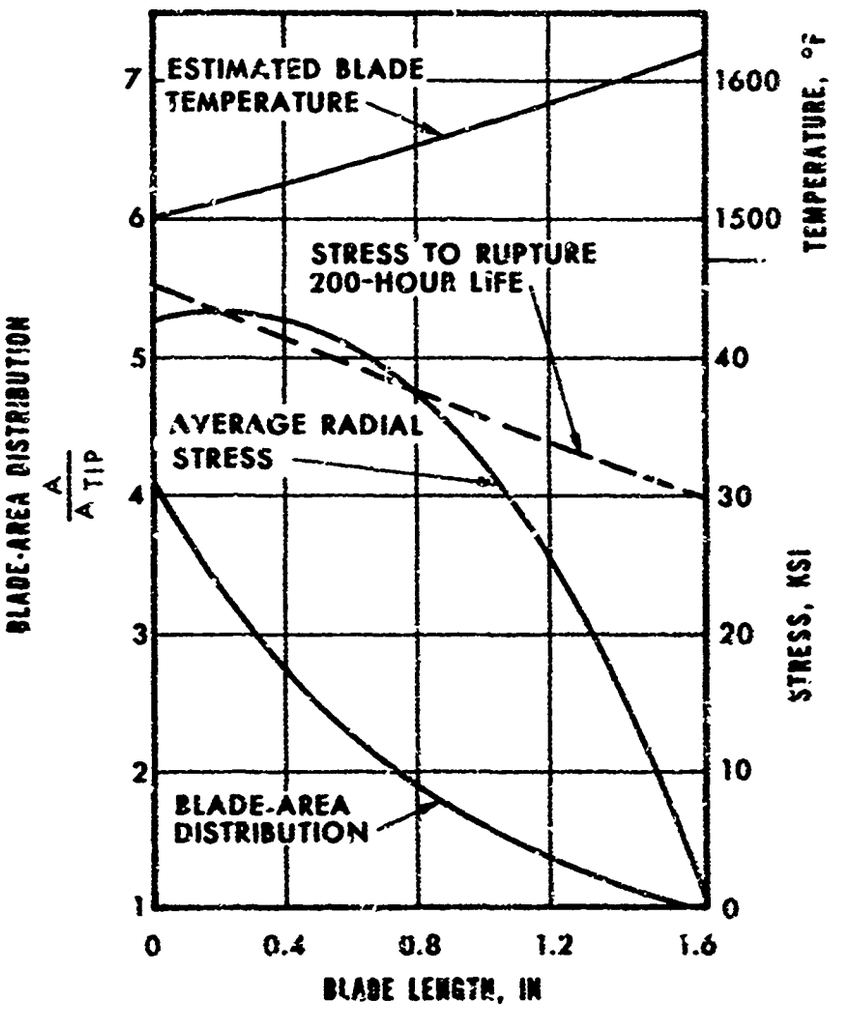

Figure 8. Preliminary Centrifugal Blade Stress Analysis for Exit Stage of Turbine Design A-342-5.

NOTES
1. ROTOR SPEED=42,000 RPM, TIP SPEED=1620 FPS
2. TIP RADIUS=4.421 IN
3. MATERIAL=INCO 713C, AS CAST
4. INLET TEMPERATURE=1672 °F
5. FOURTH STAGE
6. NO. OF BLADES=40

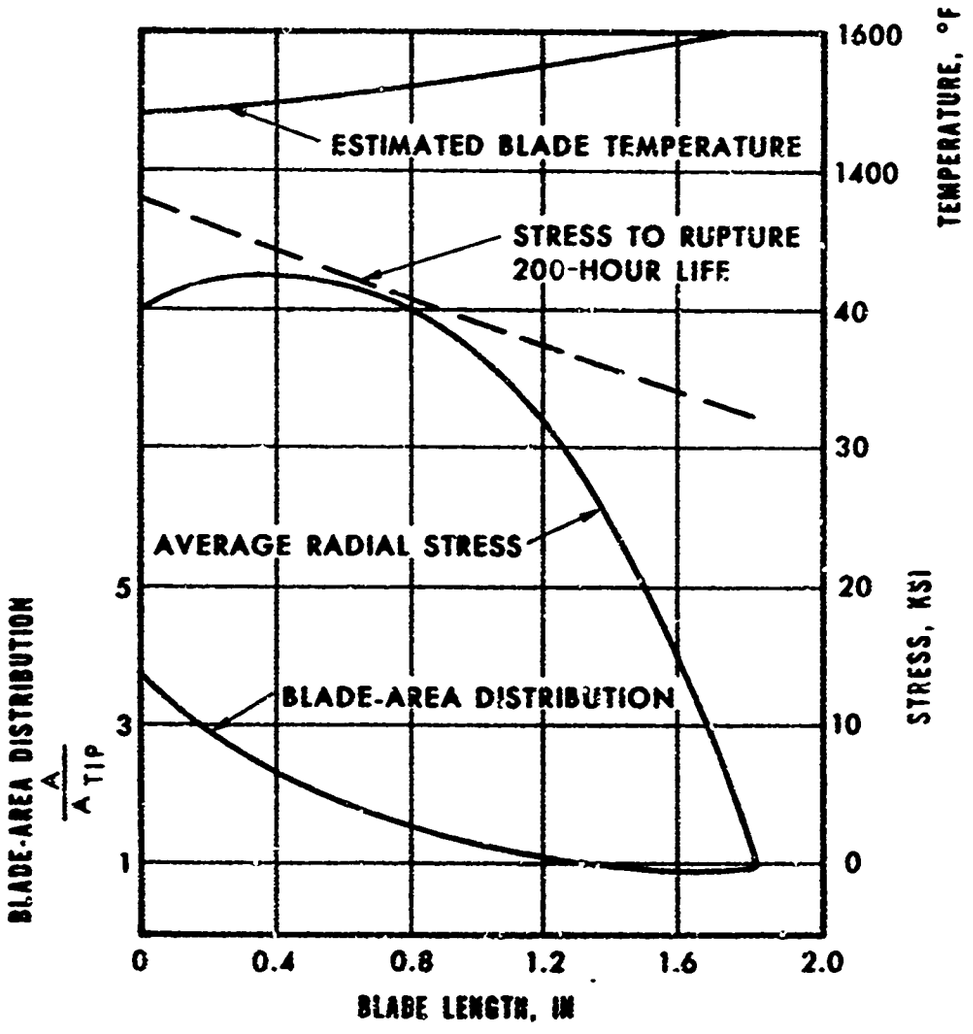

Figure 9. Preliminary Centrifugal Blade Stress Analysis for Exit Stage of Turbine Design A-442-4.

eliminated from further consideration. This elimination, plus eliminations resulting from the stress analyses (Paragraph 2.5.1.4), left only four of the original nine designs as candidates:

1. Turbine Design A-338-5
2. Turbine Design A-438-5
3. Turbine Design B-338-9
4. Turbine Design B-338-10

Preliminary evaluations of the two B-numbered designs revealed that Design B-338-10 afforded greater efficiency potentials. Therefore, comparative efficiency studies were conducted on three candidate designs--A-338-5, A-438-5, and B-338-10. Appendix II presents a summary of the methods that were employed to estimate the aerodynamic efficiency of the turbine designs.

The three aerodynamic turbine designs that were submitted to the efficiency studies incorporated comparative solutions for reducing hub diameters and, consequently, hub speeds, in order to keep centrifugal stresses of the rotors at a minimum. Each of the turbines was designed for a rotor speed of 38,000 rpm. Turbine Design A-338-5 has three impulse hub ($\lambda_s = 2.0$) stages, with a resulting hub radius of 3.319 inches. Turbine Design A-438-5 has four similar stages, with a resulting hub diameter of 2.875 inches. Turbine Design B-338-10 attempts to accomplish four-stage loading in three stages by using negative swirl in the first two stages, and also has a hub diameter of 2.875 inches.

Figure 10 shows comparative total-to-static turbine efficiencies for these three turbines. It can be seen that the four-stage solution (A-438-5) to lower hub radius results in improved turbine efficiency, while the heavy loading of Turbine Design B-338-10 results in lowered efficiency. It may be possible to minimize the performance loss of the highly loaded three-stage turbine (B-338-10) by increasing the blade heights in the first two stages (B-338-10 has the same blade heights as A-338-5). However, the comparative zero-clearance losses and the slight improvement in 0.030-inch clearance loss of A-438-5 over A-338-5 (due to increased blade height) indicate that Turbine Design B-338-10 would still have inferior performance with blade heights as tall as those of A-438-5. Therefore, Turbine Design B-338-10 and, consequently, B-338-9 were eliminated from further consideration.

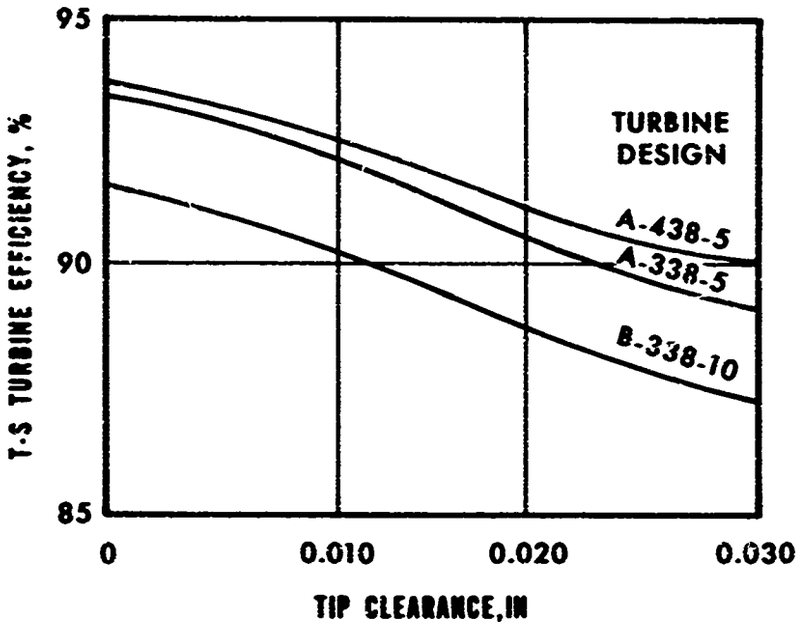

Figure 10. Comparison of Efficiencies for Three Candidate Turbine Designs.

2.6 SELECTION OF PRELIMINARY TURBINE DESIGN

The two most advantageous candidate turbine designs to pursue for final design activities were A-338-5 and A-438-5. In the final analysis, it was decided to use the A-338-5 design because of two factors: (1) the calculated centrifugal blade stresses were lower for Design A-338-5, and (2) the belief that the higher estimated efficiency of A-438-5 did not offset the weight penalty and additional rotational hardware imposed by use of a fourth stage.

The eight preliminary aerodynamic candidate turbine designs that were determined to be less advantageous than Design A-338-5 are listed below with the characteristics that eliminated them from further design considerations.

1. A-438-5, less stress-rupture life than A-338-5 and not enough efficiency improvement to warrant use of a fourth stage.

2. A-538-5, less stress-rupture life than A-338-5 and not enough efficiency improvement to warrant use of a fourth and fifth stage.

3. A-342-5, did not meet the 200-hour stress-rupture design life.

4. A-442-4, marginal 200-hour stress-rupture design life necessitated three turbine stages with beryllide blading plus the disadvantages of four stages.

5. A-346-4, did not meet the 200-hour stress-rupture design life.

6. A-446-5, did not meet the 200-hour stress-rupture design life.

7. B-338-9, less stress-rupture life and efficiency than A-338-5.

8. B-338-10, less stress-rupture life and efficiency than A-338-5.

2.7 PRELIMINARY DISK SHAPES

Two quantities remained to be determined before the turbine disk shapes could be defined: the ratio of mid-blade thickness to axial chord (TC/CX) and the number of rotor blades per stage (see Appendix I). The subject quantities were established by determining a suitable compromise between aerodynamic performance and the centrifugal stress levels in the disk, with consideration given to prior turbine programs where successful fabrication and casting experience had been gained on similar integrally cast and nonintegrally fabricated turbine rotors of the same size. The values of TC/CX that were being considered were 0.15 and 0.20. The number of blades under consideration were 30 and 40.

It was determined that both stress and efficiency were improved by the higher number of blades (40). The thinner blades, TC/CX = 0.15, were determined to be more desirable from a disk stress standpoint but resulted in a slight loss of aerodynamic performance. Six studies were then made to select the final configuration of each disk (see Table III).

For the third-stage disk, two configurations were studied and, as shown in Table III, a blade number of 40 and a TC/CX chord ratio of 0.20 were selected. The thicker chord ratio was chosen in order to gain the additional aerodynamic performance available, as prior experience with integrally cast rotors with the same number of blades and blade thickness and similar operating environment had not resulted in disk stress problems.

As shown in Table III, three configurations were studied for the second-stage disk where both TC/CX and the number of blades were varied to determine the effect on disk sizing. To assure blade spacings large enough to allow for the anticipated fir-tree attachment of the blades to the disk and to attain the best aerodynamic performance, the blade number selected was 40. Because of stress considerations to the attachment, the chord ratio chosen was 0.15. Based on the results of the studies performed on the second-stage disk, only one first-stage disk was considered. As shown in Table III, the blade number for the first stage was 40 and the chord ratio was 0.15.

The disk shapes and centrifugal stress distributions for the first-, second-, and third-stage disks of the selected turbine configuration are presented in Figures 11, 12, and 13, respectively.

TABLE III. SUMMARY OF PERTINENT TURBINE-ROTOR DATA FOR TURBINE DESIGN A-338-5

Pertinent Items	Turbine Stage Number					
	1	2	2	2	3	3
Turbine speed, rpm x 10^{-3}	38	38	38	38	38	38
Stage work split	Equal	Equal	Equal	Equal	Equal	Equal
Chord ratio, TC/CX	0.15	0.15	0.15	0.20	0.15	0.20
Number of blades	40	40	30	40	40	40
Tip diameter, in.	8.116	8.856	8.856	8.856	9.828	9.828
Inlet temperature, °F	2400	2076	2076	2076	1752	1752
Blade height, in.	0.74	1.11	1.11	1.11	1.60	1.60
Maximum blade stress, ksi	9.8	12.6	12.6	12.5	39.0	40.0
Disk weight, lb	7.59	7.89	9.82	10.70	11.01	16.24
Maximum disk stress, ksi	77.0	82.0	77.0	78.0	101.0	103.0
Average tangential disk stress, ksi	44.0	48.5	44.0	45.5	61.5	64.0
Tip speed, ft per sec	1350	1470	1470	1470	1630	1630

Notes:

1. Blade material for the first- and second-stage rotors was considered to be beryllide and for the third-stage rotor was considered to be INCO 713C, as cast.
2. Disk material for all three rotor stages was considered to be INCO 713C, as cast.

NOTES:
1. SPEED=38,000 RPM, TIP SPEED=1350 FPS
2. 40 BLADES
3. TC/CX=0.15
4. BERYLLIDE BLADES, DENSITY 0.118 LB PER CU IN.
5. DISK MATERIAL=INCO 713C. AS CAST
6. INLET TEMPERATURE=2860 °R
7. WEIGHT=7.59 LB
8. AVERAGE TANGENTIAL STRESS=44,000 PSI

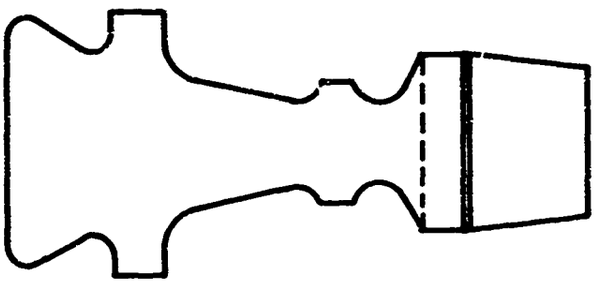

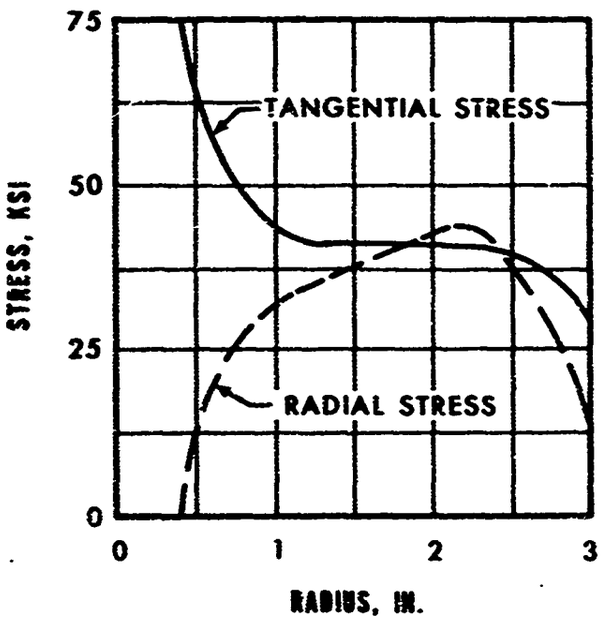

Figure 11. Preliminary Disk Shape and Calculated Centrifugal Stresses of First-Stage Turbine.

NOTES:
1. SPEED=38,000 RPM, TIP SPEED=1470 FPS
2. 40 BLADES
3. TC/CX=0.15
4. BERYLLIDE BLADES, DENSITY 0.118 LB PER CU IN.
5. DISK MATERIAL=INCO 713C, AS CAST
6. INLET TEMPERATURE=2536 °R
7. WEIGHT=7.89 LB
8. AVERAGE TANGENTIAL STRESS=48,500 PSI

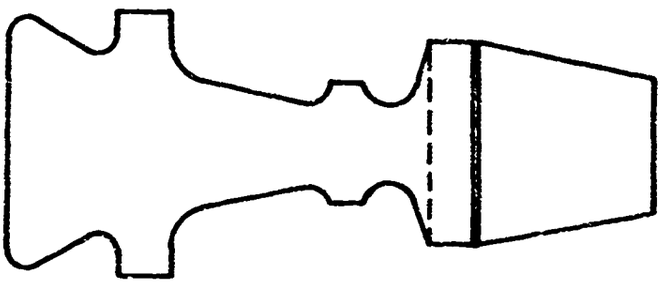

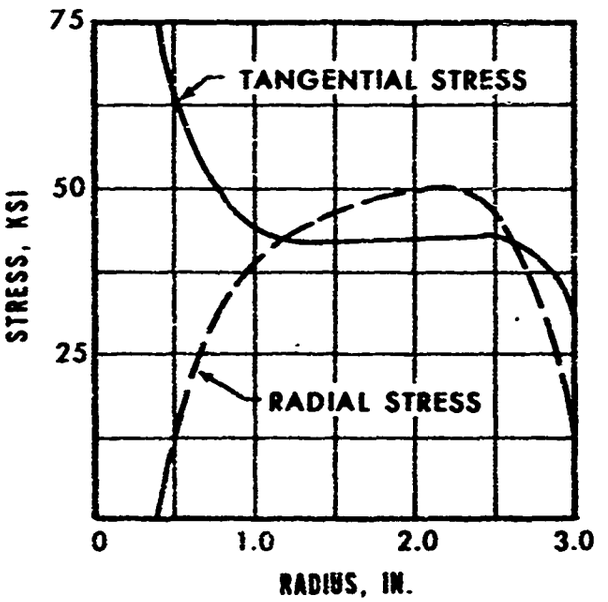

Figure 12. Preliminary Disk Shape and Calculated Centrifugal Stresses of Second-Stage Turbine.

NOTES: 1. SPEED=38,000 RPM, TIP SPEED=1630 FPS
2. 40 BLADES
3. TC/CX=0.20
4. DISK-BLADE MATERIAL=INCO 713C, AS CAST
5. INLET TEMPERATURE=2212 °R
6. WEIGHT=16.24 LB
7. AVERAGE TANGENTIAL STRESS=64,000 PSI

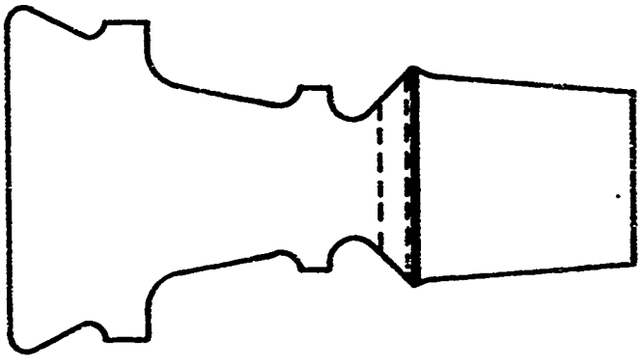

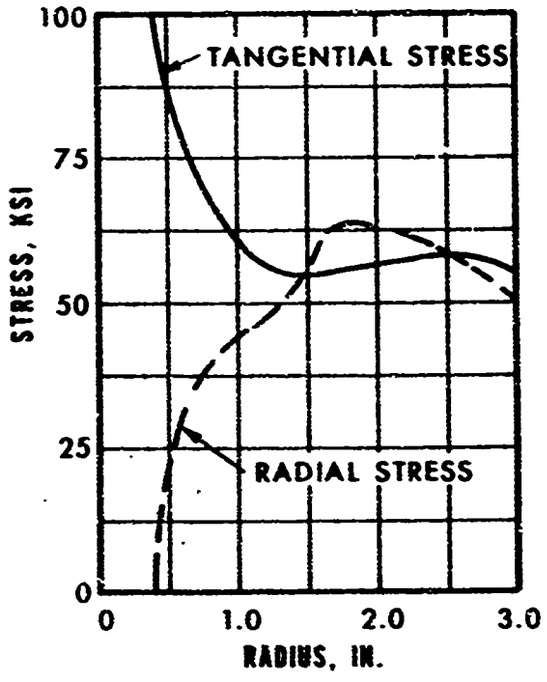

Figure 13. Preliminary Disk Shape and Calculated Centrifugal Stresses of Third-Stage Turbine.

2.8 PRELIMINARY THERMAL ANALYSES - ROTOR DISKS

The preliminary thermal analyses of the rotor disks were conducted in two phases. Phase I studies were made for the first- and second-stage turbine disks, and Phase II studies were made for the third-stage turbine disk.

2.8.1 Phase I Studies

The first- and second-stage turbine disk thermal analyses involved setting up a sector of the rotor disks on an existing steady-state-temperature computer program. The included angle of the rotor disk sectors was simply 360° divided by 40, the number of rotor blades.

Included in the analyses were the effect of thermal radiation between the disk and blade metal surfaces not in direct contact, the surface contact resistance between the disk and blade metal surfaces that were in direct contact, and the changes of the metal physical properties with temperature. Also included were the thermal resistance between the hot gas and the blade, the thermal resistance to heat flowing from the disk to the cooling air, and the thermal capacity of the cooling air.

The cooling air used in the analyses was assumed to be part of the discharge of a compressor group with an overall pressure ratio of 10:1. It was assumed that approximately 2 percent of the compressor through-flow would be required to adequately cool the rotor disks. It was further assumed that a nominal split of the cooling air would be 50 percent for the first stage, 30 percent for the second stage, and 20 percent for the third stage. The cooling-air flow path was the same for each disk and was assumed to enter at the inside diameter (ID) of the disk, to flow out radially with equal distributions over both sides of the disk, and to enter the hot gas stream at the outside diameter (OD) of the disk.

For these studies, the blade material was considered to be beryllide and the disk material was considered to be a nickel-base alloy.

A number of computer analyses were conducted to find the effect on the steady-state disk temperature distributions that variation of each of the following parameters would produce.

1. Cooling-air inlet temperature
2. Cooling-air flow rate
3. Thermal radiation resistances

4. Hot-gas total temperature

5. Thermal resistance between the hot gas and the blade surface

The procedure used was to maintain all the parameters at their calculated values (shown in Table IV) except one, which was varied to determine its effect on the pertinent disk temperatures.

For the analyses, thermal radiation resistances (Item No. 3 above) were calculated from an expression involving the surface emissivity and the view factors between the surfaces. However, since the surface emissivity may vary over a wide range during the life of the turbine as a result of deposits on the metal surfaces, it was considered important that the thermal radiation resistance be one of the variable parameters in the Phase I studies.

TABLE IV. CALCULATED VALUES OF THERMAL PARAMETERS FOR FIRST- AND SECOND-STAGE ANALYSES

Parameter	First Stage	Second Stage
Cooling inlet temperature, °R	1160	1160
Cooling flow rate, percent (total through-flow of engine, 5 lb/sec)	1.0	0.6
Radiation resistance factor	1.0	1.0
Hot-gas total temperature relative to the turbine, °R	2620	2290
Effective heat-transfer coefficient between the turbine and the working fluid, Btu/hr-ft^2-°F	1760	1162

In addition to the analyses that were made varying the subject parameters, analyses were conducted with all the parameters maintained at their calculated values to determine the effect produced by placing nickel shim stock between the mating surfaces of the blade and disk.

It was determined that with the shim in place, the operating temperature of the disk OD is approximately 30° to 40° cooler on both the first- and second-stage disks. In the operational temperature range anticipated for these two turbine disks, a 35° drop in metal temperature would allow an increase in stress level of approximately 5000 psi with no change in stress-rupture life. Also, with the shim stock in place, the temperatures of the first- and second-stage blade shanks increased approximately 30° and 20°, respectively, and the temperature difference between the blade shanks and the disks increased approximately 55°. These temperature changes all produce desirable effects for the subject design. For these reasons, plus the added benefit of having a relatively soft material between the brittle blade material and the disk contact surfaces, it was recommended that the shim be included in the blade-attachment final design and analyses.

Among the parameters of Table IV that were varied for the thermal analyses, the cooling-air flow rate has the greatest effect on engine performance and disk cooling, and can be easily varied in actuality. Therefore, the effect of this parameter on pertinent disk temperatures illustrates the results of the Phase I studies. Figures 14 and 15 show the temperatures at various locations for the first- and second-stage rotors, respectively, with shims assumed in place and as a function of the cooling-air flow rate.

2.8.2 Phase II Studies

The analytical procedure followed during the third-stage thermal analysis was the same as that used for the Phase I studies reported in Paragraph 2.8.1. The parameters that were varied for the third-stage analyses included the following:

1. Cooling-air inlet temperature
2. Cooling-air flow rate
3. Cooling-air heat-transfer coefficients
4. Hot-gas total temperature

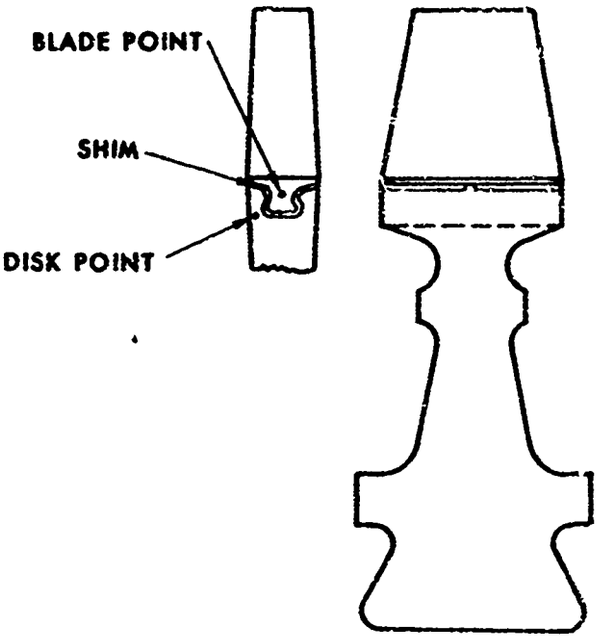

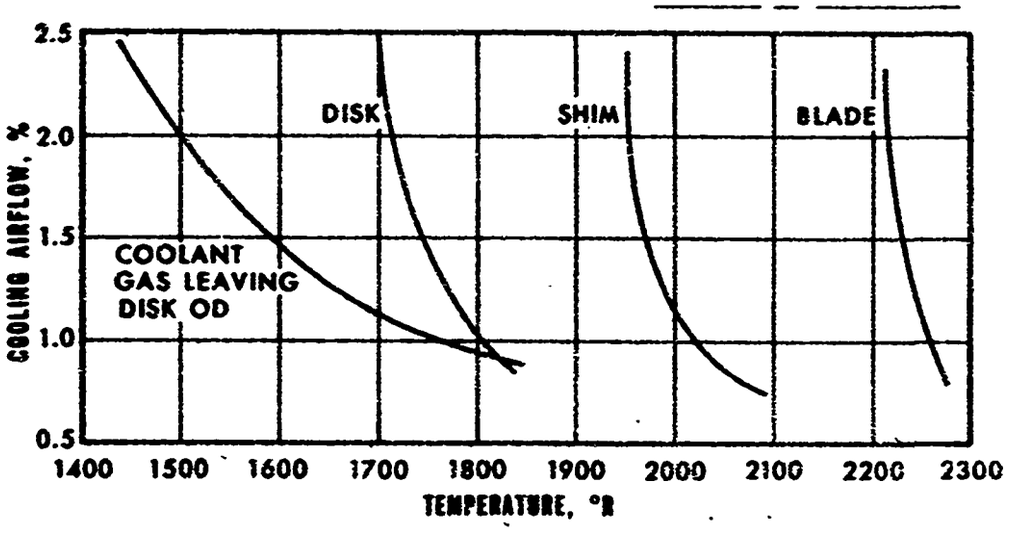

Figure 14. Preliminary Thermal Analysis of First-Stage Rotor.

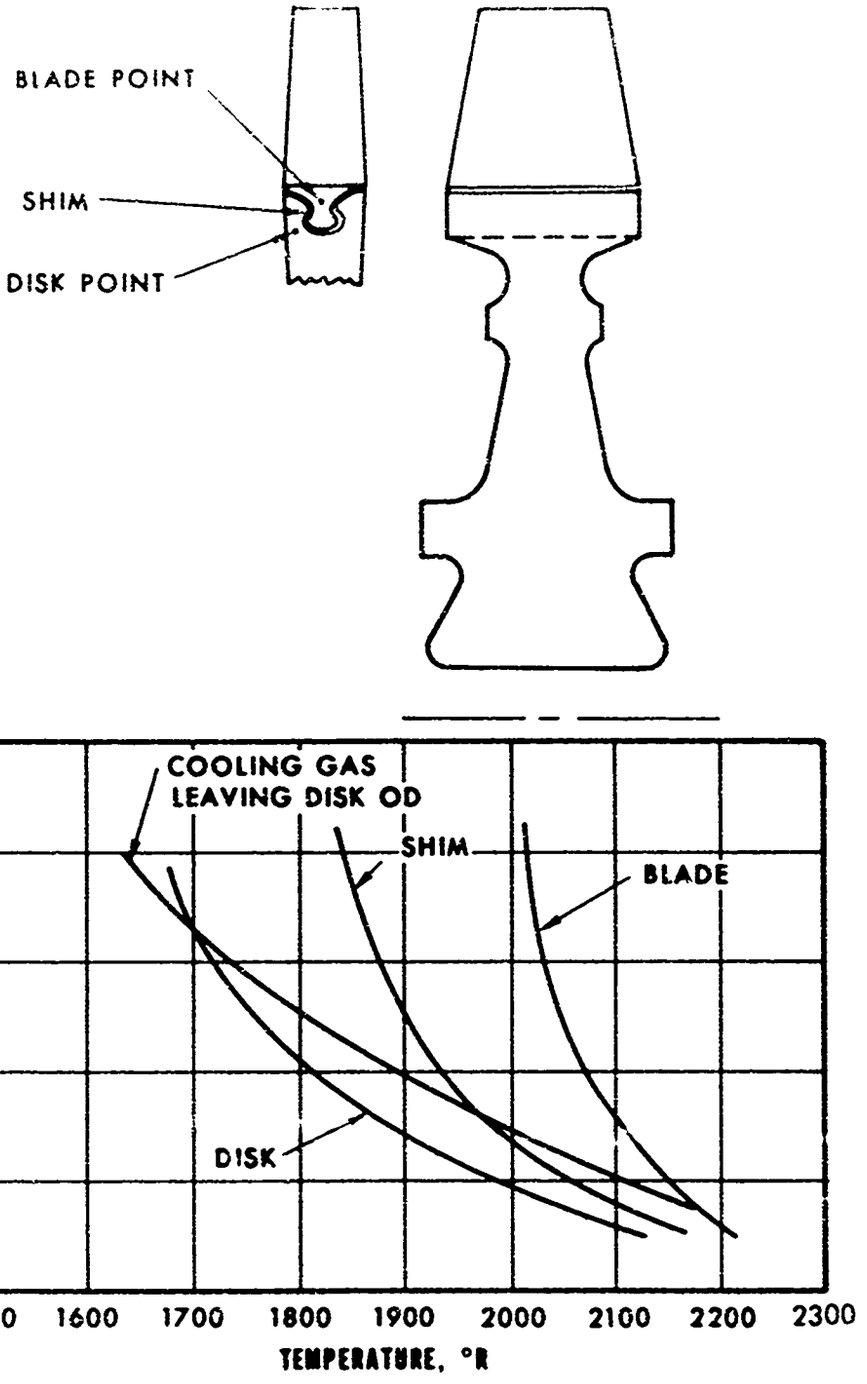

Figure 15. Preliminary Thermal Analysis of Second-Stage Rotor.

- Thermal resistance between the hot gas and the blade surface

The procedure used was to maintain all the parameters at their calculated values (shown in Table V) except one, which was varied to determine its effect on the pertinent disk temperatures.

TABLE V. CALCULATED VALUES OF THERMAL PARAMETERS FOR THIRD-STAGE ANALYSES

Cooling inlet temperature, °R	1160
Cooling flow rate, percent (total through-flow of engine, 5.0 lb/sec)	0.4
Factor applied to the calculated heat-transfer coefficients between the cooling gas and disk sides	1.0
Hot gas total temperature relative to the turbine, °R	1970
Effective heat-transfer coefficient between the turbine and the working fluid, Btu/hr-ft^2-°F	676

The third-stage turbine disk and blades were designed as an integrally cast one-piece rotor of IN-100 material. The shape of the disk was patterned after the TPE331 turbine rotors, with the rim slotted between every blade to reduce the calculated tangential stresses due to thermal effects near the OD of the hub. A hole is drilled through the rotor at the bottom of each slot to reduce the stress concentration that would normally exist at the bottom of the slot.

Again, as in the Phase I studies, the effect of the cooling-air flow-rate parameter illustrates the results of the thermal study. Figure 16 shows the temperature at various locations for the third-stage rotor as a function of the cooling-air flow rate.

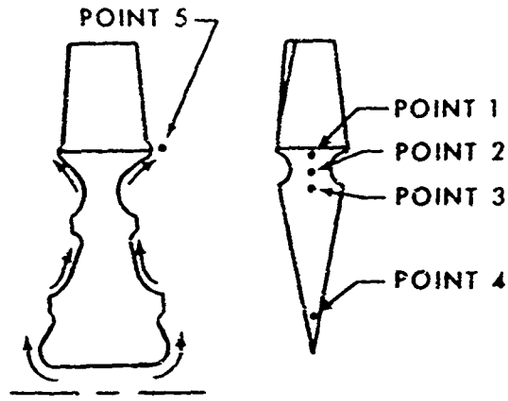

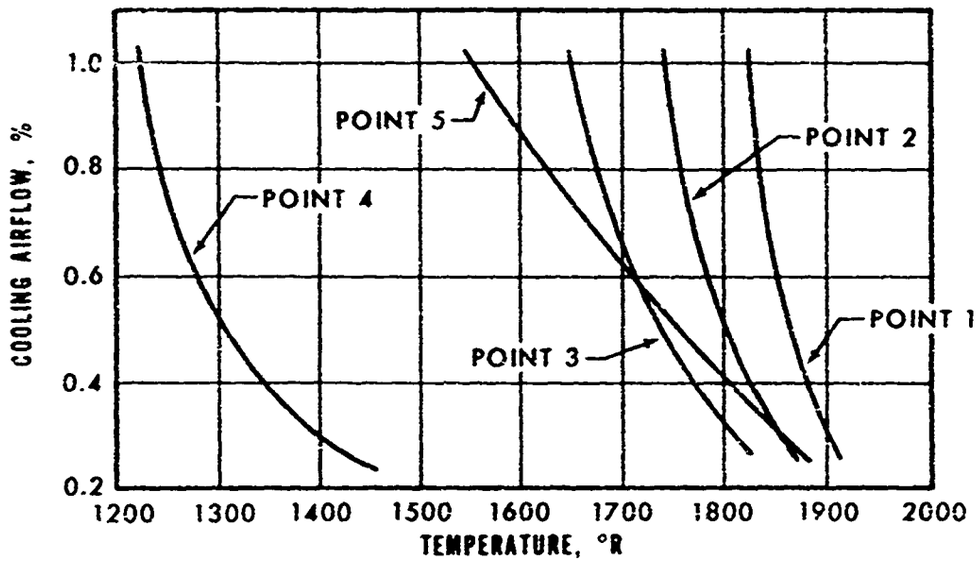

Figure 16. Preliminary Thermal Analysis of Third-Stage Rotor.

2.9 PRELIMINARY CENTRIFUGAL- AND THERMAL-STRESS ANALYSIS

An elastic stress analysis was conducted to calculate the combined thermal- and centrifugal-stress distribution for each turbine disk. The studies revealed a major stress problem in each of the disks, in that the combined thermal and centrifugal stresses that exist near the disk bore of each stage (tangential stress--tensile) and near the blade base of the first-stage disk (tangential stress--compressive) are beyond the yield strength of the material. Figures 17, 18, and 19 present the results of this analysis. Shown on these figures are the combined thermal- and centrifugal-stress distributions, the calculated temperature distributions, and the stress distributions due to centrifugal effects alone.

The thermal stresses represented a problem that required solution. The considerable magnitude of the thermal stresses was the result of the high temperature and the severity of the radial temperature gradients of the rotor disks. The problem, therefore, was to define a cooling-air flow path, or scheme, that would provide a more effective means of disk cooling and produce a more favorable temperature gradient in the disk. As described previously, the cooling air was assumed to enter at the ID of the disk, to flow out radially with equal distributions over both sides of the disk, and to enter the hot-gas stream at the OD of the disk.

Thermal studies on the first-stage disk were initiated to determine a cooling scheme that would reduce the disk temperature levels and thermal gradients without increasing the flow rate of cooling air. As reported in Paragraph 3.3.1.3, these efforts were successful and the resulting disk thermal stresses were within design life limits.

With the exception of the centrifugal stresses near the bore of the third-stage disk (tangential stress), the centrifugal stresses in the disks are well below the yield strength of the material.

With completion of the centrifugal- and thermal-stress analyses, the preliminary design studies were concluded. Efforts were then initiated to complete the final aerodynamic design and to conduct thermal and stress analyses on the anticipated mechanical configurations of the first-stage turbine components.

NOTES:
1. SPEED=38,000 RPM, TIP SPEED=1350 FPS
2. 40 BLADES, TC/CX=0.15
3. TURBINE DISK MATERIAL-INCO 713C,AS CAST
4. INLET TEMPERATURE=2860 °F
5. WEIGHT=7.59 LB
6. AVERAGE TANGENTIAL STRESS=44,000 PSI

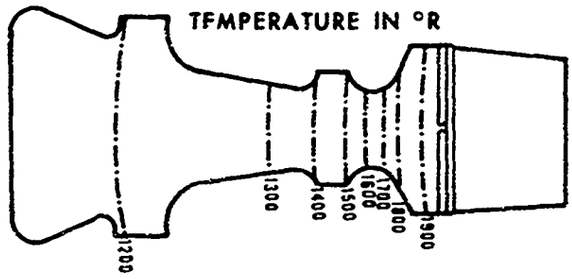

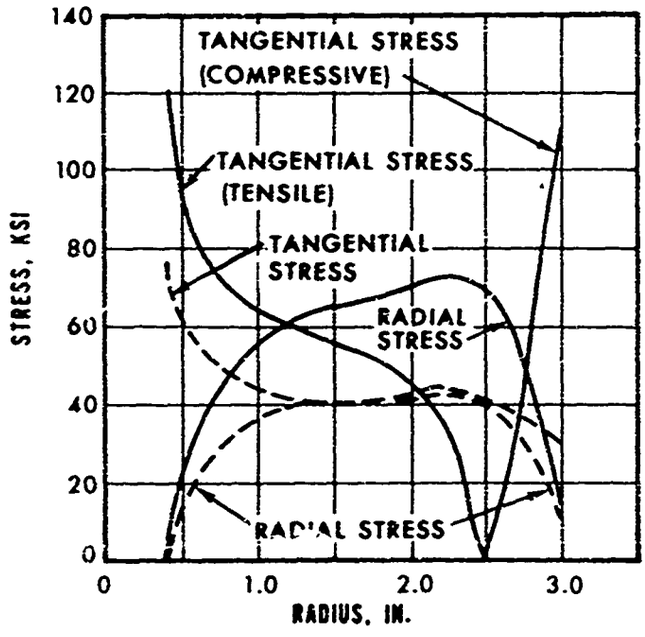

——— COMBINED THERMAL AND CENTRIFUGAL STRESS
— — — — CENTRIFUGAL STRESS ONLY

Figure 17. Preliminary Centrifugal- and Thermal-Stress Distributions of First-Stage Rotor Disk.

NOTES:

1. SPEED=38,000 RPM, TIP SPEED=1470 FPS
2. 40 BLADES, TC/CX=0.15
3. TURBINE DISK MATERIAL=INCO 713C,AS CAST
4. INLET TEMPERATURE=2536 °R
5. WEIGHT=7.89 LB
6. AVERAGE TANGENTIAL STRESS=48,500 PSI

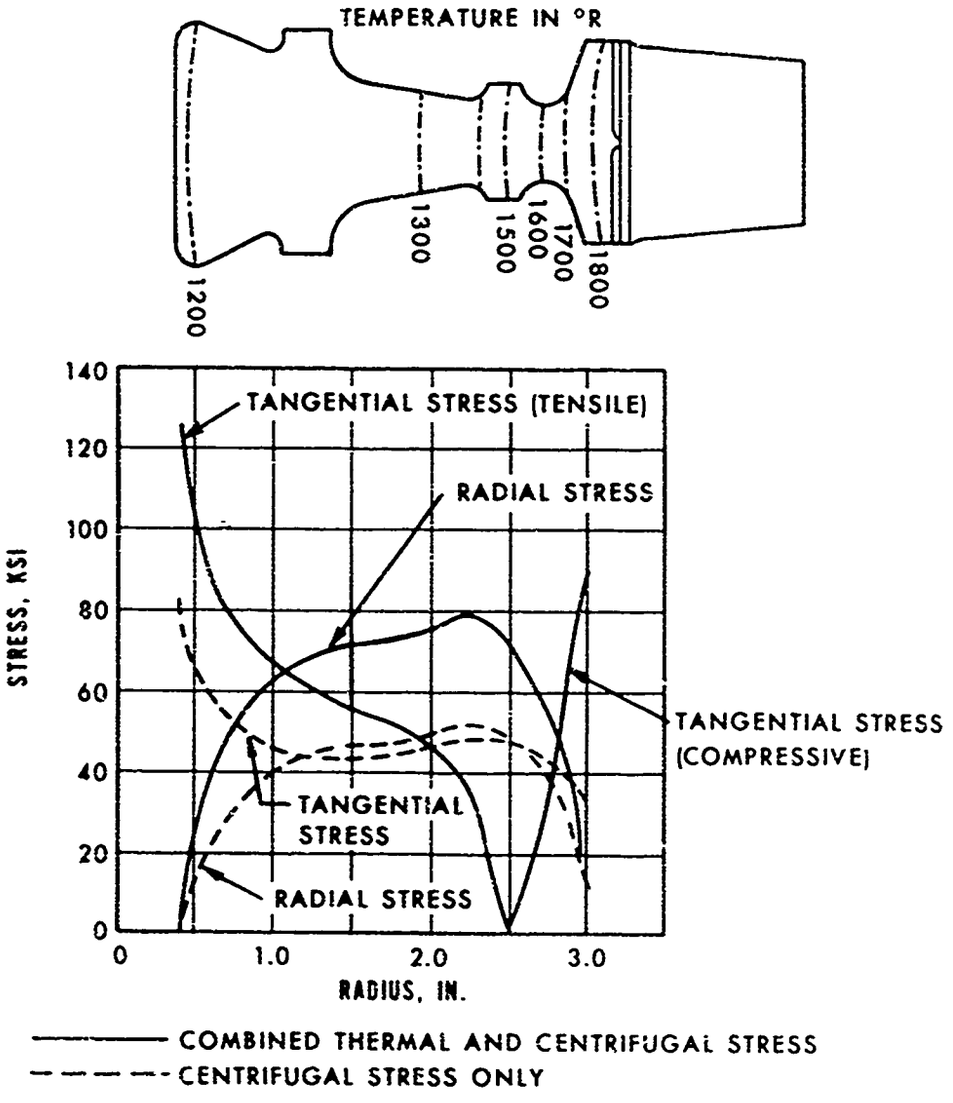

Figure 18. Preliminary Centrifugal- and Thermal-Stress Distributions of Second-Stage Rotor Disk.

NOTES

1. SPEED=38,000 RPM, TIP SPEED=1630 FPS
2. 40 BLADES, TC/CX=0.20
3. TURBINE WHEEL MATERIAL=INCO 713C, AS CAST
4. INLET TEMPERATURE=2212 °R
5. WEIGHT=16.24 LB
6. AVERAGE TANGENTIAL STRESS=64,000 PSI

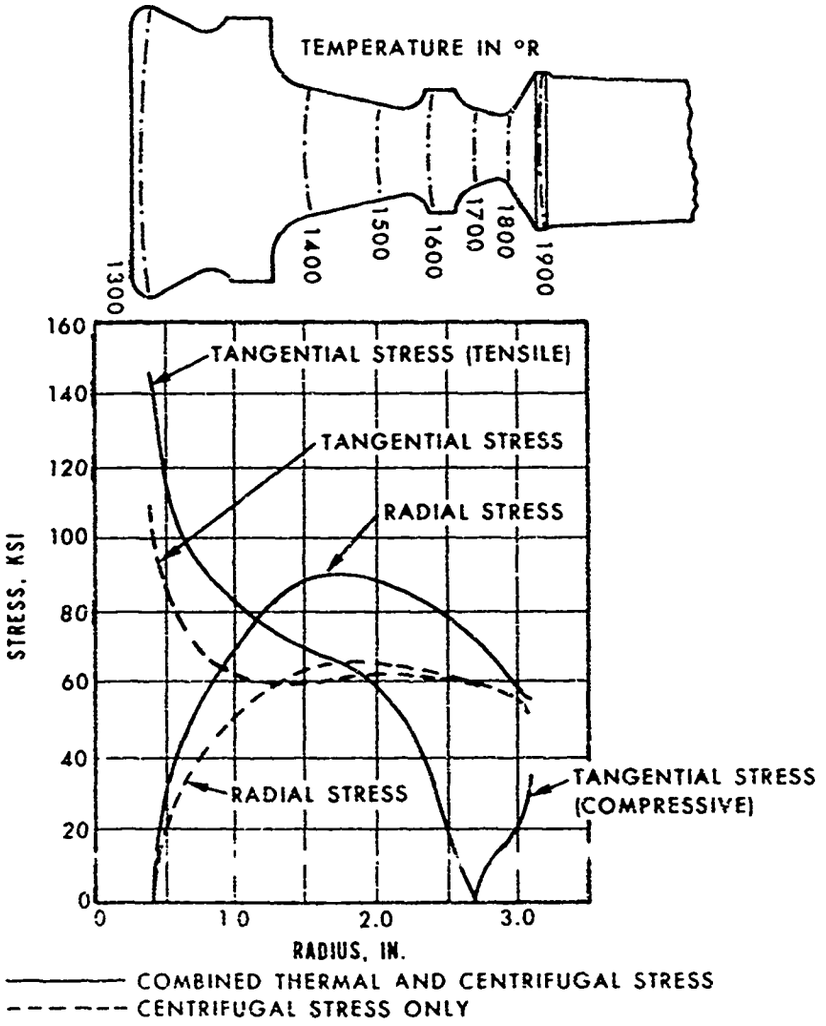

Figure 19. Preliminary Centrifugal- and Thermal-Stress Distributions of Third-Stage Rotor Disk.

3. FINAL DESIGN AND EVALUATION

3.1 GENERAL

Upon completion of the preliminary design studies, calculations were made to determine the preliminary margins of safety for Turbine Design A-338-5. These calculations were based on material-property estimates and data acquired from preliminary material-properties testing and on stress analyses of the preliminary design studies. Table VI presents the calculated stress levels, estimated material strengths, and the calculated margins of safety.

The final design activities were initiated with aerodynamic analyses to establish the first-stage turbine stator-vane and rotor-blade detailed shapes and to refine the overall gas-flow path of Turbine Design A-338-5. Mechanical studies were then conducted to determine the most advantageous structural configuration of the first-stage turbine components without affecting the established airfoil shapes, and to analyze the final component configurations for two potential failure modes--stress rupture and low-cycle fatigue. Results of these activities are reported on the following pages.

3.2 AERODYNAMIC FINAL DESIGN ACTIVITIES

Aerodynamic design studies were conducted to refine the overall gas-flow path of Turbine Design A-338-5 and to define the detailed stator vane and rotor blade shapes for the first-stage turbine components. Further aerodynamic studies were to be performed when the mechanical studies were completed and anticipated results of the cascade testing (reported in Volume I) were known.

3.2.1 Gas-Flow-Path Refinement

New vector diagrams were made for the A-338-5 three-stage turbine design to reflect the lower loss coefficients obtained from a blading efficiency analysis. Representative vector diagrams for the first-stage turbine stator and rotor are shown in Figure 20.

The hub and tip diameters of the stators and rotors of each of the three stages were revised slightly so that for normal machining and assembly tolerances, each succeeding stator and rotor would be smaller in diameter. This ensured that a "step-up" in flow would not occur through the stages that

TABLE VI. PRELIMINARY CALCULATIONS FOR MARGINS OF SAFETY

Location	Stress (psi)	Temp (°F)	Strength (psi)	Margin of Safety (M.S.)
First-Stage Turbine				
Blade root (beryllide)	10,000	2140	23,000 SR	1.3
Blade attachment (beryllide)	17,500	1900	37,000 SR	1.1
Disk attachment (INCO 713C)	17,500	1450	50,000 SR	1.85
Disk average tangential stress (INCO 713C)	44,000	1200	85,000 YS	0.93
Second-Stage Turbine				
Blade root (beryllide)	13,000	1820	43,000 SR	2.31
Blade attachment (beryllide)	28,000	1640	50,000 SR	0.78
Disk attachment (INCO 713C)	28,000	1550	70,000 SR	1.5
Disk average tangential (INCO 713C)	48,500	1200	85,000 YS	0.75
Third-Stage Turbine				
Blade root (INCO 713C)	39,000	1500	47,000 SR	0.20
Disk average tangential (INCO 713C)	64,000	1200	85,000 YS	0.32

NOTES:

1. M.S. = $\frac{\text{strength}}{\text{stress}} - 1$.
2. YS = material yield strength at temperature.
3. SR = material stress-rupture strength at temperature for 200-hour life.
4. The strength levels chosen for beryllide parts are based on the anticipated strength levels that would be achieved in the final beryllide alloy. There is sufficient range in the present design to allow for as much as a 50-percent reduction in stress level in the beryllide parts and still maintain a satisfactory margin of safety in the disk portions of the turbines.
5. Rotational speed = 38,000 rpm.

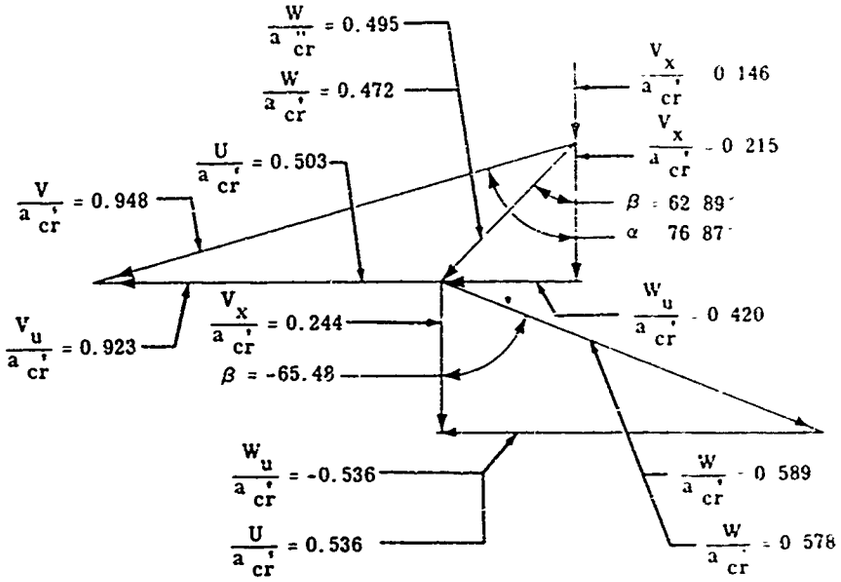

STATOR VECTOR DIAGRAM, R = 3.5694 IN.

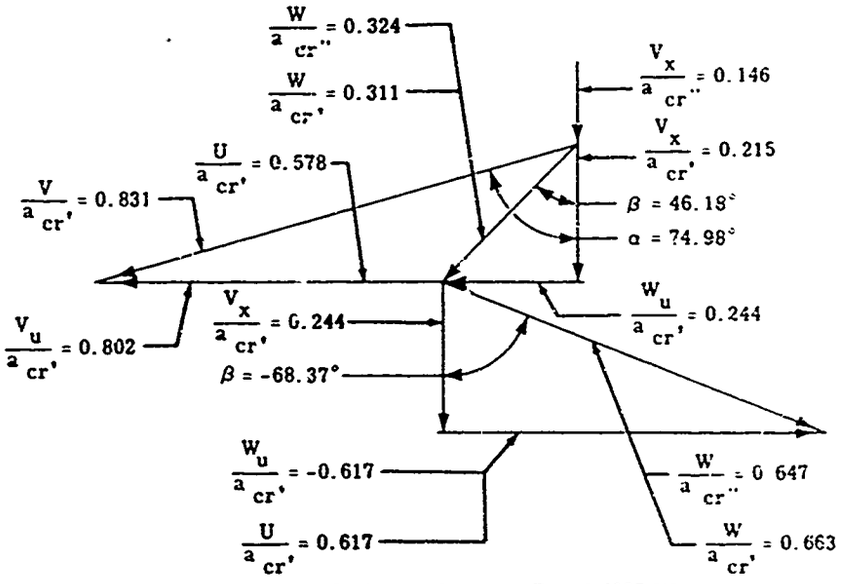

ROTOR VECTOR DIAGRAM, R = 4.1957 IN.

Figure 20. Representative Vector Diagrams for First-Stage Turbine.

could affect turbine efficiency. Table VII reflects the old and the new revised turbine stage dimensions of Turbine Design A-338-5. The meridional view of the first stage is shown in Figure 21, with the radii indicated for the local vector diagrams and detailed vane and blade shape studies.

3.2.2 Detailed Stator-Vane Shape

The final detailed stator-vane shape is shown in Figures 22 and 23 for radii of 3.5694 and 3.9694 inches. These radii correspond to approximately one-quarter and three-quarters of the vane height, respectively. The stacking line for these vane sections was chosen at the center of the throat and was used as the origin of coordinates. Coordinates for vane sections at other radii were obtained from a linear interpolation or extrapolation by a computer program.

Also shown on Figures 22 and 23 are the corresponding surface velocity distributions in terms of velocity ratio, V/a_{cr}', as a function of the percentage of the axial chord. As anticipated, the surface velocity distributions show high reaction (large acceleration of the fluid) and minimum diffusion of the surface velocity, and therefore, represent an acceptable aerodynamic stator-vane design.

3.2.3 Detailed Rotor Blade Shape

The final detailed rotor blade shape was based on analyses conducted at five cross sections. These five cross sections were taken at the following radii and corresponding blade positions:

1. 3.4204 inches - blade root
2. 3.5694 inches - one-quarter of blade height
3. 3.7694 inches - mean blade height
4. 3.9694 inches - three-quarters of blade height
5. 4.1057 inches - blade tip

The stacking line for these blade sections is the center of gravity of each section. Coordinates for blade sections at other radii were obtained from a linear interpolation or extrapolation by a computer program.

TABLE VII. TURBINE A-338-5 STAGE DIMENSIONS

Stages	Old Dimensions Hub Radius (in.)	Old Dimensions Tip Radius (in.)	New Dimensions Hub Radius (in.)	New Dimensions Tip Radius (in.)
First				
Stator				
Inlet	3.318	4.058	3.4204	4.1057
Exit	3.318	-	3.4204	4.1057
Rotor				
Inlet	3.318	4.058	3.4102	4.1452
Exit	3.318	-	3.4102	4.1452
Second				
Stator				
Inlet	3.318	4.058	3.4000	4.1452
Exit	3.318	4.428	3.4000	4.4405
Rotor				
Inlet	3.318	4.428	3.3898	4.4803
Exit	3.318	-	3.3898	4.4803
Third				
Stator				
Inlet	3.318	4.428	3.3796	4.4803
Exit	3.318	4.914	3.3796	4.9085
Rotor				
Inlet	3.314	4.914	3.3694	4.9496
Exit	3.314	-	3.3694	4.9496

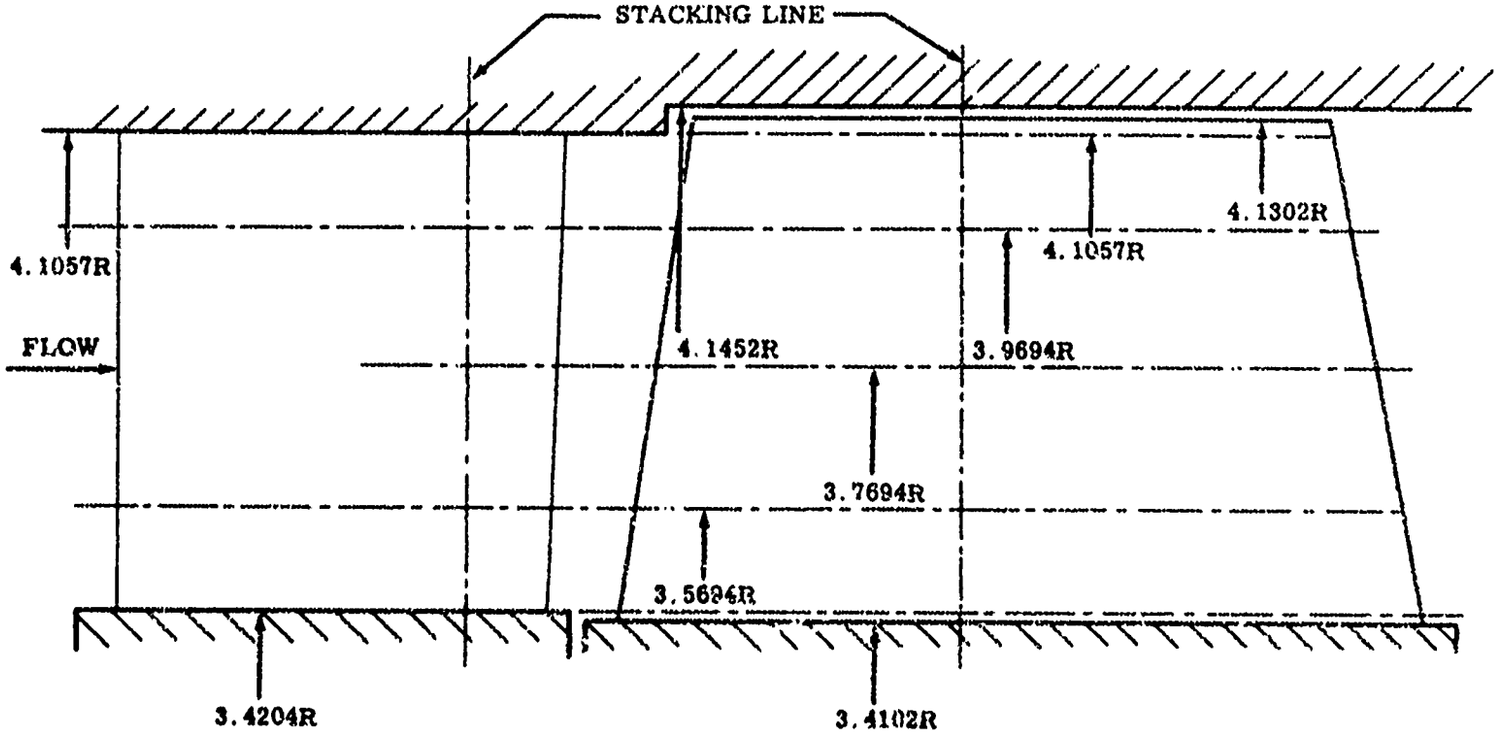

Figure 21. Meridional View of First-Stage Turbine.

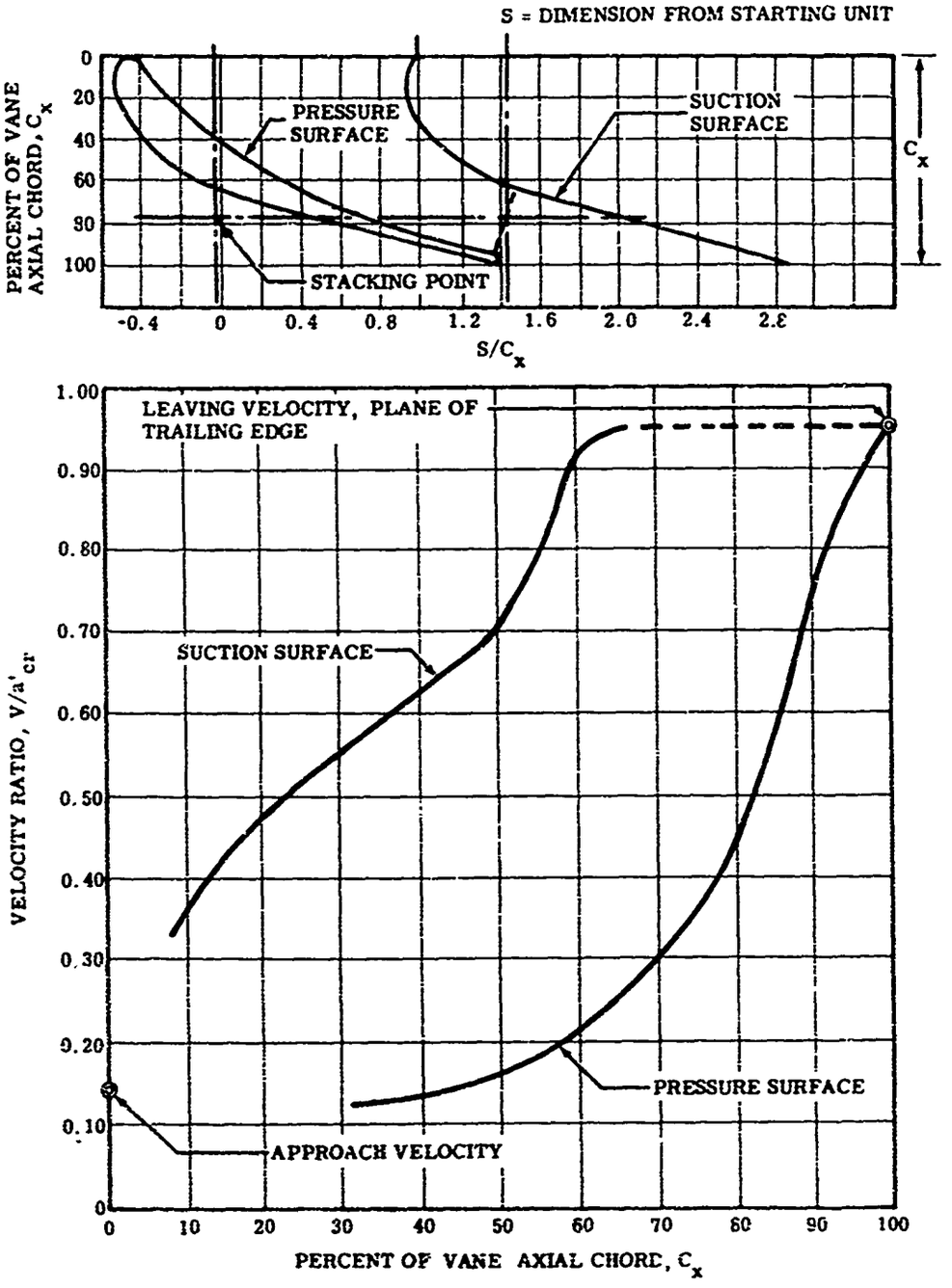

Figure 22. First-Stage Stator Vane Shape and Corresponding Surface Velocity Distribution for R = 3.5694 Inches.

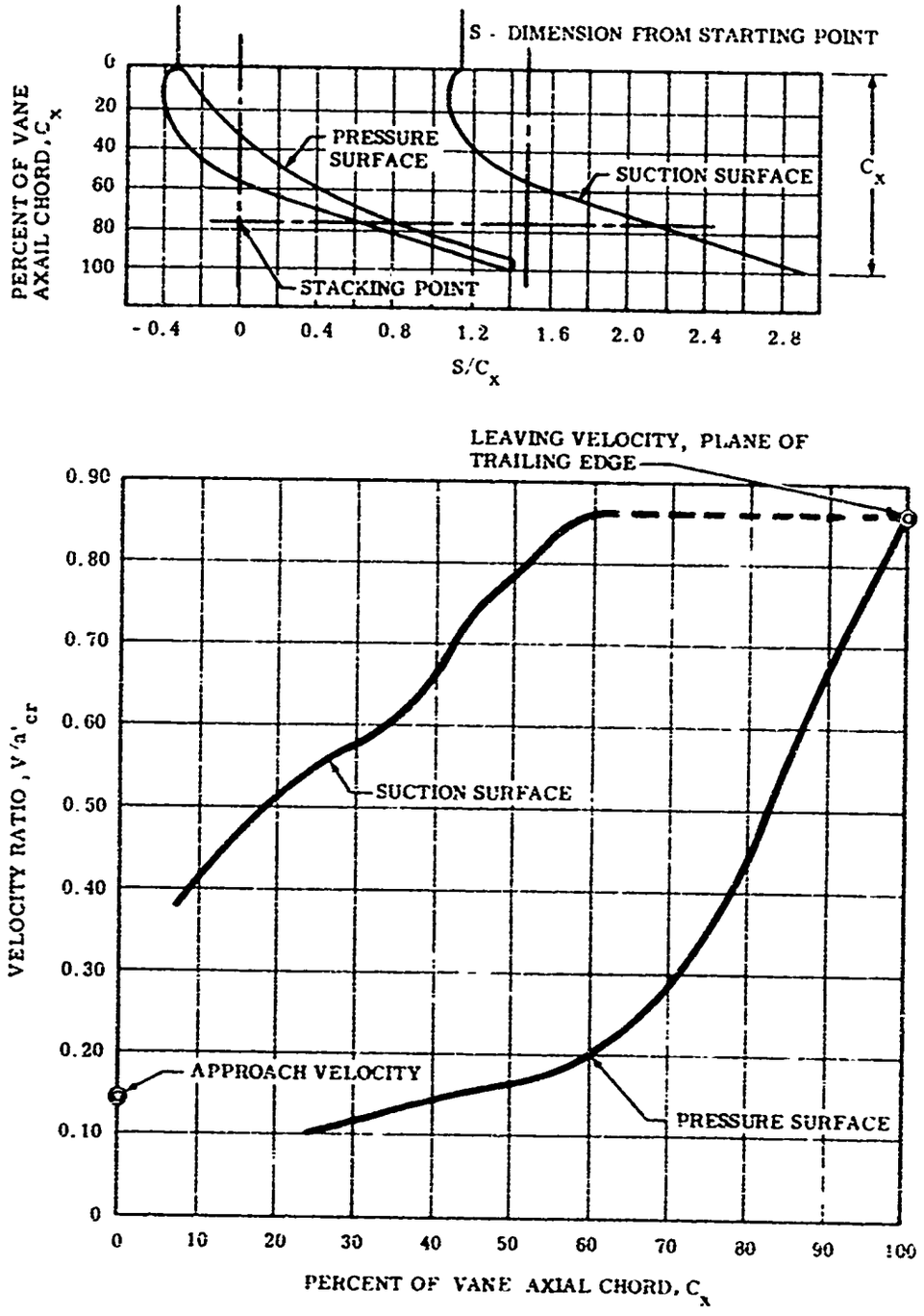

Figure 23. First-Stage Stator Vane Shape and Corresponding Surface Velocity Distribution for R = 3.9694 Inches.

The blade shape is shown in Figures 24 and 25 for radii of 3.5694 and 4.1057 inches. Also shown in these figures are the corresponding surface velocity distributions in terms of velocity ratio, W/a''_{cr}, as a function of the percentage of the axial chord. Evaluation of these data shows that only slight suction surface diffusion is present and the overall blade reaction increases rapidly with an increasing radius and, therefore, the rotor blade shape represents an acceptable aerodynamic rotor blade design.

3.3 MECHANICAL STUDIES

With the detailed aerodynamic shapes established for the first-stage turbine stator vane and rotor blade, mechanical studies were initiated to determine the most advantageous structural configuration of the first-stage turbine components without affecting the established airfoil shapes. Included in the mechanical studies were detailed thermal and thermal-stress analyses, stator-vane and rotor-blade attachment studies, and photoelastic and thermal-conduction test evaluations.

The mechanical design goal, as stated in the preliminary design studies, was a 200-hour stress-rupture life at 2400°F TIT. The final design mechanical studies included sufficient stress analyses to facilitate evaluation of two potential failure modes--stress rupture and low-cycle fatigue. For the stress-rupture evaluation, it was planned that the pertinent calculated stresses from the mechanical studies would be compared to the stress-rupture properties of the turbine material, which were to be determined in the concurrent turbine-materials research program reported in Volume I. For the low-cycle fatigue evaluation, it was planned that the pertinent calculated stresses from the mechanical studies would be compared to those determined by similar analyses in operational gas-turbine engines of comparable size and design. No attempt was planned at this time to obtain low-cycle fatigue properties for the beryllide material because of the complexities involved in this type of testing. However, this task was anticipated to be accomplished later in the program, depending upon the degree of success that was realized with the beryllide material.

At this time in the program, the material properties of IN-100 (rotor-disk material) had been established, material property testing of Composition 1 (stator-vane material) had been initiated, the stator-vane cascade test rig was being developed, and Composition 2 (rotor-blade

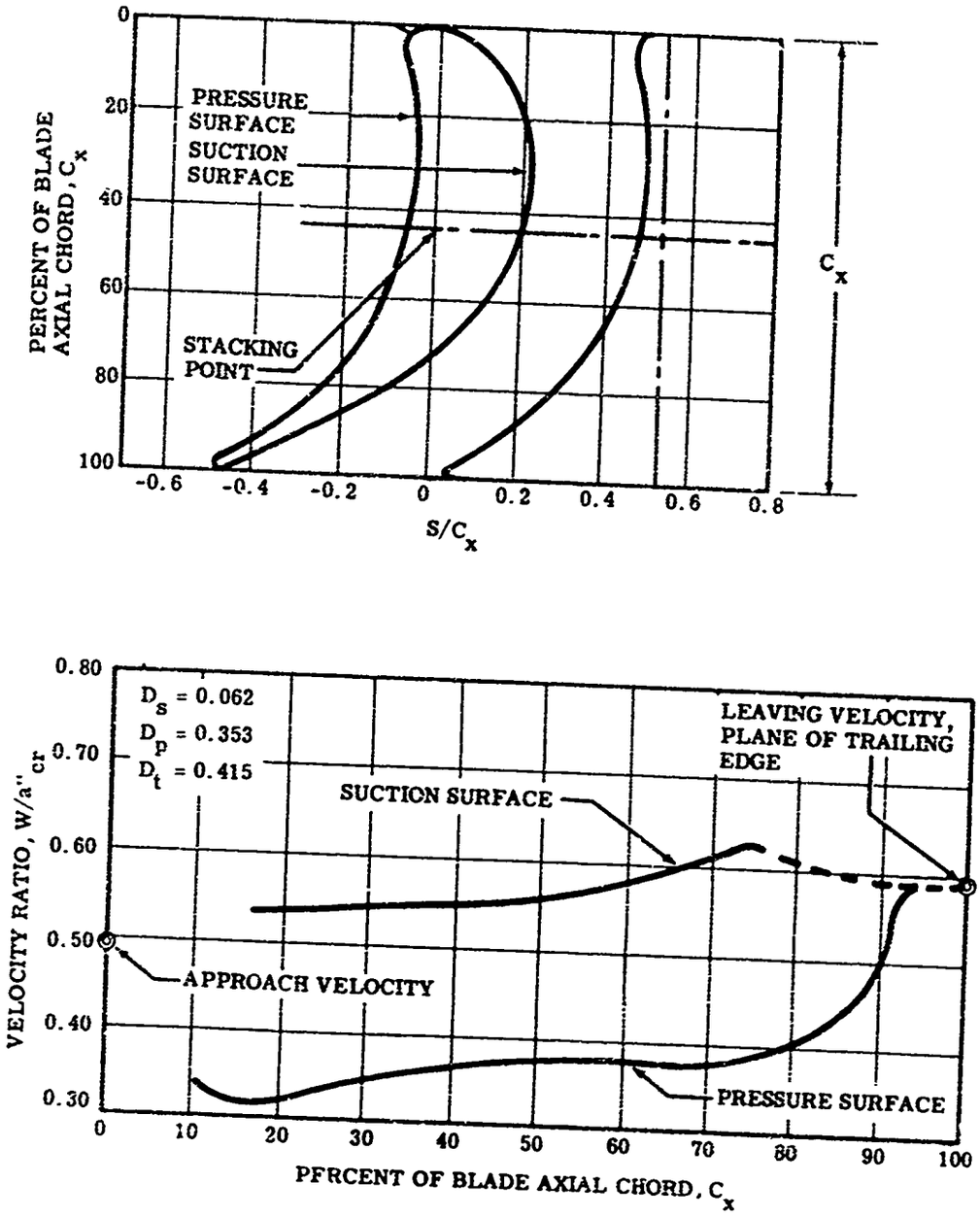

Figure 24. First-Stage Rotor Blade Shape and Corresponding Surface Velocity Distribution for R = 3.5694 Inches.

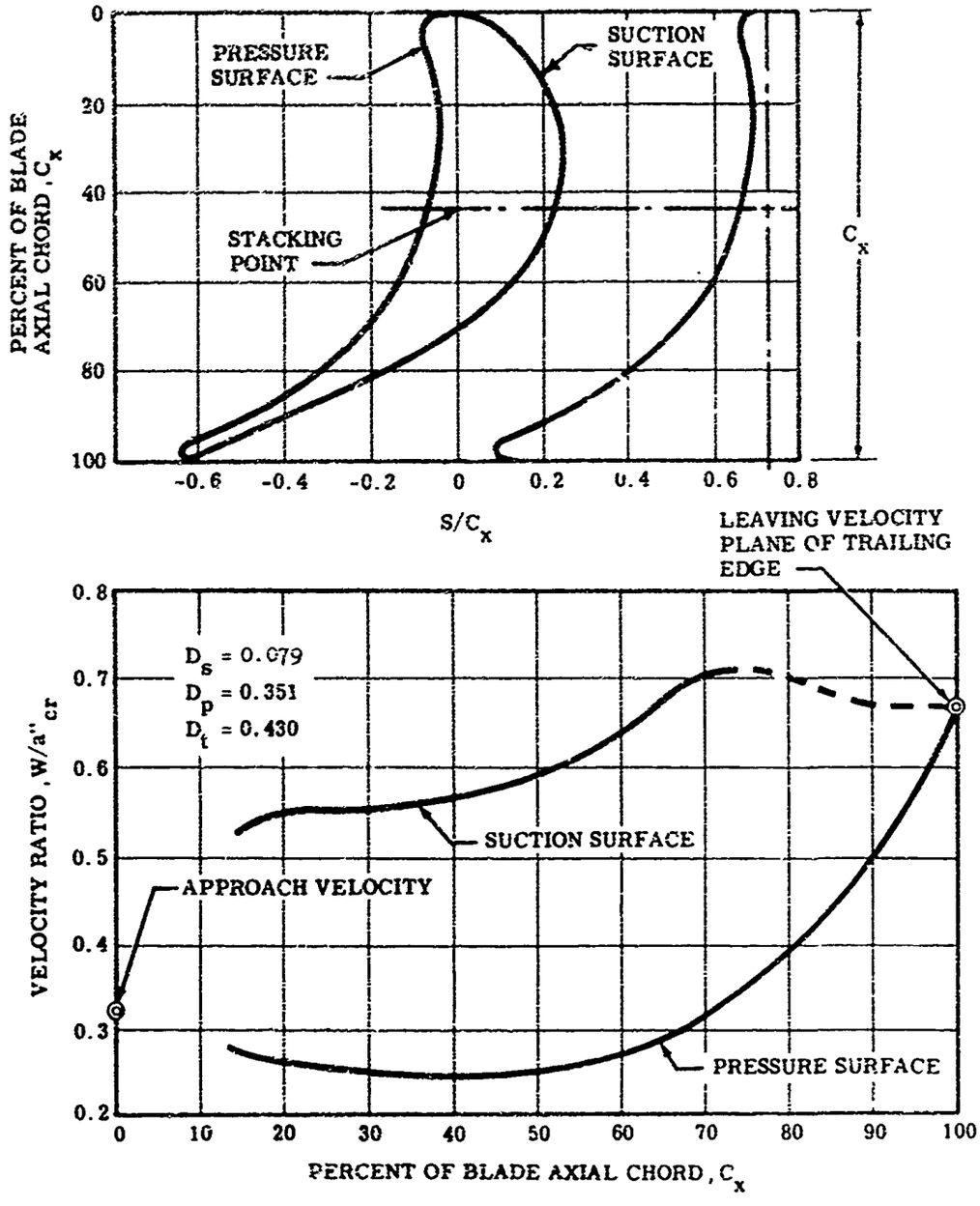

Figure 25. First-Stage Rotor Blade Shape and Corresponding Surface Velocity Distribution for R = 4.1057 Inches.

material) material-development studies had not yet been initiated (reported in Volume I). Therefore, it was necessary to estimate the physical properties of the beryllide material. The pertinent physical properties that were estimated for use in these mechanical studies are shown in Table VIII. For information purposes, Table VIII also includes measured values of the physical properties that were obtained at a later date from the materials research program.

TABLE VIII. COMPARISON OF BERYLLIDE PHYSICAL PROPERTIES ESTIMATED AND MEASURED AT 800°F

Physical Property	Estimated Values	Measured Values
Modulus of elasticity, psi	43.9×10^6	42.3×10^6
Coefficient of thermal expansion, in./in. - °F	8.83×10^{-6}	8.20×10^{-6}
Density, lb/cu in.	0.114	0.108
Specific heat, Btu/lb - °F	0.340	0.312
Thermal conductivity, Btu/hr-ft^2-°F/in.	222	165

3.3.1 Rotor--Mechanical Design Studies

The mechanical design studies that were conducted to determine and evaluate structural configurations of the rotor blade, rotor disk/blade attachment, and rotor disk of the first-stage turbine are reported in the following subparagraphs.

3.3.1.1 Rotor Blade

The first mechanical configuration of the aerodynamic blade design to be evaluated was that of a solid blade. Initial studies of the solid blade revealed that the centrifugal blade load imposed on the disk was approximately 2680 pounds per blade. This value was nearly twice the estimated blade loading used for the preliminary-design disk shape studies and was considered to be prohibitive to the anticipated rotor disk/blade attachment. To reduce the magnitude of the blade loading, studies were initiated to design a radial hole in the solid blade and, thus, reduce the blade mass. Analyses were conducted to determine the most desirable hole size and location to minimize the thermal and centrifugal loading stresses.

In determining the contour of the radial hole, a minimum blade wall thickness of 0.025 inch was selected. This dimension was located near the minimum value of heat-transfer coefficient on the pressure side of the blade, since the wall thicknesses around the radial hole were determined with the objective of minimizing the thermal gradients occurring over the cross section at any blade section. Because of the blade taper, from tip to root, the minimum wall thickness varied from 0.025 inch at the tip end to 0.032 inch at the root end of the hole. The radial hole reduced the mass of the airfoil portion of the blade by 41 percent. The solid blade centrifugal load of 2680 pounds per blade was reduced to 1640 pounds per blade after adding the radial hole. The shape of the contoured radial hole in the blade is shown in Figure 26. Also shown in this figure is the calculated static-pressure distribution around the blade at the cross section located at a radius of 3.7694 (mean blade height). From the calculated pressure distributions, the air loads were determined for the disk/blade attachment studies.

Detailed thermal and thermal-stress analyses were conducted on the rotor blade. For comparison purposes, the studies included both hollow and solid blades. The analyses involved determination of the steady-state heat-transfer-coefficient distribution and relative gas-temperature distribution around the blade (these data were available for the radial hole contour studies), the transient temperature distributions, and the corresponding thermal-stress distributions of the blade. Variations in gas temperature and heat-transfer coefficients with time were included in the analyses, as were the blade material-property variations with temperature. The time-dependent properties were the result of calculating the TIT variation with time based on existing experimental start data from three-stage turbines of lower operating TIT ranges (see Figure 27).

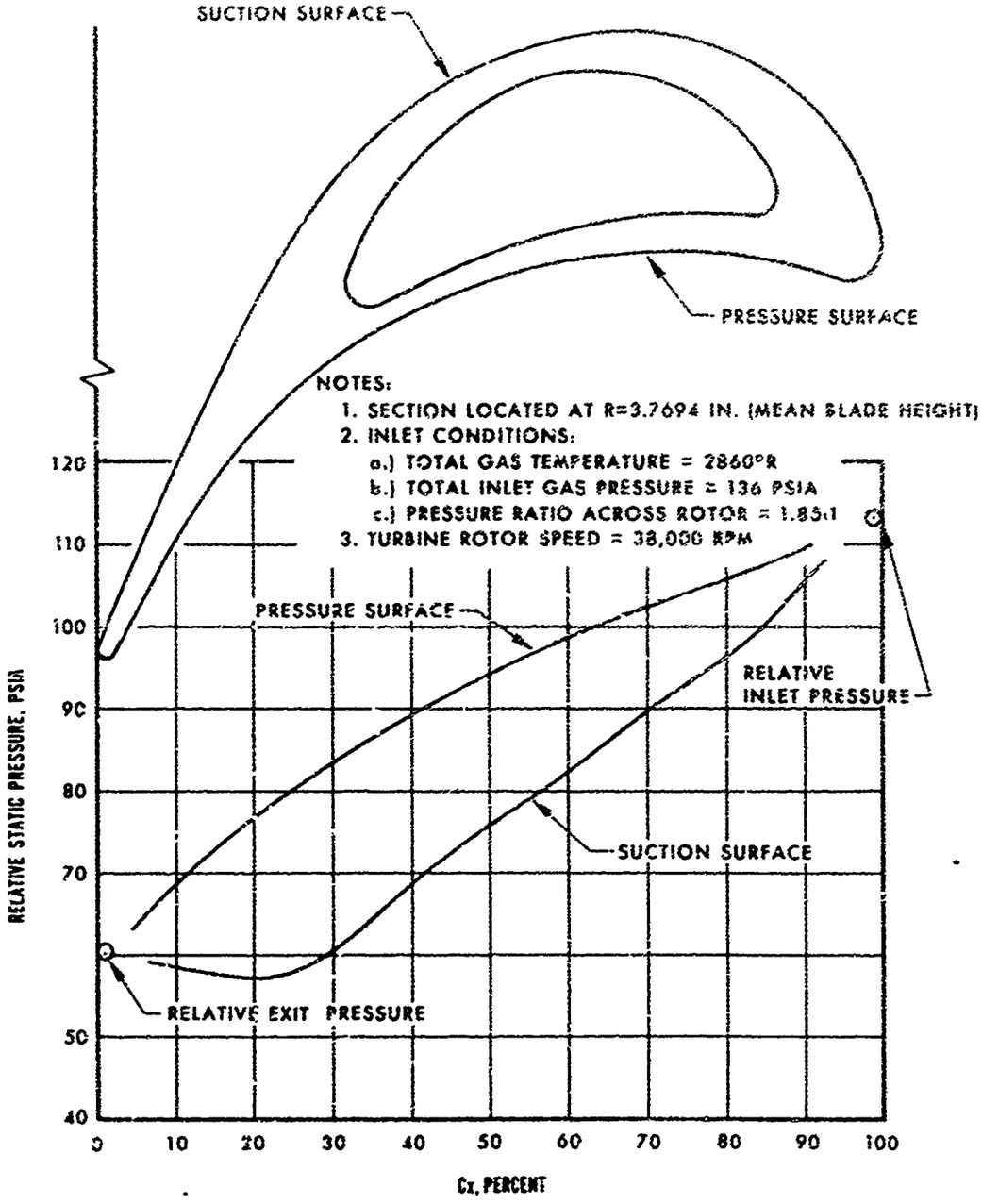

Figure 26. Rotor Blade Radial Hole Shape and the Calculated Static-Pressure Distribution.

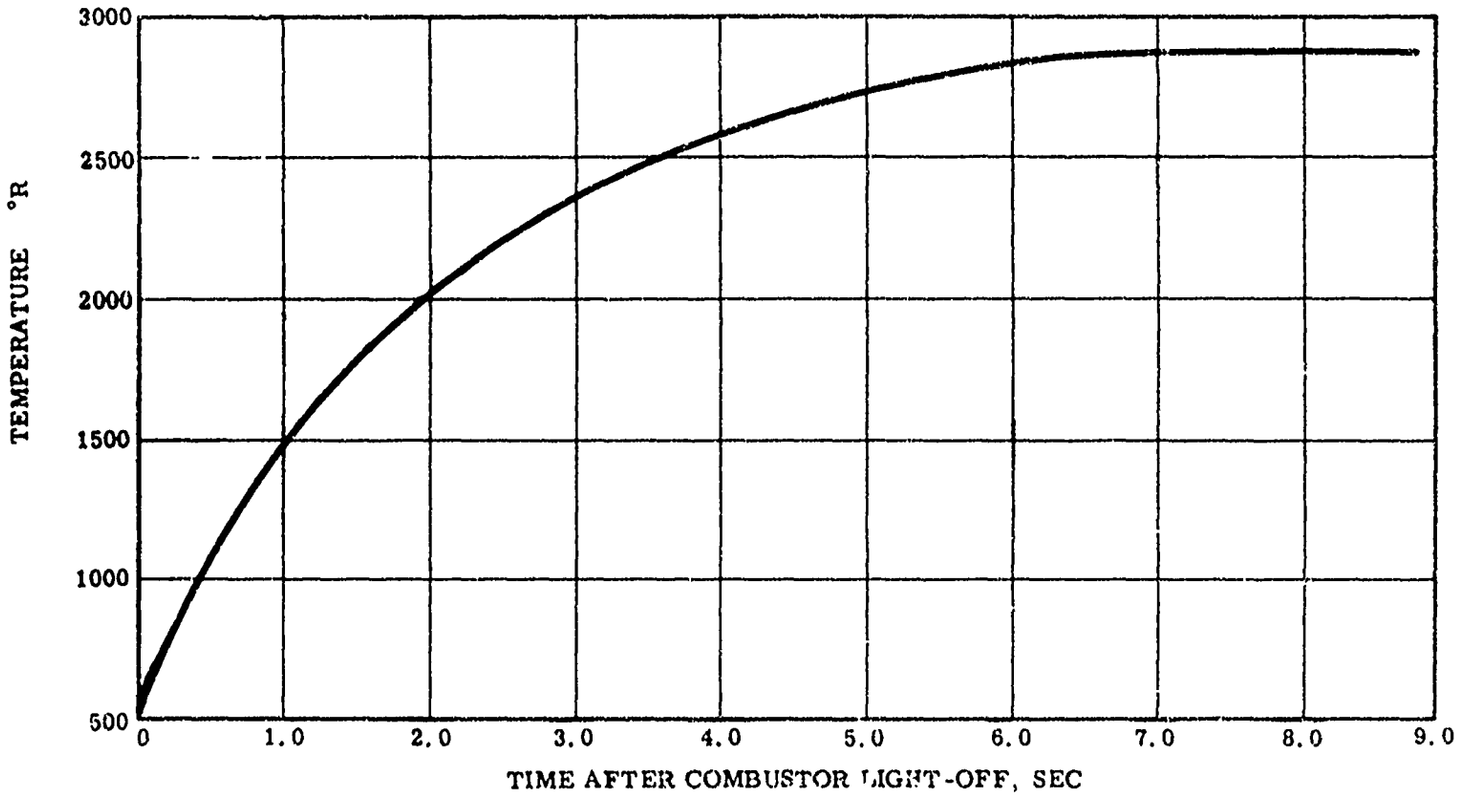

Figure 27. Calculated First-Stage TIT Variation With Time.

Other assumptions made for the thermal-stress calculations of the blade were:

1. There were no thermal gradients in the radial direction.

2. All stresses were due to thermal gradients in the remaining two directions (no external loads).

The following conditions of equilibrium were satisfied at the cross section analyzed:

$$\int \sigma \, dA = 0$$

$$\int \sigma x \, dA = 0$$

$$\int \sigma y \, dA = 0$$

where x and y are any axes in the plane of the cross section and A is the cross-sectional area of the blade section.

The heat-transfer-coefficient distribution and the relative gas-temperature distribution around the blade are shown in Figure 28 at steady state. A large variation in heat-transfer coefficient exists across the thick portion of the blade, which results in large thermal gradients in the blade during start-up. Also, the large variation in blade thickness from the middle of the blade cross section to the trailing edge increases the magnitudes of the thermal gradients that occur and the corresponding thermal stress levels.

Figures 29 and 30 show the results of the transient temperature and thermal-stress analyses of the rotor blade cross section at a radius of 4.1057 inches (blade tip). The blade tip cross section was selected for these analyses, since it was the farthest removed from the blade root and, therefore, the least likely to be affected by radial conduction of heat into the disk/blade attachment. Experience has shown that radial conduction of heat from the blade cross sections near the root into the disk/blade attachment region tends to produce thermal gradients that are less severe than those predicted by a two-dimensional heat-transfer analysis that neglects radial conduction. As shown in Figure 29, making the blade hollow caused an approximate 25-percent

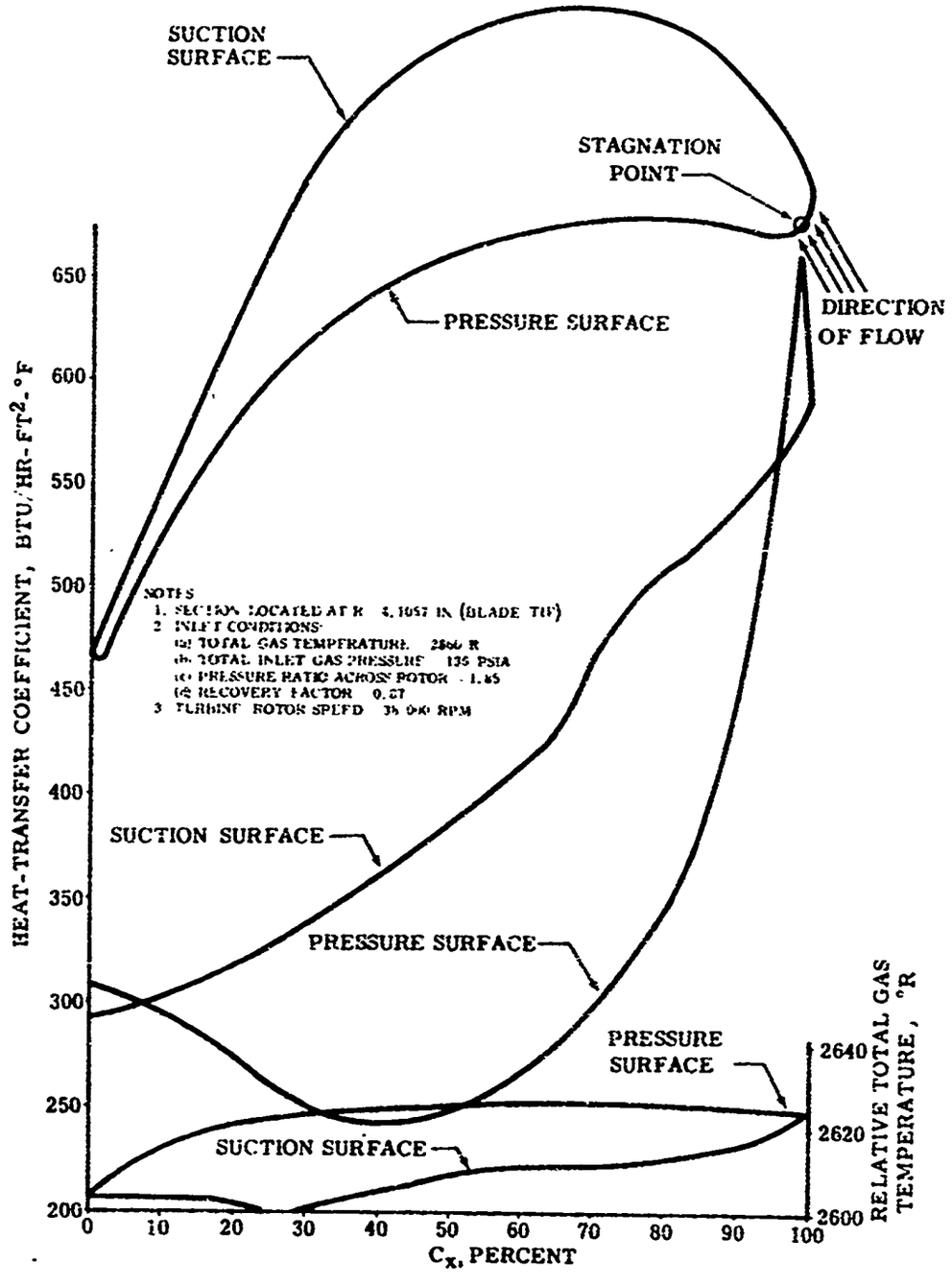

Figure 28. Steady-State Heat-Transfer-Coefficient Distribution and Relative Gas-Temperature Distribution Around the Blade.

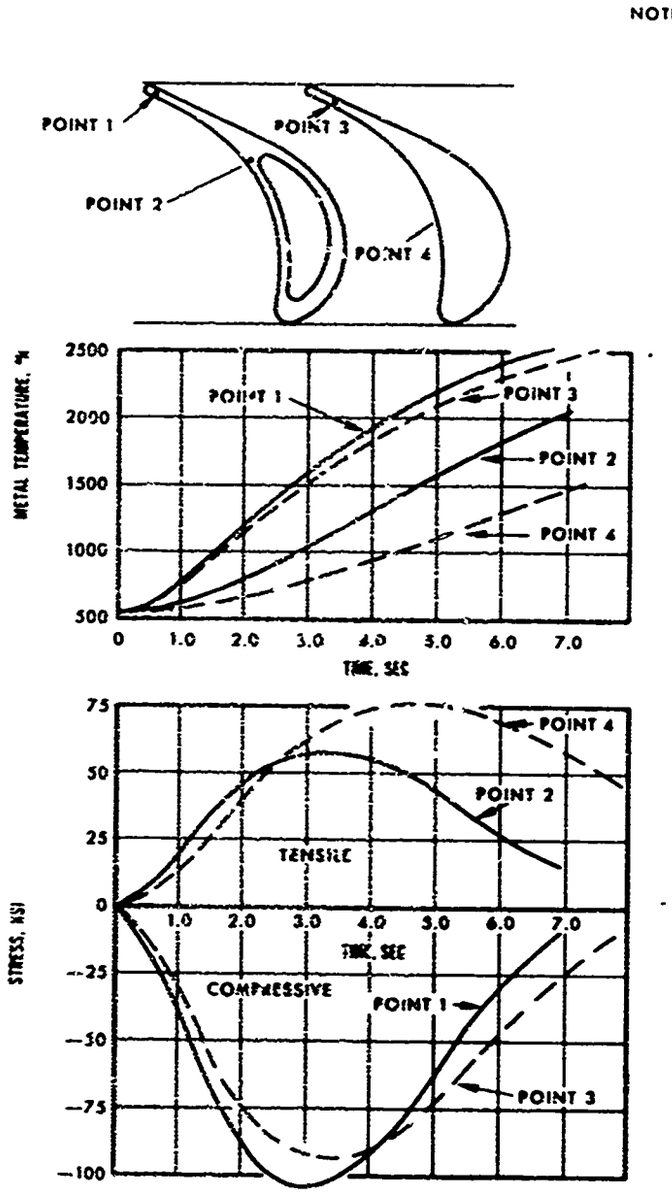

Figure 29. Transient Thermal Study of Rotor Blade Section at R = 4.1057 Inches (Blade Tip).

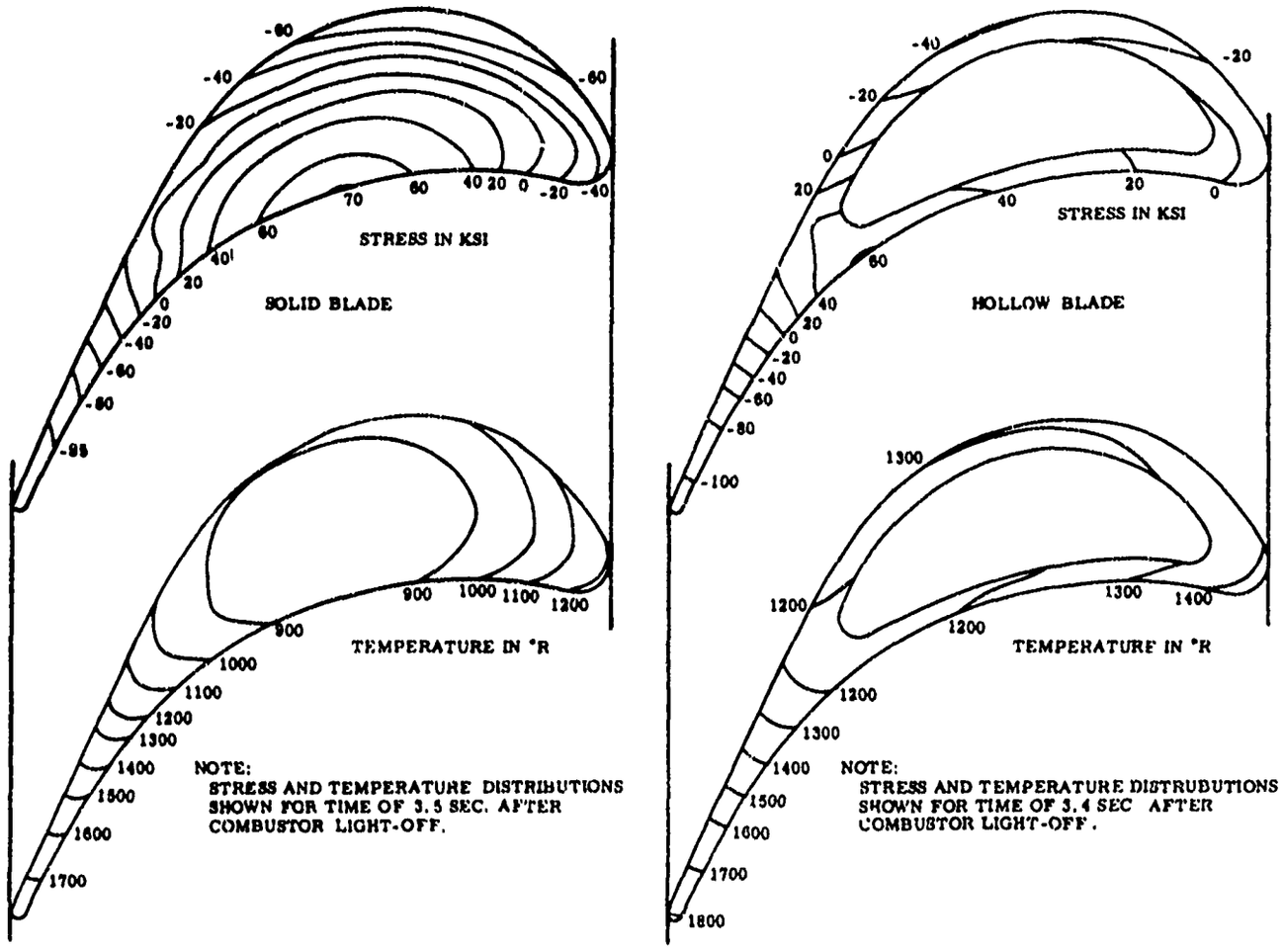

Figure 30. Transient Temperature and Stress Distribution of Rotor Blade Section at R = 4.1057 Inches (Blade Tip).

reduction in the peak positive thermal stress level and an approximate 16-percent increase in the peak compressive stress level. The solid blade material temperature at the time and place these peak stresses occur is approximately 1100°F and 700°F at stress levels of minus 90,000 psi and plus 75,000 psi, respectively. For the hollow blade, the temperatures are approximately the same, and the stress levels are minus 105,000 psi and plus 55,000 psi, respectively.

These transient thermal stresses are of a magnitude (80,000 to 120,000 psi) similar to that calculated in operational gas-turbine engines of comparable size and design. No further attempt was made at this time to reduce the transient thermal stresses or to perform a low-cycle-fatigue analysis on the subject rotor blade configurations. As previously stated, low-cycle-fatigue analyses were to be conducted in a later phase of the program provided that the beryllide material successfully satisfied the stress-rupture requirements of this phase of the final design.

The transient thermal stress analyses (Figures 29 and 30) were performed to investigate whether the estimated physical properties of the beryllide turbine material would result in excessive thermal stress levels as compared to those calculated in conventional turbine material. Since no stresses encountered were significantly greater than those occurring in conventional turbine designs, and beryllide material properties were not yet available from the materials test program, the hollow-blade configuration was judged to be an acceptable mechanical design.

3.3.1.2 Rotor Disk/Blade Attachment

The rotor disk/blade attachment design objective was to determine a configuration in which the calculated maximum stress in both the disk and the blade portions did not exceed 40,000 psi at operating speed. This stress level was again based on preliminary materials testing with the beryllide compositions.

It was evident that a dovetail attachment design (single lobe) required considerably less ductility in the disk/blade material combination to obtain an even distribution of the loading than that required for a fir-tree attachment design (double lobe). For this reason, the disk/blade attachment studies were conducted initially for a dovetail attachment design.

3.3.1.2.1 Dovetail Attachment Design and Analyses

Figure 31 shows the general configuration, stress point locations and pertinent dimension locations of the dovetail attachment design that was analyzed. In the design of dovetail blade attachments, the critical location for stress in the blade is normally where the necked section joins the tang or hook of the dovetail. This section is located between points B and D in Figure 31. Because of the nonuniformity of load distribution and neck stress distribution, the fillet stress at this section can normally be expected to be highest on one of the four external corners labeled 1, 2, 3, and 4 in Section A-A of Figure 31. The corner having the critical stress will depend on the magnitude and direction of the loads. Similar circumstances exist for the disk portion of the attachment.

The fillet stress, σ_f, is a measure of nearness to failure and is actually a combination of the neck stress, σ_a, and the tang stress, σ_t. Points B and D in Figure 31 are the locations of the blade neck stress and tang stress, respectively. The equation that relates σ_f to σ_a and σ_t can be stated as:

$$\sigma_f = \sigma_a + T\sigma_t \tag{23}$$

where

$$T = \frac{1}{1 + c\ (\sigma_a/\sigma_t)}$$

$$c = \left(\frac{\lambda}{N}\right)^2$$

and λ is the angular separation (in degrees) between the tang stress and neck stress locations in Figure 31. A value of 44 for N was used in the analyses.

For the disk stress analysis, the same analytical approach was used. The maximum stress was calculated to occur at one of the four external corners labeled on Section C-C located between Points E and F in Figure 31. The fillet stress at each corner was determined from the same relationship between tang and neck stresses as used in the blade. In Figure 31, Point E is the location of the disk tang stress, and Point F is the location of the disk neck stress.

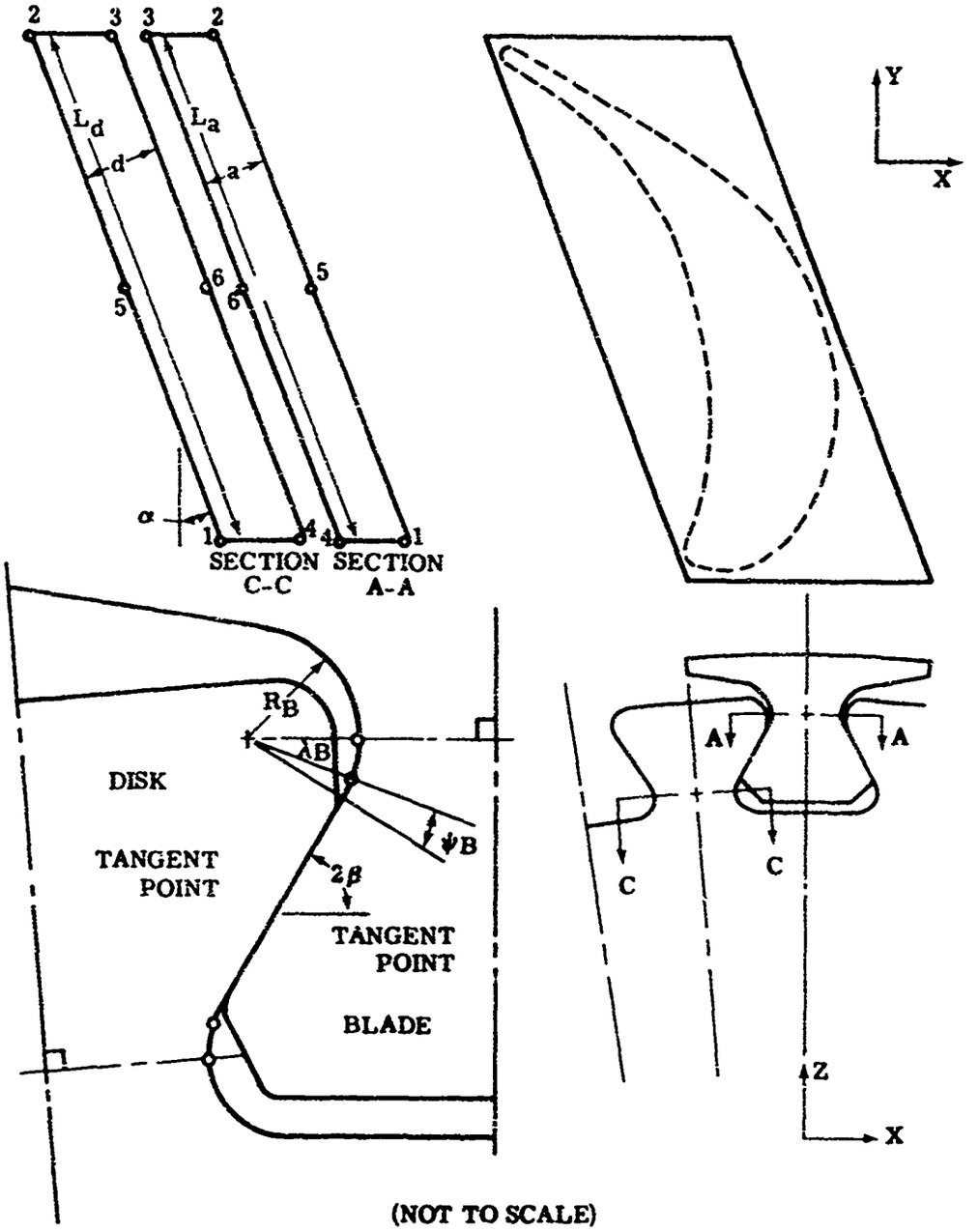

Figure 31. General Configuration, Stress Point Locations, and Pertinent Dimension Locations of Dovetail Attachment.

The location of Point E in the disk and Point D in the blade, where the tang stresses are calculated, depends on the value assumed for the angle, ψ. For single-tang dovetail shapes, which lack the stiffening of additional material under them and which have relatively steep flank angles (2β), the point of maximum stress may be very close to the tangency point. Thus, ψ may be taken as low as 5°. For these analyses, angle ψ was assumed equal to 10° for both the blade and disk.

In the stresses that were tabulated, a nominal and a maximum fillet stress occurred. The difference between these two is that the bending and tensile stresses that make up the fillet stress have been combined with the appropriate stress-concentration factors to give the maximum calculated fillet stress at the locations shown. This information was considered especially pertinent for the blade material, since the ductility and the susceptibility to brittle failure of the blade material were uncertain at this time.

The stress analyses conducted for the dovetail attachment consisted of studies of eight different configurations with use of an existing computer program. Included in the program were axial and tangential shear loads acting on the blade, as well as moments resulting from axial and tangential gas loads and bending loads in the blade. Table IX presents a summary of the pertinent dimensions (defined and listed below) or Configuration No. 1 and also shows the results of the stress analysis. The pertinent dimensions used for Configuration No. 1 were established as the standard values and were used as base-line references for the other configurations.

Analyses for each succeeding configuration were conducted with one of the pertinent dimensions varied while the remaining pertinent dimensions were maintained constant at the established base-line values. In this manner, the effect that each of the pertinent dimensions had on the calculated stress values of the attachment was evaluated. The pertinent dimensions whose values were varied in the stress studies were:

1. The flank angle, 2β
2. The blade neck thickness, a
3. The disk neck thickness, d
4. The fillet radii, R_B, R_D
5. The flank lengths, L_a, L_d

TABLE IX. PERTINENT DIMENSIONS AND CALCULATED STRESSES OF DOVETAIL DISK/BLADE ATTACHMENT, CONFIGURATION NO. 1

(Refer to Figure 31 for Locations)

PERTINENT DIMENSIONS: $2\beta = 60°$, $a = 0.15$, $d = 0.18$, $\alpha = 0°$, $R_B = 0.060$, $L_a = L_d = 1.0$, AND $R_D = 0.045$

LOCATION	POINT 1	POINT 2	POINT 3	POINT 4	POINT 5	POINT 6
BLADE PORTION OF ATTACHMENT STRESSES						
NOMINAL NECK STRESS	11024.36	12868.97	18152.36	24620.97	11946.67	21386.67
NOMINAL TANG STRESS	26492.07	25792.10	26011.39	32214.93	26142.09	29113.16
NOMINAL FILLET STRESS	35419.01	36250.68	40885.89	52442.65	35833.39	46663.38
MAXIMUM FILLET STRESS	53970.30	54273.33	60453.50	76790.20	54120.91	68621.18
NOM. HOOK SHEAR STRESS	10654.42	10379.91	10461.10	12956.01	10513.67	11708.56
DISK PORTION OF ATTACHMENT STRESSES						
NOMINAL NECK STRESS	34871.53	36001.33	24643.36	30975.19	35436.43	27809.28
NOMINAL TANG STRESS	22407.13	21815.09	22000.57	27247.56	22111.11	24624.06
NOMINAL FILLET STRESS	49985.79	50432.47	40972.85	51121.81	50207.73	46047.27
MAXIMUM FILLET STRESS	62224.27	63685.11	50221.00	64204.63	65026.25	55243.33
NOM. HOOK SHEAR STRESS	9588.98	9335.62	9414.99	11660.41	9462.30	10537.70
ADDITIONAL STRESSES, NOMINAL						
BEARING STRESS	16923.78	16476.62	16616.71	20579.68	16700.20	18598.20
COMBINED FILLET AND TORSIONAL SHEAR STRESS AT POINTS OF MAXIMUM STRESS IN BLADE					35839.71	46668.24
COMBINED FILLET AND TORSIONAL SHEAR STRESS AT POINTS OF MAXIMUM STRESS IN DISK					50209.98	46049.72

With completion of the stress analysis on the seventh configuration, a study was made to combine the optimum values of the pertinent dimensions determined by the seven studies into one design. Thus, this design represented the optimum configuration of the dovetail attachment. Table X presents the dimensions and stresses of the optimum configuration. The stress objective (40,000 psi) for the design was not realized. At this time, efforts were directed toward design and stress analyses of a fir-tree disk-blade attachment.

3.3.1.2.2 Fir-Tree Attachment Design and Analyses

Figure 32 shows the general configuration, stress-point locations, and pertinent dimension locations of the fir-tree attachment design that was analyzed. As discussed in the dovetail attachment analyses, the critical location for stress in the dovetail design is in the fillet area of the necked sections between the lobes. This is also true for the fir-tree design. The fillet stress, σ_f, of the fir-tree design was calculated in the same manner as that in the dovetail analyses.

Twenty-five fir-tree configurations were analyzed with use of a computer program. Included in the program were axial and tangential shear loads acting on the blade, as well as moments resulting from axial and tangential gas loads and bending loads in the blade. Data from the initial configuration (nominal pertinent dimensions and angles for base-line references) and from the optimized configuration analyses are shown in Tables XI and XII, respectively. The analyses were conducted in a manner similar to that of the dovetail analyses, where all pertinent dimensions and angles were maintained at the base-line values except one, which was varied. The effect of each variable was evaluated, and the pertinent dimension and angle values determined to be most advantageous were selected for the optimized configuration. The pertinent dimensions and angles that were varied during the analyses are listed in the referenced tables.

As can be seen in Table XII, in the recommended attachment design, the maximum blade-fillet stresses vary between 31,500 psi and 40,200 psi, while in the disk the nominal fillet stresses vary between 30,000 psi and 44,100 psi. A maximum disk temperature of 1500°F was estimated for the point where the stresses exceed 40,000 psi in the disk

TABLE X. PERTINENT DIMENSIONS AND CALCULATED STRESSES OF THE OPTIMIZED DOVETAIL DISK/BLADE ATTACHMENT DESIGN, CONFIGURATION NO. 8

(Refer to Figure 31 for Locations)

PERTINENT DIMENSIONS: $2\beta = 70°$, $a = 0.17$, $d = 0.19$, $\alpha = 0°$, $R_B = 0.080$, $L_a = L_d = 1.10$, AND $R_D = 0.065$

LOCATION	POINT 1	POINT 2	POINT 3	POINT 4	POINT 5	POINT 6
BLADE PORTION OF ATTACHMENT STRESSES						
NOMINAL NECK STRESS	9657.12	10399.50	14652.51	18766.80	10028.31	16709.66
NOMINAL TANG STRESS	15328.46	14496.88	15239.26	18081.99	14912.67	16660.63
NOMINAL FILLET STRESS	24502.48	24378.41	29170.74	35928.75	24440.38	32549.69
MAXIMUM FILLET STRESS	37711.05	36892.64	43077.24	52569.83	37301.80	47823.49
NOM. HOOK SHEAR STRESS	6935.54	6559.29	6895.19	8181.41	6747.42	7538.30
DISK PORTION OF ATTACHMENT STRESSES						
NOMINAL NECK STRESS	30694.03	30774.34	22390.62	26712.91	30734.19	24551.76
NOMINAL TANG STRESS	14409.74	13628.00	14325.89	16998.24	14018.87	15662.06
NOMINAL FILLET STRESS	42396.63	41718.44	34637.72	41233.05	42057.18	37935.38
MAXIMUM FILLET STRESS	42922.28	43072.58	33676.80	41667.26	43955.42	36723.01
NOM. HOOK SHEAR STRESS	6837.86	6466.90	6798.07	8066.18	6652.38	7432.13
ADDITIONAL STRESSES, NOMINAL						
BEARING STRESS	13918.32	13163.25	13837.33	16418.55	13540.78	15127.94
COMBINED FILLET AND TORSIONAL SHEAR STRESS AT POINTS OF MAXIMUM STRESS IN BLADE					24445.05	32553.20
COMBINED FILLET AND TORSIONAL SHEAR STRESS AT POINTS OF MAXIMUM STRESS IN DISK					42058.95	37937.35

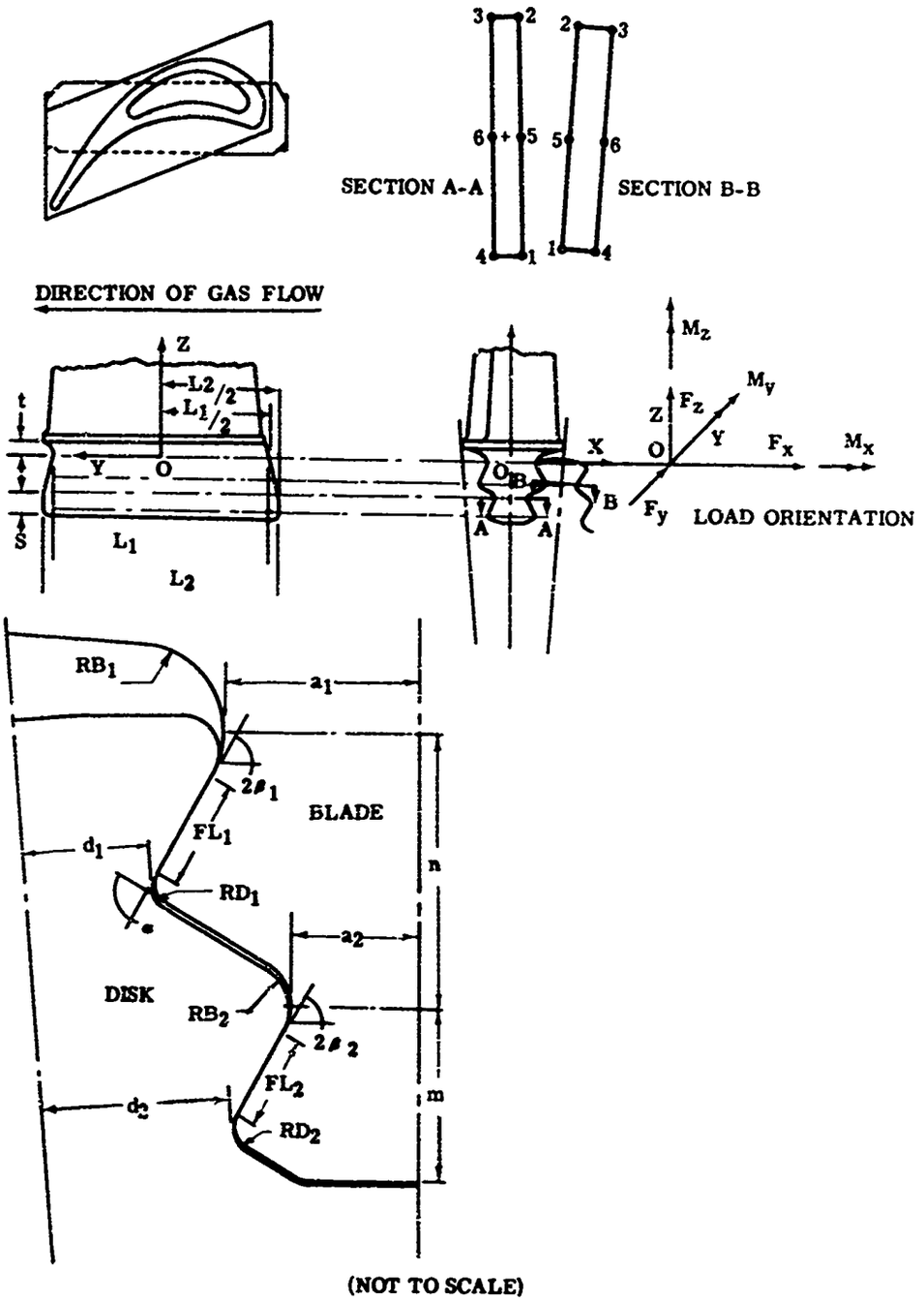

Figure 32. General Configuration, Stress Point Locations, and Pertinent Dimension Locations of Fir-Tree Attachment.

TABLE XI. PERTINENT DIMENSIONS AND CALCULATED STRESSES OF FIR-TREE DISK BLADE ATTACHMENT, CONFIGURATION NO. 1

(Refer to Figure 32 for Locations)

PERTINENT DIMENSIONS (IN.)

a_1	.71	RB_1 = .058	FL_1 = .060	a_2 = .100	RB_2 = .019	FL_2 = .054
d_1	.147	RD_1 = .019	L_1 = 1.0	d_2 = .253	RD_2 = .019	L_2 = 1.0
		t = .070	x = .105	S = -	n = .183	

PERTINENT ANGLES (DEGREES)

$2\theta_1$ = 45.5 α = 70 $2\theta_2$ = 45.5

LOAD (POUNDS)			MOMENTS (INCH-POUNDS)		
F_z = 2500	F_x = 37.1	F_y = 60.3	M_z = -21.4	M_x = -28.9	M_y = 17.7

UPPER LOBE PAIR

LOCATIONS	POINT 1	POINT 2	POINT 3	POINT 4	POINT 5	POINT 6
BLADE PORTION OF ATTACHMENT STRESSES (PSI)						
NOMINAL NECK STRESS	7200	11600	10400	18100	9400	14300
NOMINAL TANG STRESS	17600	18400	18000	24500	18000	21300
NOMINAL FILLET STRESS	24200	28900	27400	40900	26600	34200
MAXIMUM FILLET STRESS	38500	44500	42400	61700	41500	52100
NOM. HOOK SHEAR STRESS	8700	9100	7900	10800	8900	9300
DISK PORTION OF ATTACHMENT STRESSES (PSI)						
NOMINAL NECK STRESS	23400	30400	6000	15400	26900	10700
NOMINAL TANG STRESS	27500	28700	21100	28800	28100	25000
NOMINAL FILLET STRESS	39300	46100	23300	35700	43000	29400
MAXIMUM FILLET STRESS	64900	76300	35800	56600	70500	46000
NOM. HOOK SHEAR STRESS	7800	8200	7100	9700	8000	8400
ADDITIONAL STRESSES, NOMINAL (PSI)						
BEARING STRESS	13200	13800	12000	16400	13500	14200
COMBINED FILLET AND TORSIONAL SHEAR STRESS AT POINTS OF MAXIMUM STRESS IN BLADE					26600	34200
COMBINED FILLET AND TORSIONAL SHEAR STRESS AT POINTS OF MAXIMUM STRESS IN DISK					43000	294000

LOWER LOBE PAIR

BLADE PORTION OF ATTACHMENT STRESSES (PSI)						
NOMINAL NECK STRESS	-300	11600	13800	30100	5600	21900
NOMINAL TANG STRESS	20600	21700	20300	27700	21200	24000
NOMINAL FILLET STRESS	20700	28000	28200	46800	23900	37400
MAXIMUM FILLET STRESS	35990	48500	49200	79700	41800	64600
NOM. HOOK SHEAR STRESS	9000	9400	8200	11200	9200	9750
DISK PORTION OF ATTACHMENT STRESSES (PSI)						
NOMINAL NECK STRESS	29700	32400	14500	20700	31000	17600
NOMINAL TANG STRESS	22000	23000	24100	32900	27500	28500
NOMINAL FILLET STRESS	47300	50700	36300	50200	49000	43300
MAXIMUM FILLET STRESS	84500	92200	58500	83800	88400	71200
NOM. HOOK SHEAR STRESS	7800	8200	7100	9700	8000	8400
ADDITIONAL STRESSES, NOMINAL (PSI)						
BEARING STRESS	12400	12900	11300	15400	12600	13300
COMBINED FILLET AND TORSIONAL SHEAR STRESS AT POINTS OF MAXIMUM STRESS IN BLADE					23900	37400
COMBINED FILLET AND TORSIONAL SHEAR STRESS AT POINTS OF MAXIMUM STRESS IN DISK					49000	43300

TABLE XII. PERTINENT DIMENSIONS AND CALCULATED STRESSES OF THE OPTIMIZED FIR-TREE ATTACHMENT DESIGN

(Refer to Figure 32 for Locations)

PERTINENT DIMENSIONS (IN.)

a_1 = .27	RB_1 = .045	FL_1 = .095	a_2 .172	RB_2 .032	FL_2 = .095
d_1 = .157	RD_1 = .0315	L_1 = 1.10	a_3 = .23	RD_2 = .0315	L_2 = 1.195
t = .05		w = .12	S = .095	n = .175	

PERTINENT ANGLES (DEGREES)

$2\alpha_1$ 60 α = 90 $2\alpha_2$ = 60

LOADS (POUNDS)			MOMENTS (INCH-POUNDS)		
F_z 2450	F_x = 37.1	F_y = 60.5	M_z = -21.3	M_x = 0.0	M_y 0.0

LOCATION	POINT 1	POINT 2	POINT 3	POINT 4	POINT 5	POINT 6
BLADE PORTION OF ATTACHMENT STRESSES (PSI)						
NOMINAL NECK STRESS	7300	9000	7300	9000	9200	8100
NOMINAL TANG STRESS	15100	13900	13900	15300	13500	14500
NOMINAL FILLET STRESS	20500	23000	21300	24400	21700	22900
MAXIMUM FILLET STRESS	34400	38200	35400	40200	36200	37800
NOM. HOOK SHEAR STRESS	7900	8400	7900	8400	8100	8400
DISK PORTION OF ATTACHMENT STRESSES (PSI)						
NOMINAL NECK STRESS	18300	21200	18700	15700	19800	14200
NOMINAL TANG STRESS	21500	22500	20600	22800	21900	21700
NOMINAL FILLET STRESS	35200	38700	30000	34500	27000	32300
MAXIMUM FILLET STRESS	43500	48700	35800	42300	40100	39900
NOM. HOOK SHEAR STRESS	9100	9600	9100	10100	9400	9600
ADDITIONAL STRESSES, NOMINAL (PSI)						
BEARING STRESS	17300	18300	17400	19200	17800	18300
COMBINED FILLET AND TORSIONAL SHEAR STRESS AT POINTS OF MAXIMUM STRESS IN BLADE					21700	22900
COMBINED FILLET AND TORSIONAL SHEAR STRESS AT POINTS OF MAXIMUM STRESS IN DISK					37000	32300
LOWER LOBE PAIR						
BLADE PORTION OF ATTACHMENT STRESSES (PSI)						
NOMINAL NECK STRESS	5700	6300	5700	5700	7000	6200
NOMINAL TANG STRESS	15800	16700	13900	15200	16200	14700
NOMINAL FILLET STRESS	20400	23400	19300	23100	21900	21700
MAXIMUM FILLET STRESS	33100	37400	31500	37400	35300	34500
NOM. HOOK SHEAR STRESS	7800	8300	7900	8700	8100	8300
DISK PORTION OF ATTACHMENT STRESSES (PSI)						
NOMINAL NECK STRESS	27900	29700	26700	23100	28900	22000
NOMINAL TANG STRESS	13800	14600	14600	16200	14200	15400
NOMINAL FILLET STRESS	41500	44100	35300	39100	42800	37200
MAXIMUM FILLET STRESS	49600	54300	39100	45100	52100	42100
NOM. HOOK SHEAR STRESS	7300	7600	7400	8100	7600	7700
ADDITIONAL STRESSES, NOMINAL (PSI)						
BEARING STRESS	17300	18300	17400	19200	17800	18300
COMBINED FILLET AND TORSIONAL SHEAR STRESS AT POINTS OF MAXIMUM STRESS IN BLADE					21900	21200
COMBINED FILLET AND TORSIONAL SHEAR STRESS AT POINTS OF MAXIMUM STRESS IN DISK					42800	37200

(based on the results of preliminary temperature studies that were being conducted on the disk to determine the optimum impingement cooling scheme). The minimum 200-hour stress-to-rupture value for IN-100 of 1500°F is 60,000 psi. Thus, a disk stress of 44,100 psi at this point was acceptable.

During the time period of the disk/blade attachment studies, a program was being prepared to experimentally evaluate the calculated stress distribution occurring in the disk/blade attachment by using the techniques of photoelasticity. This program, reported in Appendix III of this report, consisted of three major parts:

1. Design and fabrication of a photoelastic test rig.

2. Design and fabrication of the experimental attachment model to be tested.

3. Preparation of test procedures, conduction of the test, and analysis of the data.

Results from the photoelastic testing indicated that the fir-tree attachment stresses were somewhat lower than the calculated stresses shown in Table XII. There were a number of differences between the fir tree modeled in the photoelastic tests and the one analyzed in Table XII. These differences include:

1. An inability to model disk curvature in the photoelastic test rig.

2. In the photoelastic tests, no distinction was made between the blade centrifugal loading by itself and the combined centrifugal loading of the blade and the attachment.

3. The gas loads on the blade were not simulated in the test rig.

4. The difference between the disk and blade material moduli (24×10^3 psi for the disk and 39×10^6 psi for the blade) was not simulated in the photoelastic test rig.

All of the above would have contributed to the differences observed between the photoelastic results and the calculated stresses. The ability to study the relative effects of tolerances and load sharing in the photoelastic test rig made the photoelastic testing a valuable tool in establishing the final fir-tree configuration.

3.3.1.3 Rotor Disk

During the preliminary design mechanical studies, calculations were made to determine the temperature distributions (Paragraph 2.8) and the centrifugal and thermal elastic stresses (Paragraph 2.9) of the rotor disks. It was apparent from these preliminary analyses that the magnitude of the thermal stresses presented a problem that required solution. Studies were initiated to determine a cooling scheme which, without increasing the cooling-air flow rate, would provide greater disk cooling and produce a more favorable temperature gradient in the disk to reduce the thermal stresses to an acceptable level. From these studies, an optimized cooling scheme was determined in which equal portions of the cooling air were impinged upon each side of the disk wall, near the bore of the disk, to flow out radially along the disk sides and enter the hot-gas stream at the OD of the disk. The preliminary estimates for the airflow rates were determined to be adequate--namely, 50 percent for the first stage, 30 percent for the second stage, and 20 percent for the third stage, with the total representing 2.0 percent of the engine through-flow.

With completion of the rotor blade and the rotor disk/blade attachment final designs and with the cooling scheme optimized, analyses were conducted to calculate the temperature distributions, centrifugal stresses, and the combined centrifugal and thermal elastic stress of the first-stage rotor disk.

The heat-transfer-coefficient and the relative gas-temperature distributions around the blade (Figure 28) were included in the final thermal analyses. The cooling-air-heat-transfer coefficients were calculated with use of the estimated cooling-gas temperatures. A coolant inlet temperature of 900°F was used (this value was based on a 5.0-pound-per-second compressor with a pressure ratio of 10:1, and an estimated 100°F temperature rise in the coolant temperature from the time it leaves the compressor discharge until it is impinged upon the sides of the rotor disk). An existing computer program was used to calculate the metal temperatures, along with the cooling-air temperatures, as the coolant flowed radially out along the sides of the disk.

Thermal studies were completed for the rotor with and without the nickel shim stock placed between the mating surfaces of the blade and disk in the fir-tree attachment. As in the preliminary studies (Paragraph 2.8), use of the shim stock was determined to be advantageous; the metal

temperatures of the disk in the attachment area were reduced approximately 35°. This temperature reduction in the disk metal at the attachment area will allow an increase of approximately 5000 psi in stress level for the same disk life with the IN-100 disk material. In addition, use of the shim stock caused a slight reduction (1000 to 3000 psi) in the peak thermal stress levels in the disk. Therefore, the shim stock was recommended for inclusion in the final design.

In the temperature analyses, the contact resistance across the fir-tree attachment was simulated as an additional length to the conduction path connecting the blade to the disk. This additional conduction length was estimated (from scant data available at the time) as 0.09 inch. In terms of thermal resistance across the fir-tree attachment contact surfaces, this value indicated that the resistance was quite small and would have very little effect on the thermal gradients between the blade and the disk. There was concern that this resistance might be of much larger magnitude; therefore, a test program was prepared to determine the thermal conduction across the interface of the fir-tree attachment between the blade and the disk.

The thermal conduction test program, reported in Appendix IV of this document, consisted of two major parts:

1. Design and fabrication of the thermal conduction test rig and test specimens

2. Implementation of the test and analysis of the data

Results from the thermal-conduction testing indicated that the contact resistance, instead of being larger, was approximately 50 percent smaller than that used in rotor thermal analyses. Since the contact resistance was so small, reducing it further would have little or no effect on the calculated disk temperatures and cooling requirements, so no additional disk thermal analyses were conducted.

The calculated temperature distributions of the rotor with and without use of the shim stock are shown in Figure 33. The calculated disk and blade centrifugal stresses and the combined centrifugal and thermal elastic stresses of the rotor, without use of the shim stock, are shown on Figures 34 and 35, respectively. These stress data were selected to illustrate that the disk stresses are within an acceptable range even without the benefits gained by use of the shim

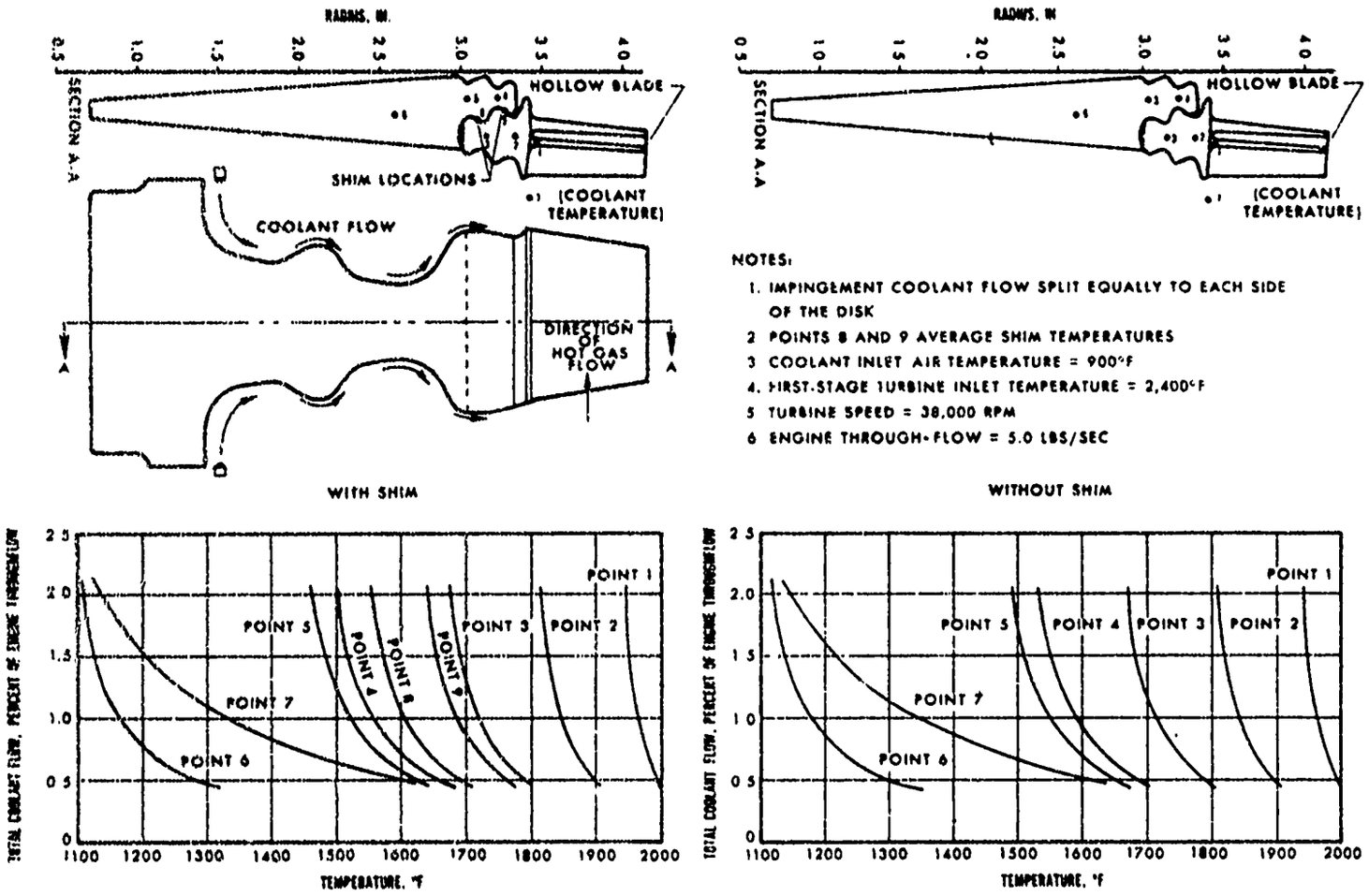

Figure 33. Temperature Distributions of Rotor With and Without Shim Stock in Place.

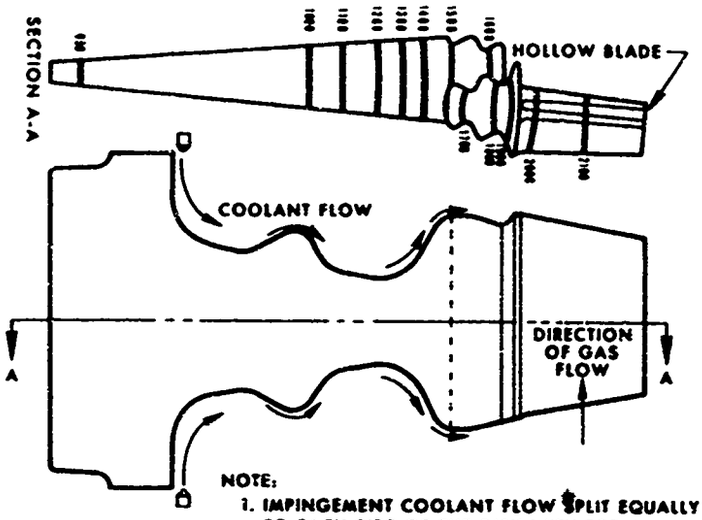

NOTE:

1. IMPINGEMENT COOLANT FLOW SPLIT EQUALLY TO EACH SIDE OF THE DISK WITH TOTAL COOLANT FLOW EQUAL TO 1-PERCENT OF ENGINE THROUGH-FLOW
2. TURBINE SPEED = 38,000 RPM
3. FIRST-STAGE TURBINE INLET TEMPERATURE = 2400°F
4. COOLANT INLET TEMPERATURE = 900°F
5. POINTS MARKED ⊡ REFER TO DESIGN FILLET STRESSES IN DISK PORTION OF BLADE-DISK ATTACHMENT
6. POINTS MARKED ⊙ REFER TO DESIGN FILLET STRESSES IN BLADE PORTION OF BLADE-DISK ATTACHMENT
7. COOLANT FLOW IMPINGES AT RADIUS = 1.400 INCH
8. ENGINE TOTAL THROUGH-FLOW = 5.0 LBS/SEC.
9. DISK AVERAGE TANGENTIAL = 54,500 PSI

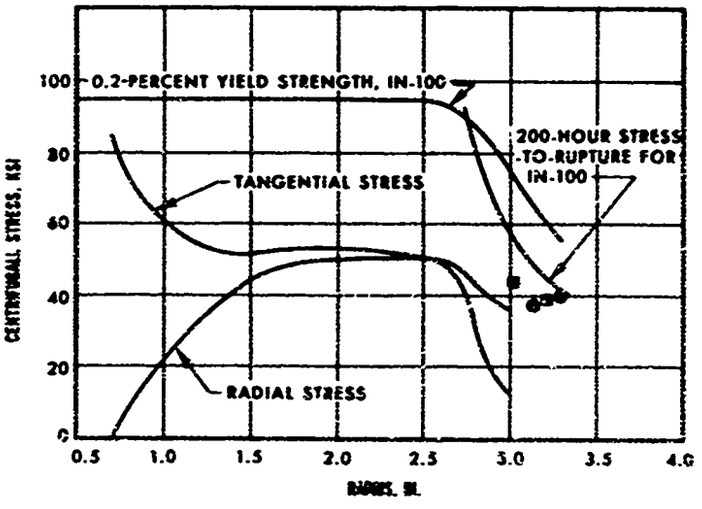

Figure 34. Calculated Centrifugal Stresses of Rotor Disk Without Shim in Place.

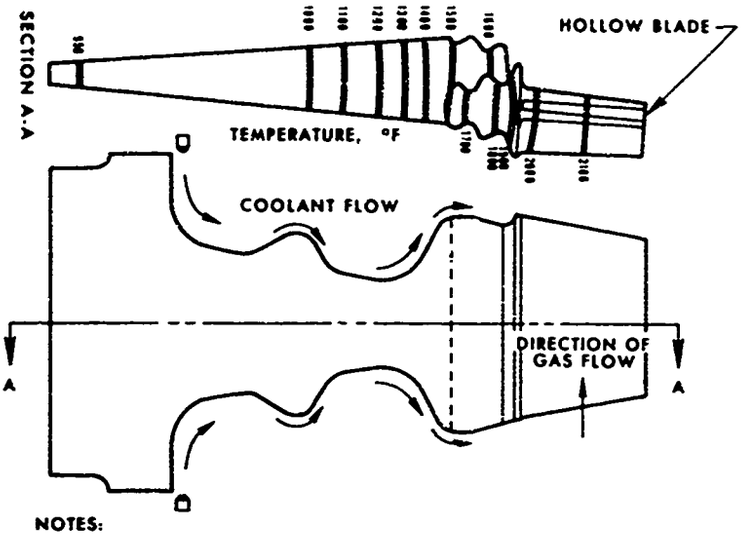

NOTES:

1. IMPINGEMENT COOLANT FLOW SPLIT EQUALLY TO EACH SIDE OF THE DISK WITH TOTAL COOLANT FLOW EQUAL TO 1-PERCENT OF ENGINE THROUGH-FLOW
2. TURBINE SPEED = 38,000 RPM
3. FIRST-STAGE TURBINE INLET TEMPERATURE = 2400°F
4. COOLANT INLET TEMPERATURE = 900°F
5. POINTS MARKED ⊡ REFER TO DESIGN FILLET STRESSES IN DISK PORTION OF BLADE - DISK ATTACHMENT
6. POINTS MARKED ⊙ REFER TO DESIGN FILLET STRESSES IN BLADE PORTION OF BLADE-DISK & ATTACHMENT
7. COOLANT FLOW IMPINGES AT RADIUS = 1.400 INCH
8. ENGINE TOTAL THROUGH-FLOW = 5 LBS PER SEC.
9. DISK & AVERAGE TANGENTIAL STRESS = 54, 500 PSI

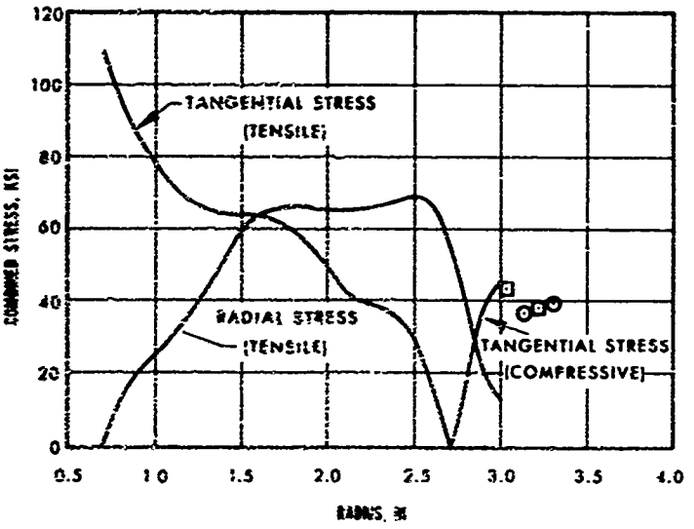

Figure 35. Calculated Combined Centrifugal and Thermal Elastic Stresses of Rotor Disk Without Shim in Place.

stock. The combined centrifugal and thermal stresses in the disk bore (Figure 35) may result in some yielding in that area. However, successful experience with similarly shaped disks operating at the same stress levels and in a similar temperature environment provides assurance that the magnitude of the predicted bore stresses will not result in low-cycle-fatigue problems.

3.3.2 Stator--Mechanical Design Studies

Detailed stress analyses were conducted on the final aerodynamic vane shape. These studies included calculations of the maximum transient thermal stresses that would occur in the vane during an engine start and also the peak bending stresses that would occur in the vane from the steady-state air loads. The results of these studies were to be used to establish the strength goals of the beryllide material (Composition 1) to be developed for stator application.

The same analytical procedures, assumptions, and computer programs that were used for the rotor blade thermal studies (Paragraph 3.3.1.1) were used for the temperature and thermal-stress analyses of the stator vane. The beryllide Composition 1 physical properties that were estimated for these studies were shown in Table VIII. While thermal-stress analyses were performed on the stator vane designs under consideration for four different engine transient temperature profiles, the data presented in this report were based on the same assumed TIT-variation-with-time temperature profile that was used for the rotor blade analyses. This temperature profile (Figure 27) was considered to be the most realistic estimate of the transient temperature conditions that would be encountered during a normal start of an engine of the design, configuration, and size assumed for this program. Calculations of the peak bending stresses in the vane due to the air loads were based on the static pressure distribution around the vane calculated from the vane velocity distributions established in the aerodynamic final design studies (Figure 23).

Since the stator vane has a fairly constant cross section with radius, the data presented for the stator studies are for the cross section located at R = 3.5694 and are considered to be representative values for all cross sections. Subsequent paragraphs describe the pertinent mechanical studies that were conducted for the stator.

3.3.2.1 Two-Dimensional Thermal and Thermal-Stress Transient Analyses of the Stator Vane

These analyses comprised several phases, which are described in chronological order on the following pages. The initial study was undertaken to calculate the heat-transfer coefficient and relative gas-temperature distributions around the vane at steady-state conditions. The calculations were based on the gas velocity distributions (Figure 23) and cycle inlet conditions. These cycle conditions, along with the resulting heat-transfer coefficient and relative gas-temperature distributions, are shown in Figure 36.

The first mechanical configuration of the aerodynamic vane design to be evaluated was a solid vane. Results of this two-dimensional thermal and thermal-stress study are shown in Figure 37. The peak thermal stress occurred as a compressive stress near the leading edge of the vane. The thermal stress and temperature distributions in the solid vane at the approximate time of maximum stress are shown in Figure 38.

The maximum thermal stresses for the solid vane are of the same order of magnitude as those calculated for the hollow first-stage blade discussed in Section 3.3.1.1 and, thus, were considered acceptable. During the analysis it was observed, however, that the magnitude of the maximum thermal stress levels in the stator vane were due, in part, to the large variation in gas velocities around the vane and the corresponding heat-transfer coefficient distribution. It was apparent that by discretely locating a radial contoured hole in the vane, these maximum stresses could be reduced. Since in the absence of beryllide material properties, the goal was to minimize the stress levels occurring in the beryllide parts, analysis was undertaken to determine the location and contour of the radial hole. Calculations were performed to determine a ratio of pressure-side-wall thickness to suction-side-wall thickness that would serve to maintain a minimum temperature difference between the two vane walls during transient conditions. The configuration established was an offset-hollow vane with wall thicknesses of 0.020 inch for the cool wall (pressure side) and 0.50 inch for the hot wall (suction side).

A two-dimensional thermal and thermal-stress study was then performed on the offset-hollow vane. Results of this study are shown in Figure 39. The peak compressive stress occurred on the pressure side of the vane just aft of the radial hole centerline, and the peak tensile stress occurred near the leading edge of the vane. The thermal stress and temperature distributions in the offset-hollow vane at the approximate

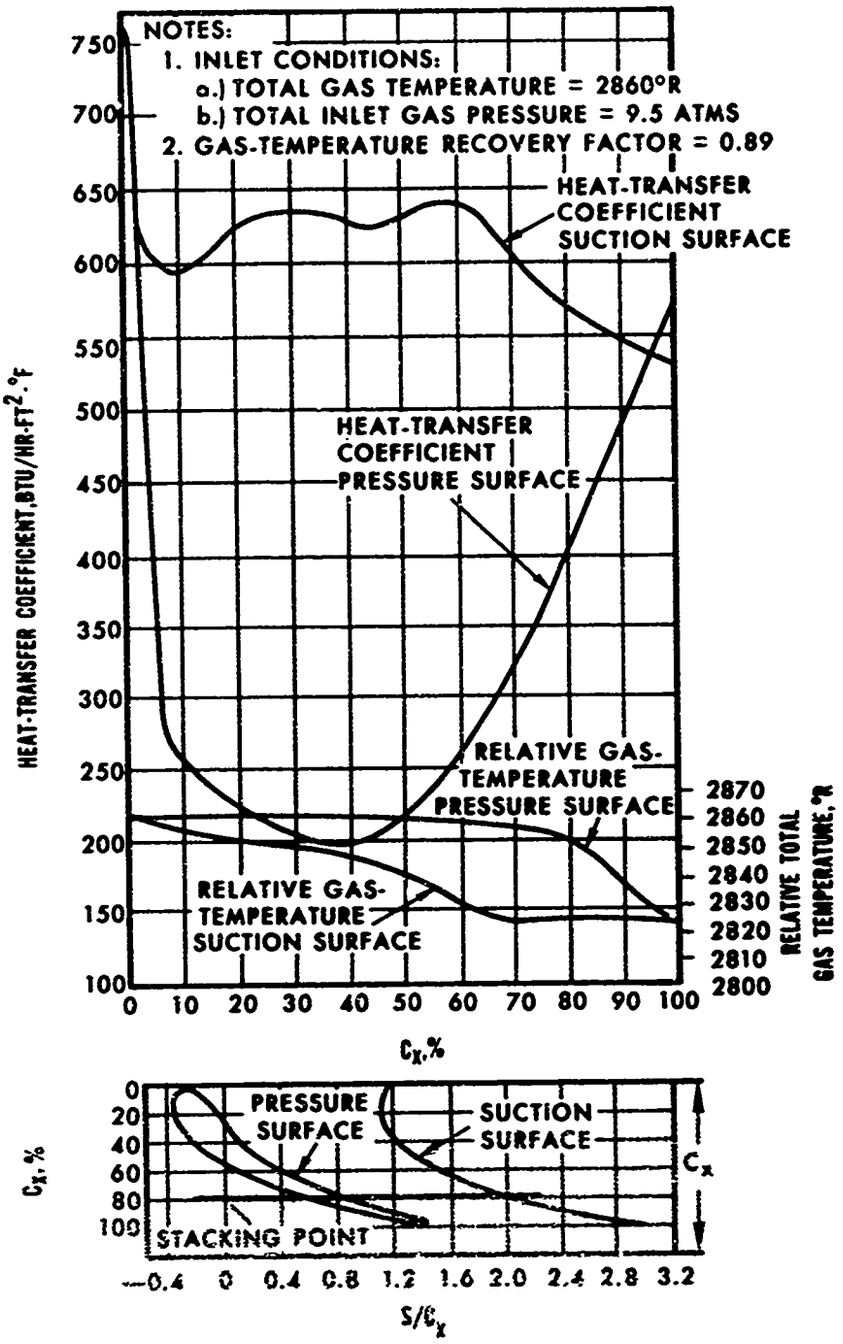

Figure 36. Steady-State Heat-Transfer Coefficient and Relative Gas-Temperature Distributions Around the Stator Vane at Section, R = 3.5694 Inches.

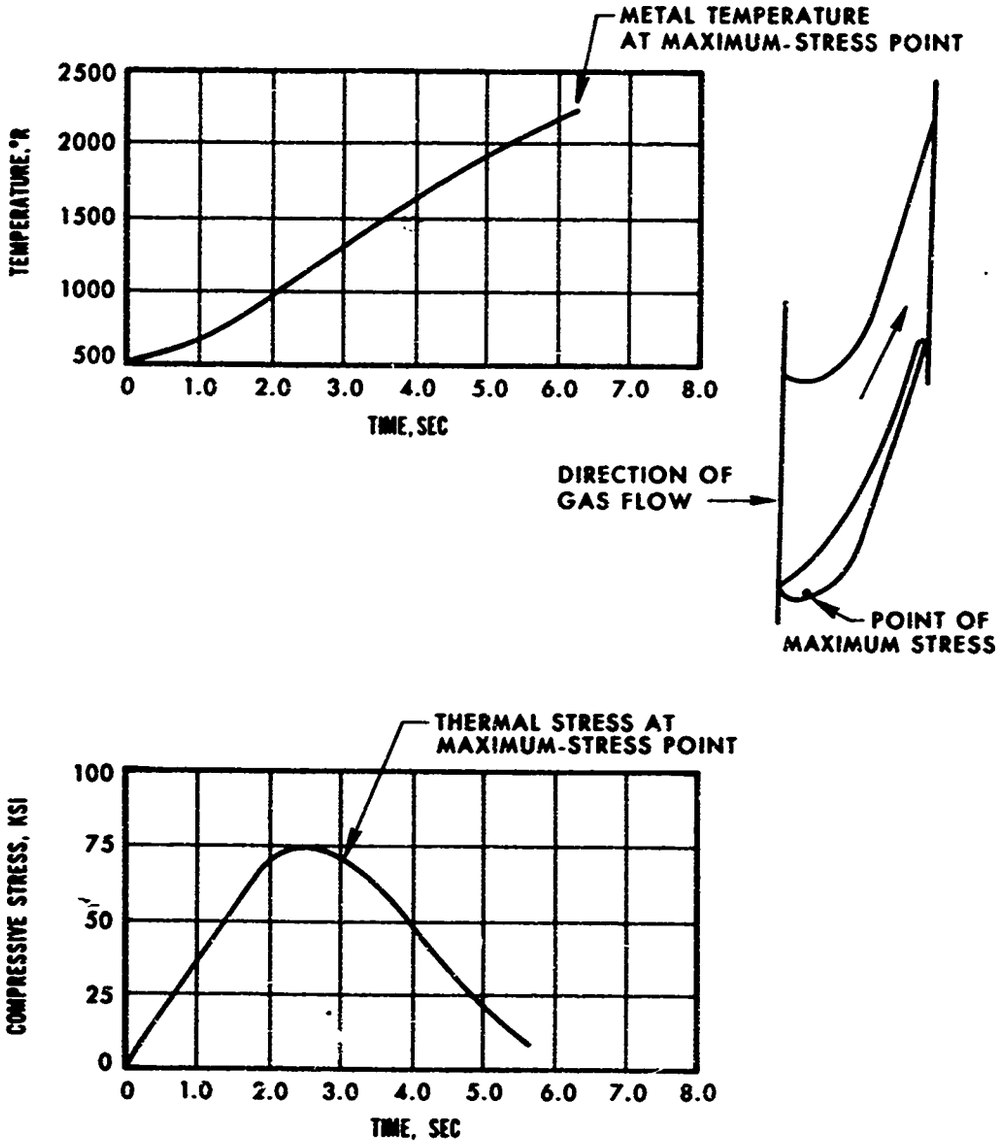

Figure 37. Transient Thermal Study of Solid Stator Vane at Section, R = 3.5694 Inches.

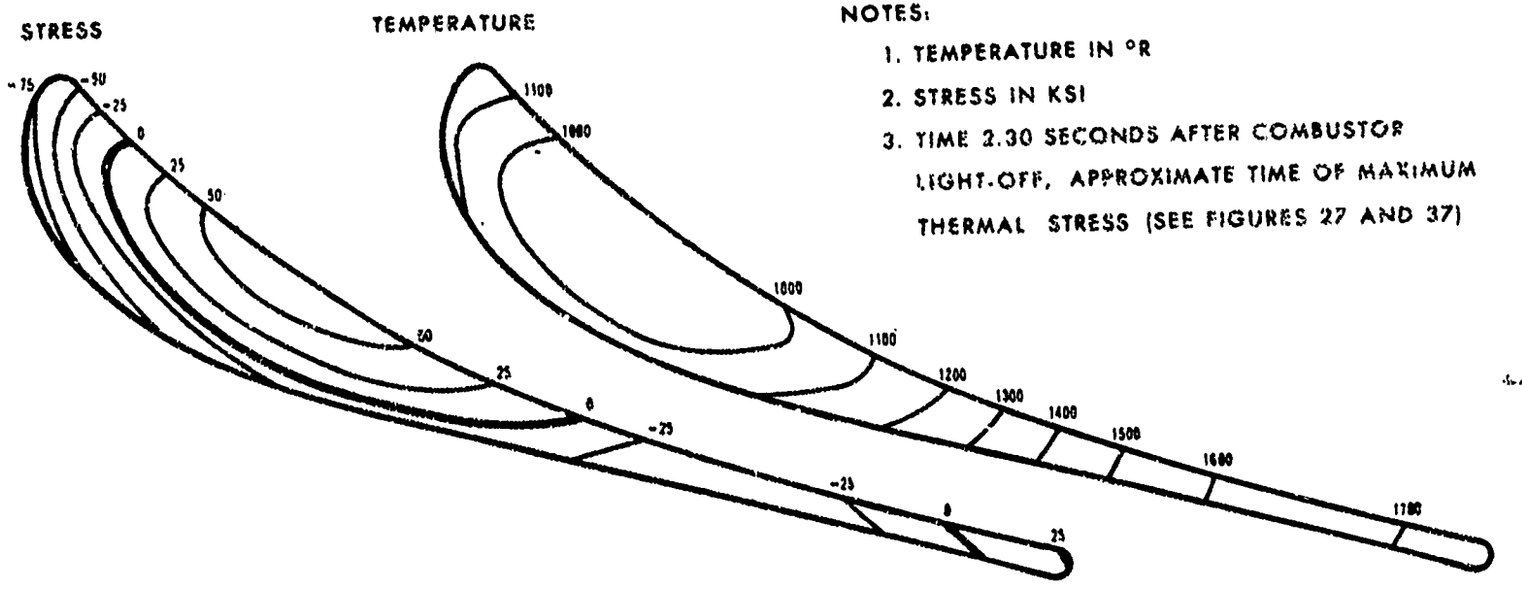

Figure 38. Stress and Temperature Distributions in Solid Stator Vane at Section, R = 3.5694 Inches.

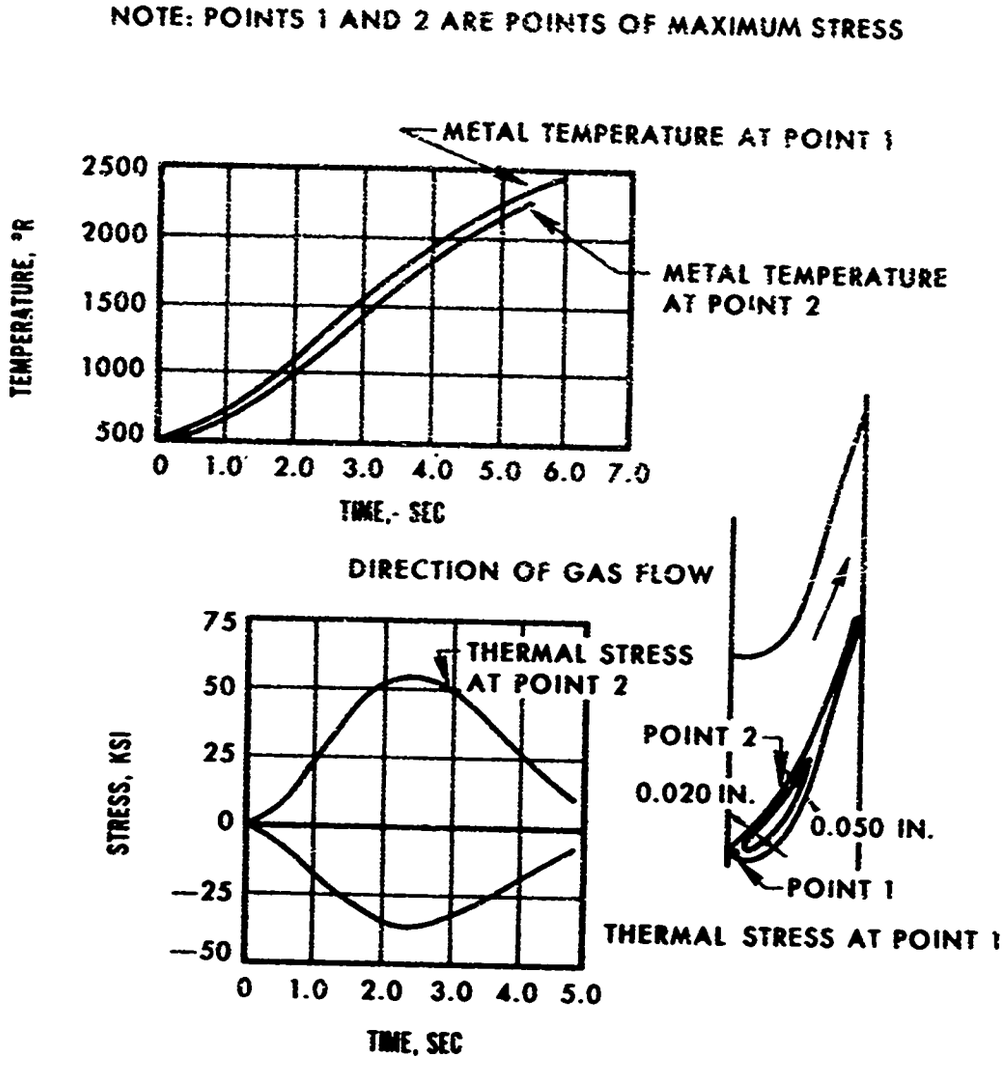

Figure 39. Transient Thermal Study of Offset-Hollow Stator Vane at Section, R = 3.5694 Inches.

NOTES:
1. TEMPERATURE IN °R
2. STRESS IN KSI
3. TIME 2.50 SECONDS AFTER COMBUSTOR LIGHT-OFF APPROXIMATE TIME OF MAXIMUM THERMAL STRESS (SEE FIGURES 27 AND 39)

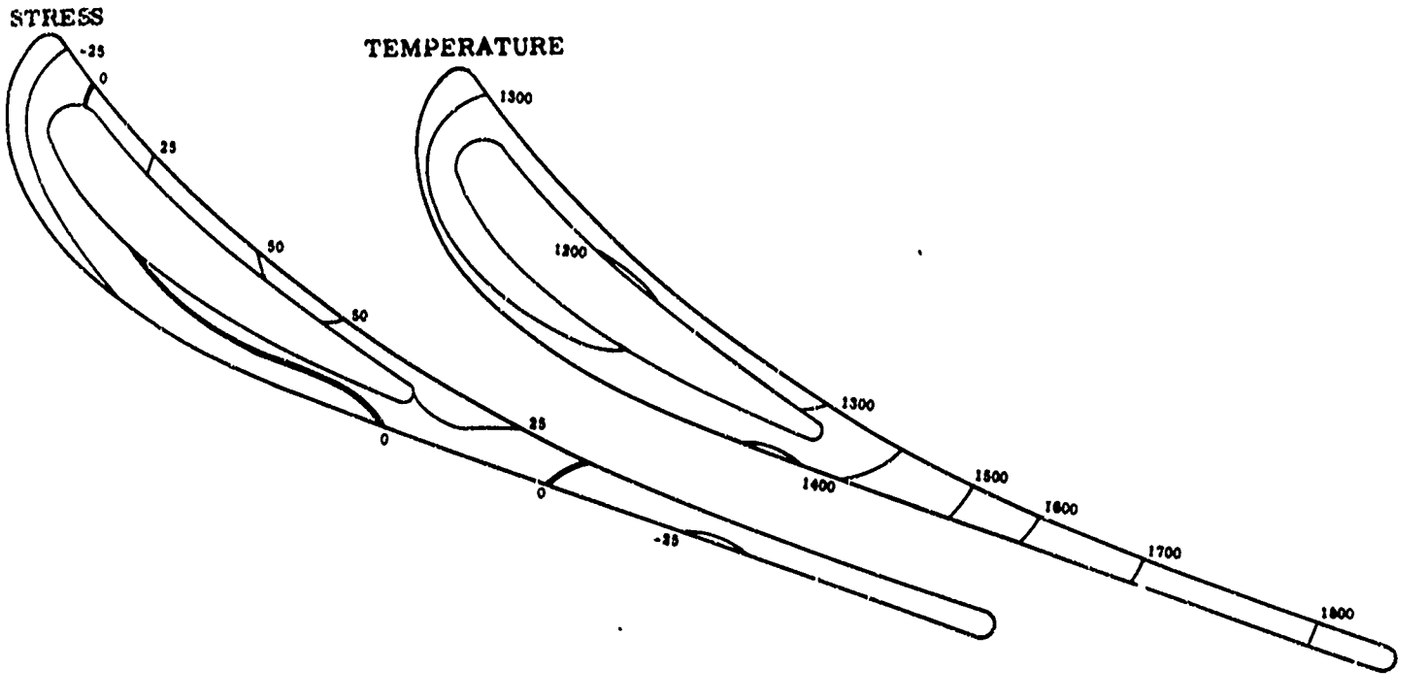

Figure 40. Stress and Temperature Distributions in Offset-Hollow Stator Vane at Section, R = 3.5694 Inches.

time of maximum stress are shown in Figure 40. The offset-hollow vane configuration resulted in an approximate 30 percent reduction of the peak thermal stresses that were calculated for the solid vane.

3.3.2.2 Stator-Vane Bending Stress Studies

Studies were made to determine the peak steady-state bending stresses in both the solid and offset-hollow vanes that result from the static pressure distribution around the vane. The calculated peak bending stresses were 11,000 psi for the solid vane and 14,000 psi for the offset-hollow vane. For both vane configurations, the peak bending stress was a tensile stress located at the leading edge of the vane where it intersects the outer circumference of the nozzle passage. Shear stresses in both vane configurations due to static pressure loading were calculated to be less than 1000 psi. Figure 41 shows the location and position of the principal axis of the vane for both vane configurations used in this study.

These steady-state bending stresses in the vane were used to establish the stress-rupture requirement for the beryllide vane material.

3.3.2.3 Stator-Vane Attachment Studies

At this time, the anticipated mechanical configuration for the stator assembly was a series of one-piece stator vanes attached to an outer ring to form the assembly. Two mechanical stator-vane attachment configurations were designed for evaluation. These configurations were identified as A and B, and are shown in Figure 42.

The static pressure drop across the stator vane was calculated to be 60 psi. This degree of pressure differential imposed considerable vane loading on the attachment and also presented a serious sealing problem in the vane attachment. Therefore, both attachment configurations were designed to ensure adequate sealing and to keep the maximum stresses in the attachment, resulting from the static pressure loading on the vane, to less than the steady-state bending stresses occurring in the vane.

Both attachment configurations were designed for use of the labyrinth provided by lap joints for sealing between the individual vanes. Also, piston ring arrangements similar to those used on the Model TPE331 Turboprop Engines were designed for the stator assembly ID to allow for small axial movements and still provide a good method of sealing. The piston rings would provide an elastic member to control the deformations of the individual vanes.

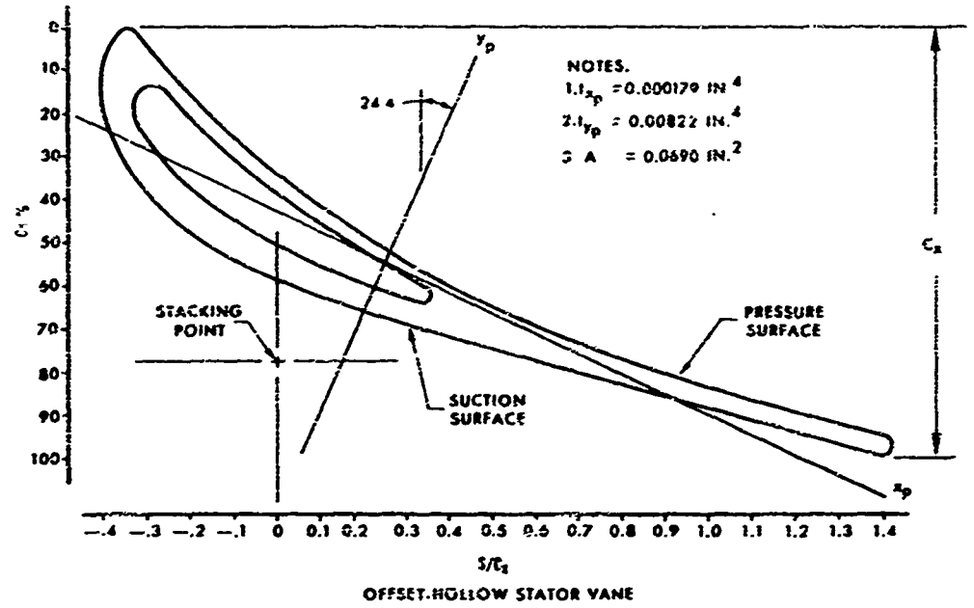

OFFSET-HOLLOW STATOR VANE

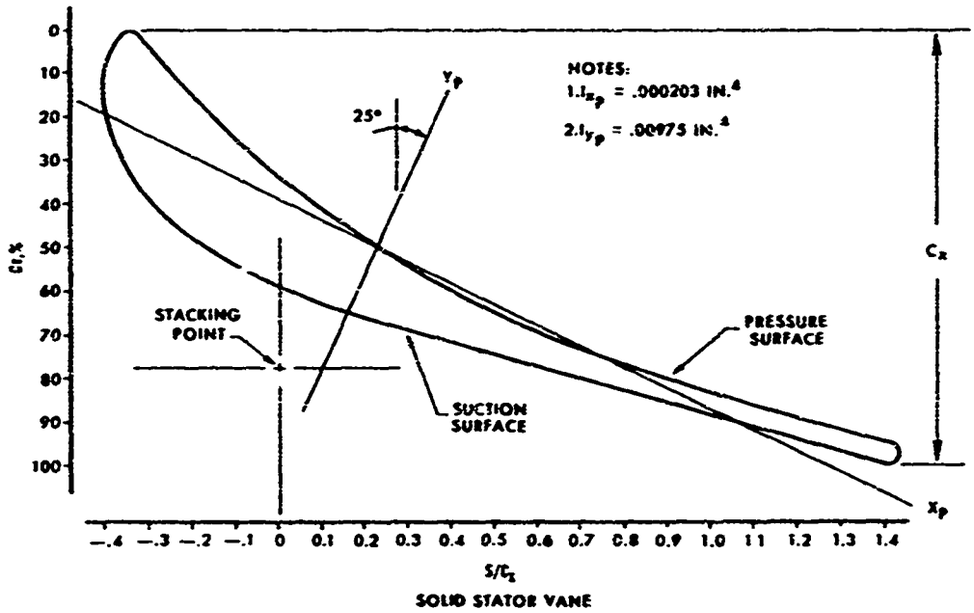

SOLID STATOR VANE

Figure 41. Locations and Positions of Principal Axis on Offset-Hollow and Solid Stator Vanes at Section, R = 3.5694 Inches.

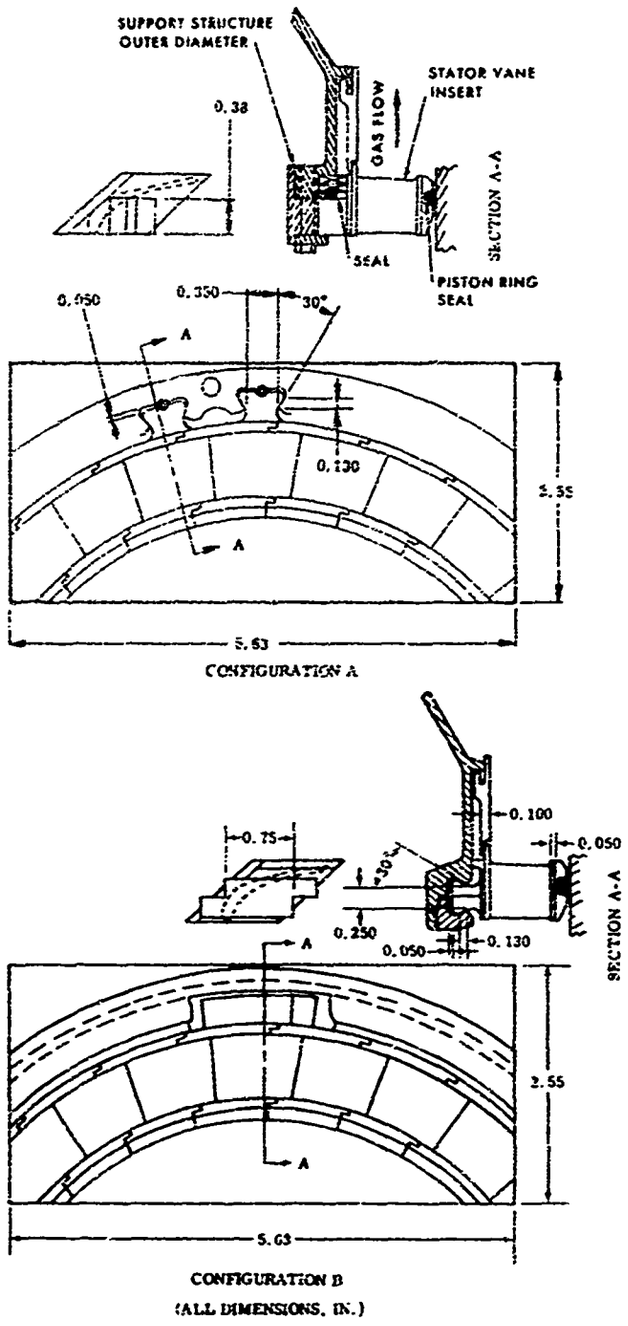

Figure 42. Stator Attachment Designs.

Two separate methods were designed to provide sealing between the stator shroud and the attachment ring. Configuration A was designed for use of a flat sealing ring clamped in place. Configuration B again employed the labyrinth of a lap joint.

The plan at this time was to evaluate both configurations experimentally during the cascade test program scheduled for the stator component. Based on the results of the cascade testing, one configuration would then be selected for the final design.

3.3.2.4 Three-Dimensional Thermal Analyses of the Offset-Hollow Stator Vane

With mechanical configurations of the stator-vane attachment established, three-dimensional thermal analyses on the offset-hollow vane with attachment Configuration B were initiated. Both steady-state and transient analyses were included.

The same computer programs and analytical procedures used for the two-dimensional analyses were used for the three-dimensional studies plus the following inclusions and assumptions:

1. Radial heat conduction in the vane was included in the study.

2. The effects of compressor discharge air scrubbing in the nozzle vanes supporting ring were included in the study.

3. For the steady-state thermal study, all the heat flowing into the vane was assumed to flow out through the vane attachment to the supporting ring located on the OD of the stator assembly.

4. For the transient thermal study, the assumed initial temperature of all metal components was 80°F. The assumed compressor discharge temperature variation with time is shown in Figure 43. The TIT variation with time used in the preceding thermal studies was again used for this study (Figure 27).

The calculated steady-state temperature distribution for the offset-hollow vane and attachment Configuration B is shown in Figure 44. The steady-state thermal study revealed that most of the nozzle vane was at or near the relative gas temperature. It was found that a rather large thermal gradient existed in the stem of the attachment portion of the vane. It was determined that this thermal gradient could present an

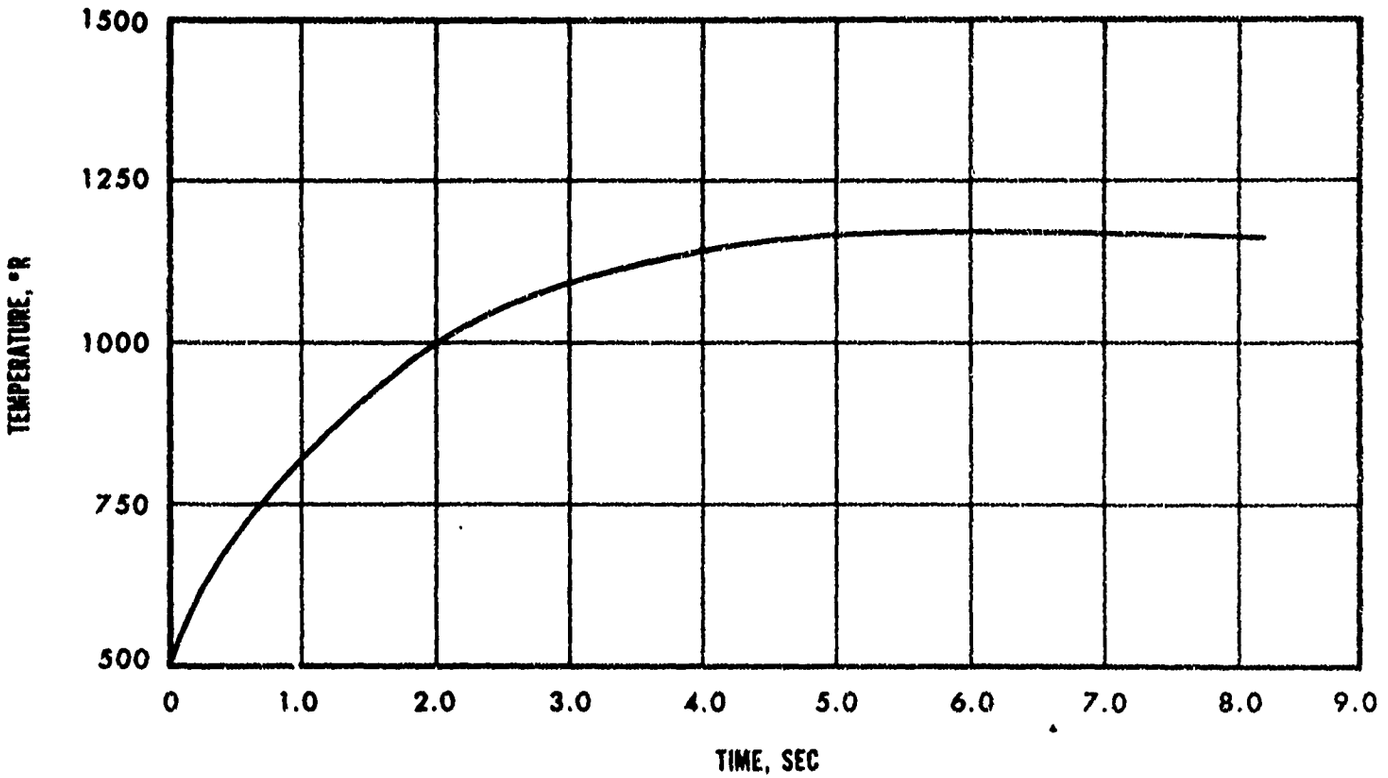

Figure 43. Assumed Compressor Discharge Temperature Variation With Time.

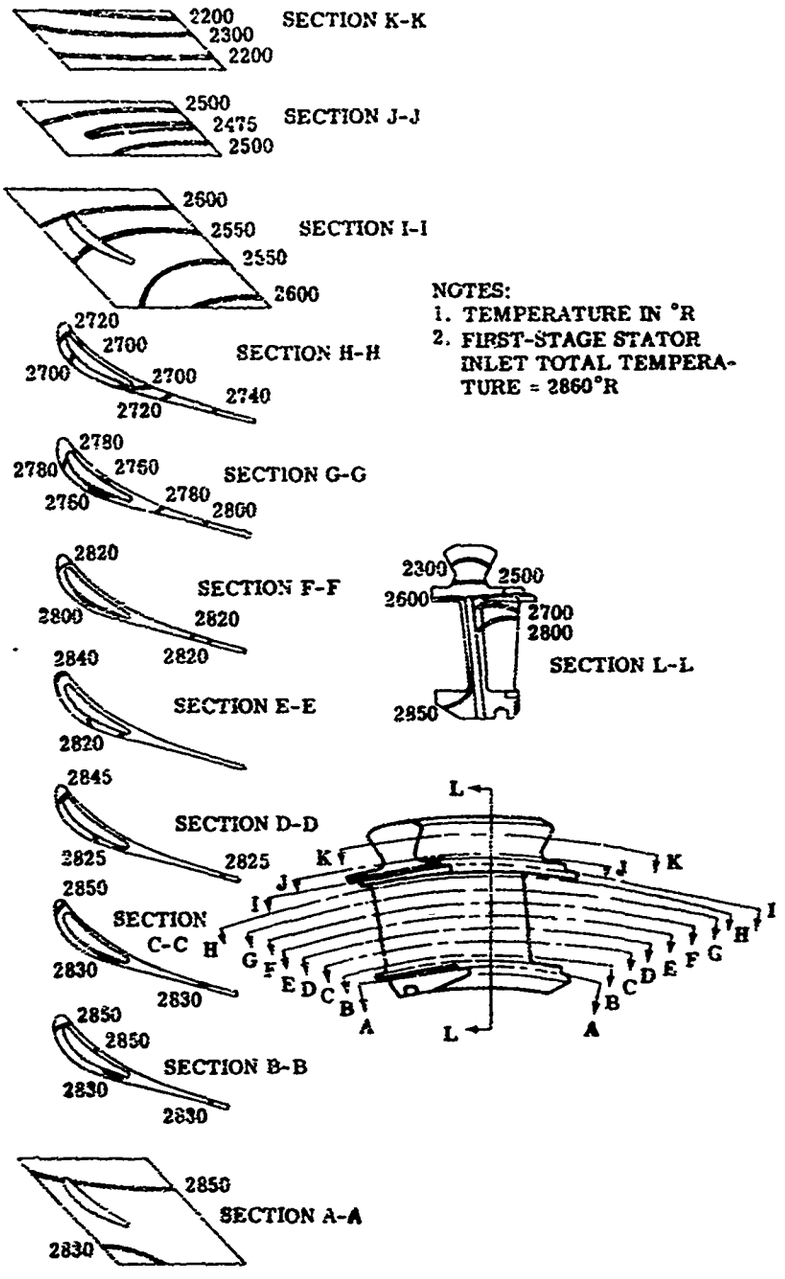

Figure 44. Three-Dimensional, Steady-State Temperature Distribution in Offset-Hollow Vane and Attachment Configuration B.

unacceptable stress problem with the one-piece vane design due to the bending imposed on the platform by the stem or dovetail and the restraint provided by the vane itself. At this time, studies were initiated to design a multiple-piece vane (described in 3.3.2.5) that would help to relieve these stresses as well as ease the fabrication problems encountered in fabricating a one-piece vane.

Results of the transient thermal study were used to evaluate the accuracy of the two-dimensional thermal study reported in 3.3.2.1. Figure 45 shows a comparison of the calculated temperatures from the two-dimensional study assuming no radial heat conduction and from this three-dimensional study assuming radial heat conduction. The temperatures shown in Figure 45 are for vane locations where the maximum calculated thermal stresses occurred in the offset-hollow vane. There is good agreement between the two analyses up to 4.0 seconds, which is well beyond 2.5 seconds--the approximate time of peak thermal stress. Therefore, it was substantiated that the two-dimensional thermal studies accurately predicted the maximum transient temperature gradients.

3.3.2.5 Multiple-Piece Stator-Vane Studies

Because of difficulties encountered in fabricating a single or one-piece stator vane (platforms and attachment integral with the airfoil portion), it was decided to fabricate each vane insert as three pieces. The insert was to include the platform and attachment portion on the outer diameter as one piece, the airfoil as one piece, and the platform and attachment portion located on the inner diameter as the third piece. Following a review of the loading on the vane, it was determined that this change would also improve the stress situation in the vane. This improvement was brought about by the method now required to support the three-piece vane.

Since it would now be an assembly of three pieces, provision for support of the vane both on the inner diameter and the outer diameter was required. The previous one-piece stator vane was essentially cantilevered from a support on its outer diameter. In the three-piece configuration, the vane was simply supported at each end, which reduced the steady-state bending stresses to approximately one-fourth of their previous value in the one-piece design. The steady-state bending stresses in the airfoil for the three-piece vane were calculated to be 2500 psi in the solid vane and 3250 psi in the hollow vane.

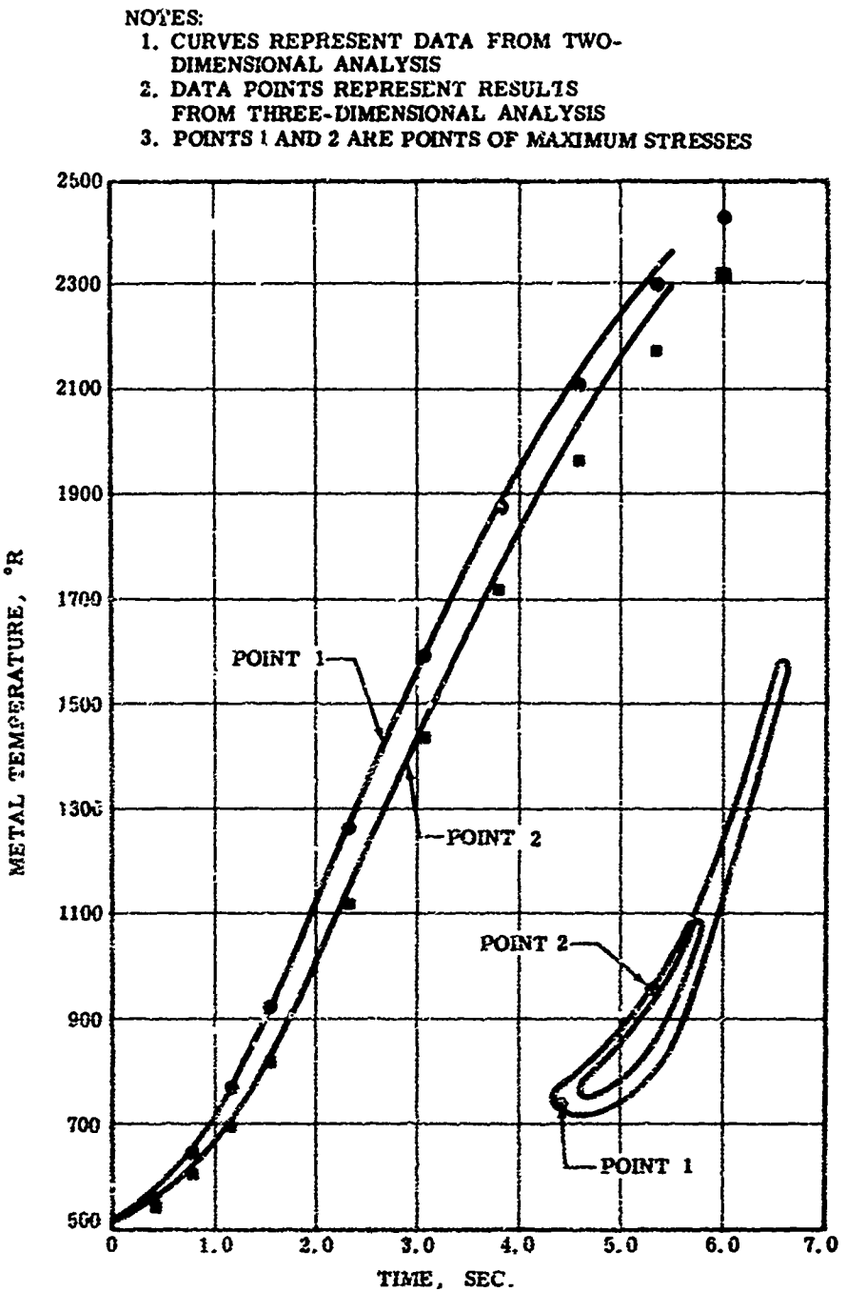

Figure 45. Comparison of Two-Dimensional and Three-Dimensional Calculated Temperatures for Offset-Hollow Vane at Points of Maximum Stresses.

Based on the results of the three-dimensional heat study (Section 3.3.2.4), no change was expected in the transient thermal stress results presented in Section 3.3.2.1.

3.3.2.6 Summation of the Stator Mechanical Studies and Cascade Test Evaluation

When the material-property data became available for beryllide Composition 1, it was found to be inadequate to accommodate the stresses occurring in the three-piece vane. As reported in Volume I, this was verified by the cascade testing where the beryllide test vanes failed in a relatively short period of time. These failures were primarily caused by insufficient low-temperature ductility in the beryllide to tolerate the peak thermal stresses occurring during starts and calculated in the mechanical studies. In addition, the material-property test results showed that the beryllide had inadequate stress-rupture strength to satisfy the steady-state stress requirements of the vane.

Although the vane steady-state stresses had been compared to the stress-rupture strength of the beryllide for 200 hours at 2400°F, a more realistic approach is to compare the stresses to the 100-hour 0.2-percent creep strength. This comparison was made by estimating the 0.2-percent creep strength to be equal to 80 percent of the stress-rupture strength. Thus, the stress-rupture strength required for the three-piece solid-vane configuration becomes 3130 psi (the calculated stress divided by 0.8) for 100 hours. The temperature used in this evaluation includes a ±200°F allowance for the circumferential spread in combustor discharge temperature. This gives a maximum expected vane metal temperature of 2600°F. With this temperature and the stress-rupture strength presented in Volume I, the 0.2-percent creep life of the Composition I solid vane is estimated to be 1.25 hours.

4. CONCLUSIONS

When the material-property tests (reported in Volume I) were completed, the resulting data were compared with the turbine design requirements calculated in the final design mechanical studies. The following conclusions were made:

1. The beryllide material had insufficient ductility for use in either the stator or the rotor components. Measurable ductility in the beryllides was not achieved below 2000°F.

2. The beryllide material had insufficient stress-rupture strength for use in the rotor component. While Composition 2 displayed adequate stress-rupture strength for the stator design (200 hours at 2500 psi and 2400°F), it did not approach the rotor design requirement.

In view of these findings, it was decided that without additional research to further develop a high-temperature turbine material, it was not expedient to continue design studies for the uncooled turbine.

5. RECOMMENDATIONS

The objective of this activity--to demonstrate the feasibility of an uncooled-turbine design--was not realized. Success of the program was precluded by the lack of a suitable turbine material. Even so, the need for such a turbine becomes increasingly greater, and the successful design of a small, high-temperature uncooled turbine should remain an ultimate goal of advanced turbine technology.

While it is advocated that no further turbine design efforts be expended at this time, it is recommended that research of high-temperature materials be continued in an effort to develop a material that would facilitate the success of an uncooled-turbine design.

APPENDIX I
GENERATION OF PRELIMINARY BLADE PROFILES

Figure 46 shows a representative blade profile, along with the definition of the geometry used. The axial chord CX and blade spacings are obtained by Zweifel's solidity requirement (reference on Page 19):

$$\frac{CX}{s} = \frac{2 \cos \beta_3 \sin(\beta_2 - \beta_3)}{\Psi \cos \beta_2} \tag{24}$$

where, for this study, $\Psi = 0.8$ (Zweifel's recommended optimum value).

From this ratio,

$$CX_i = \frac{2\pi r_i}{Z} \left(\frac{CX}{s}\right)_i \tag{25}$$

where r_i = radius of blade section

Z = number of blades

The blade profile layout (see Figure 46) is obtained by locating the center of a single arc suction-surface radius r_s so that the longest possible arc joins a tangent with blade angle β_3 at the exit and a tangent with angle β_2 at the blade leading edge. This suction-surface radius is given by

$$r_s = \frac{CX + s \sin \beta_3 \cos \beta_3}{\sin \beta_2 - \sin \beta_3} \tag{26}$$

The blade pressure surface is also a single circular arc obtained by locating a circle through two points and tangent to a trailing-edge surface t_e thick. The first point establishing the pressure surface is obtained by laying out a leading-edge thickness dimension t_a from the leading-edge intersection of the suction-surface arc. The second point on

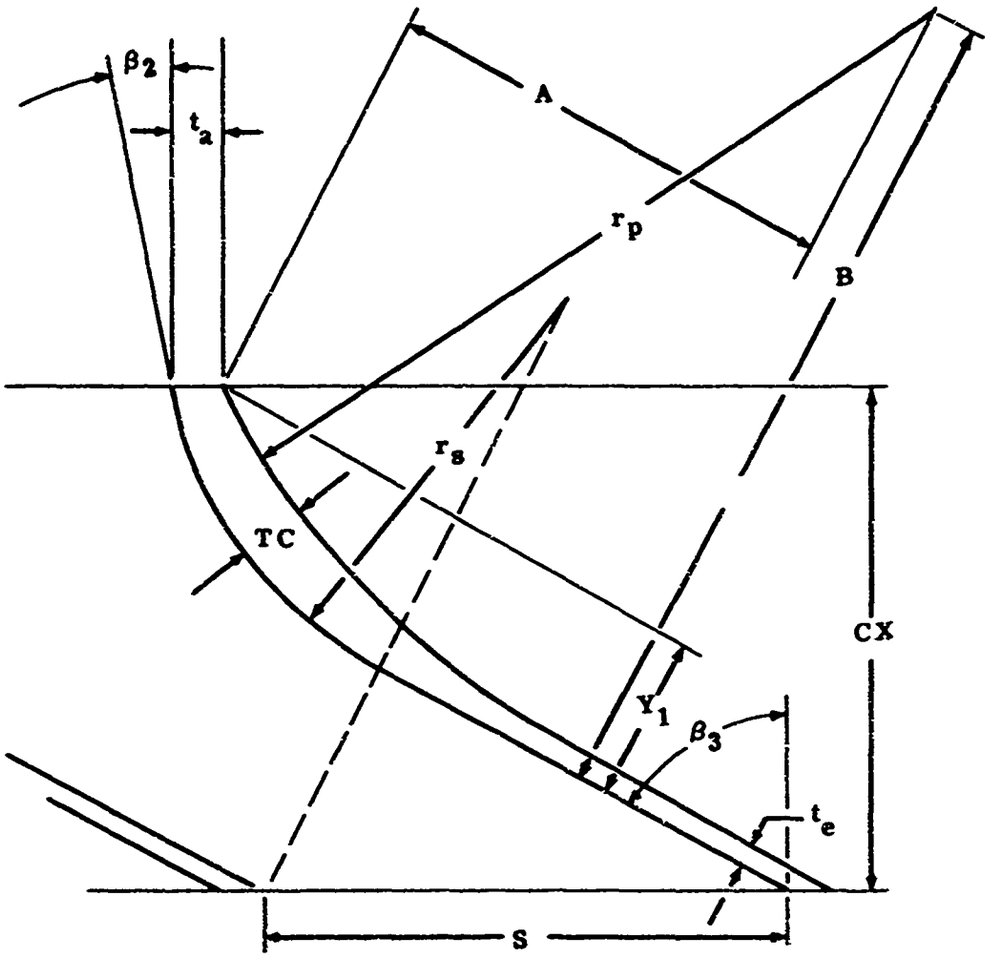

Figure 46. Blade Profile Layout.

the pressure surface is obtained by laying out a camber thickness TC on a suction-surface radius at a point halfway through the suction-surface turning angle ($\beta_2 - \beta_3$).

A computer program calculates these blade layout dimensions and the blade areas and blade moments, and integrates them to give blade volumes and radial centroids from input data β_2, β_3, γ_t, Z, t_a, TC/CX, t_e, and radius of the blade section r_i. For the turbines studied in this program, $t_a = 0.070$ and $t_e = 0.030$. These values were judged to be reasonable from a fabrication point of view.

Since the blade areas are a function of certain input parameters such as number of blades or assumed thickness parameters t_a, TC/CX, and t_e, a study of blade-area variation with two of these parameters was made for the third stage of Turbine Design A-338-5.

Figure 47 shows blade-area variation with radius for 35, 40, and 45 blades. Figure 48 shows the effect of camber thickness on blade area. These two figures were prepared for use in the stress analysis to show sensitivity to these assumptions in the blade profile layout.

NO. OF BLADES	35	40	45
BLADE VOLUME - CU. IN.	0.2780	0.2156	0.1727
RADIUS, CENTROID - IN.	3.9352	3.9359	3.9370
TC - HUB - IN.	0.2568	0.2247	0.1998
TC - TIP - IN.	0.1221	0.1068	0.0949
CX - HUB - IN.	1.7122	1.4982	1.3317

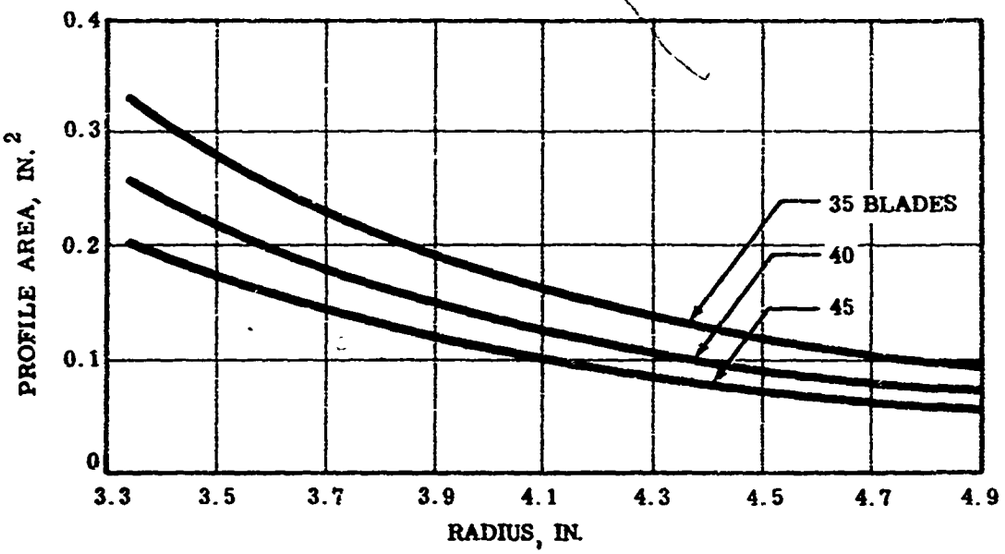

Figure 47. Turbine Blade Area Distribution Turbine Design A-338-5, Third Stage, Showing Comparison Between Different Numbers of Blades.

TC/CX	0.15	0.20
BLADE VOLUME - CU. IN.	0.2516	0.2952
RADIUS, CENTROID - IN.	3.9359	3.9478
TC- HUB - IN.	0.2247	0.2996
TC- TIP - IN.	0.1068	0.1424
CX - HUB - IN.	1.4982	1.4982

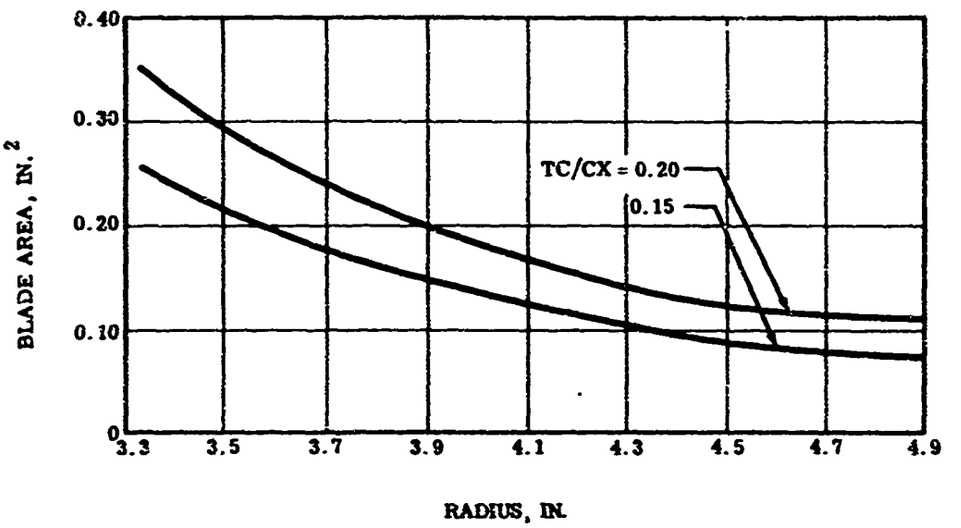

Figure 48. Turbine Blade Area Distribution Turbine Design A-338-5, Third Stage, Showing Comparison Between Different TC/CX Ratios.

APPENDIX II
METHOD FOR ESTIMATING TURBINE AERODYNAMIC EFFICIENCY

In general, turbine-blade losses can be categorized as two-dimensional profile losses and three-dimensional losses. The two-dimensional losses consist of surface friction losses due to boundary layers and downstream mixing losses due to boundary-layer and trailing-edge wakes. The three-dimensional losses consist of end-wall boundary layers, secondary flow losses, and tip clearance losses. Two-dimensional profile losses can be predicted with reasonable accuracy as long as the wake region is so thin that it has no effect on the profile velocity distribution. Three-dimensional profile losses present a more difficult problem, and experimental data are required.

For a wide variety of turbine blading, Stewart, Whitney, and Wong* have shown that the trailing-edge momentum thickness can be correlated with total blade surface diffusion by the following equation:

$$\frac{\theta_t}{\ell} = \left(\frac{0.003}{1-1.4D_t}\right)\left(\frac{3 \times 10^5}{Re_\ell}\right)^{0.2} \tag{27}$$

where θ_t = total trailing-edge momentum thickness

ℓ = mean camber-line length of blade section

Re_ℓ = blade row Reynolds number based on camber-line length

D_t = total surface diffusion parameter

* Stewart, Warner L., Whitney, Warren J., and Wong, Robert Y., A STUDY OF BOUNDARY LAYER CHARACTERISTICS OF TURBOMACHINE BLADE ROWS AND THEIR RELATION TO OVERALL BLADE LOSS, ASME Paper No. 59-A-23, 1959.

The total diffusion parameter is the sum of the suction surface and pressure surface diffusion parameters defined by:

$$D_t = D_s + D_p$$

$$D_s = 1 - \frac{V_{exit}}{V_{max}}$$

$$D_p = 1 - \frac{V_{min}}{V_{inlet}}$$

where

D_t = total diffusion parameter

D_s = suction-side diffusion parameter

D_p = pressure-side diffusion parameter

V_{exit} = average exit velocity

V_{max} = maximum velocity on the suction side

V_{min} = minimum velocity on the pressure side

These parameters are related to the blade loading diagram as shown in Figure 49.

In addition, Zweifel (reference on Page 19) has shown that the optimum blade section solidity can be related to the blade geometry by the following expression:

$$\frac{CX}{s} = \frac{2 \cos \beta_{exit} \sin \Delta\beta}{Y \cos \beta_{inlet}} \qquad (28)$$

where Y = aerodynamic loading coefficient

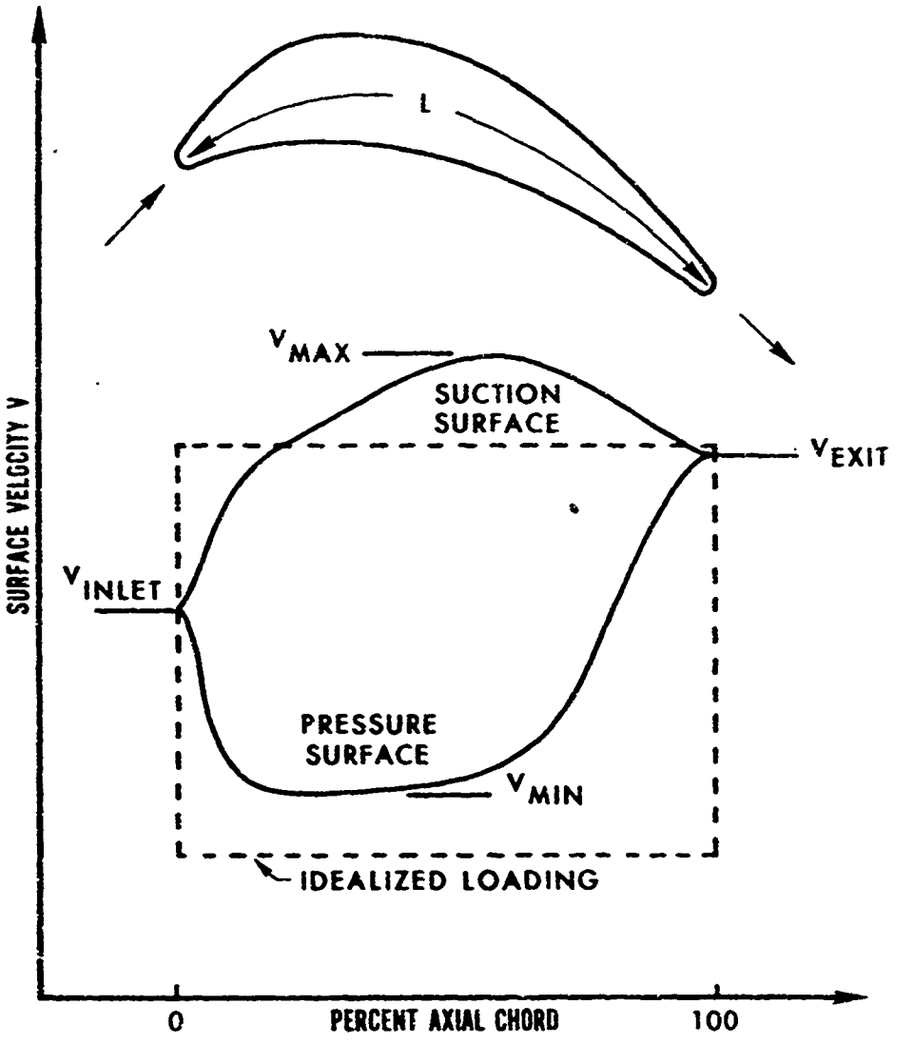

Figure 49. Blade Aerodynamic Loading Diagrams.

The aerodynamic loading coefficient Ψ is a complex function that is related to the profile suction and pressure-side velocities. If the idealized suction surface velocity were constant and equal to the exit velocity and the pressure surface velocity were zero, the loading coefficient would be unity. The parameter Ψ varies from 0.65 to 0.80 for highly loaded blades.

With the assumption of an idealized rectangular loading diagram having zero suction-surface diffusion ($D_s = 0$), the parameter Ψ can be related to the total diffusion parameter D_t by the following expression (see Figure 49):

$$D_t = 1 - \left(\sqrt{1-\Psi}\right) \left(\frac{V_{exit}}{V_{inlet}}\right) \tag{29}$$

By combining the above equations, the two-dimensional surface friction losses can be related to the blade geometry and the requirements of the vector diagram. With use of the above information, an estimate of the wake mixing losses can be made according to the Stewart method.* This method can be refined if detailed blade sections are available, since the potential flow velocity distribution about the blade profile can be calculated and the results used to determine the boundary-layer growth on the blade surfaces.

Integration of the estimated two-dimensional blade section losses over the entire blade height and correction of the results for end-wall boundary layers provide an estimated loss for the blade row. The end-wall boundary-layer correction is described by Stewart, Whitney, and Wong (reference on Page 103). Combining stator and rotor loss estimates results in a predicted aerodynamic stage efficiency, $\eta_{3D,\ A}$.

*Stewart, Warner L., ANALYSIS OF TWO-DIMENSIONAL COMPRESSIBLE FLOW LOSS CHARACTERISTICS DOWNSTREAM OF TURBOMACHINE BLADE ROWS IN TERMS OF BASIC BOUNDARY LAYER CHARACTERISTICS, NACA TN 3515, July 1955.

Tip-clearance losses in the rotor are correlated by the following equation:

$$\eta_{3D} = \eta_{3D,\ A} \left[1 - \frac{r_t}{r_m} k \frac{c}{h} \right] \tag{30}$$

where η_{3D} = stage efficiency for rotor-tip clearance equal to c

$\eta_{3D,\ A}$ = predicted three-dimensional aerodynamic efficiency at zero clearance

r_t, r_m = rotor-tip and mean radius, respectively

c = rotor-tip clearance

h = rotor-blade height

k = constant, depending on tip shroud geometry

Figure 50 shows a typical loss breakdown for a single-stage turbine for varying rotor clearance and tip shroud geometry.

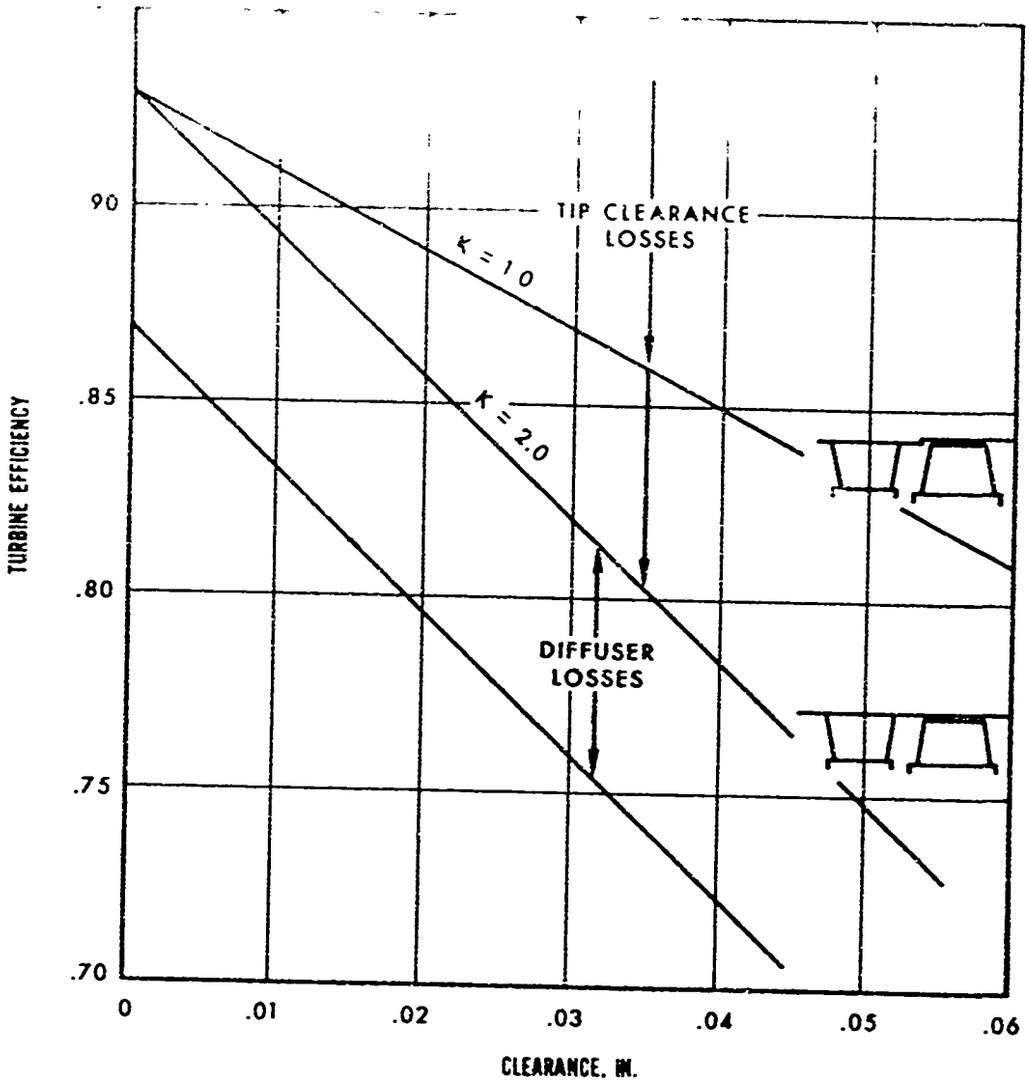

Figure 50. Attainable Turbine Efficiency.

APPENDIX III
PHOTOELASTIC TEST PROGRAM

GENERAL

A photoelastic test program was implemented to experimentally evaluate the stress distribution of the rotor disk blade fir-tree attachment configurations that evolved from the mechanical studies reported in Paragraph 3.3.1.2.2. The attachment configurations were to be tested over a wide range of loads, simulating operating conditions, while observing the corresponding stress distributions. Information gained from these tests was to be used in studies to optimize the rotor final mechanical design with respect to stress concentration in the attachment area.

The model material selected for the photoelastic test evaluation was CR-39, an allyl diglycol carbonate resin. For the results of the photoelastic testing to be applicable to the actual turbine prototype, it was necessary that certain conditions of structural similarity be satisfied. Conditions of similitude were established through dimensional analyses, and the model loads determined were used during the test evaluations.

SIMILITUDE CONDITIONS

The method for establishing similitude conditions between models and prototypes by dimensional analyses was used for the photoelastic test model.

With the assumption that both the model and the prototype behave elastically, and with consideration that for the general case the load distribution may be affected by the elastic deformation, it was found that the conditions of similitude were governed by the relationship

$$\frac{P_m}{P_p} = \frac{E_m}{E_r} \frac{\ell_m}{\ell_r} \frac{t_m}{t_p} \tag{31}$$

where the subscripts m and p refer to the model and the prototype, respectively; thus,

$\frac{P_m}{P_p}$ load ratio

$\frac{E_m}{E_p}$ modulus ratio

$\frac{\ell_m}{\ell_p}$ = scaling factor in the plane of the wheel

$\frac{t_m}{t_p}$ = scaling factor in the axial direction

For convenience, the scaling factors were made 5:1 in the plane of the wheel and 1:4 axially. The prototype (centrifugal force) load at operating speed was calculated to be 2500 pounds. Available data indicated a Young's modulus of between 10×10^6 and 30×10^6 psi for the beryllide prototype material and 0.3×10^6 psi for the CR-39 model material. The requisite model loads were then calculated to be between 31 and 94 pounds, depending on the elastic modulus of the beryllide.

If the structure were sufficiently stiff, the stress distribution would be unaffected by the deformations, and the preceding restriction on model loads would be unnecessary.

CALIBRATION TEST

The stress-optical characteristics of the CR-39 model material were determined by a calibration test of a representative tensile specimen. The fringe value for the material thickness of 1/4 inch was found to be 340 psi per fringe for the monochromatic light transmitted through the filter used. This was in agreement with the manufacturer's published value of 336 psi per fringe for light, also presumably in the blue-green portion of the spectrum.

The value obtained in the calibration test was used in the conversion of fringe value to stress value in the actual model test.

TEST DESCRIPTION

The model was made five times actual size and was patterned after Figure 51. Three blade sections were used to simulate conditions in the vicinity of the center blade on which all

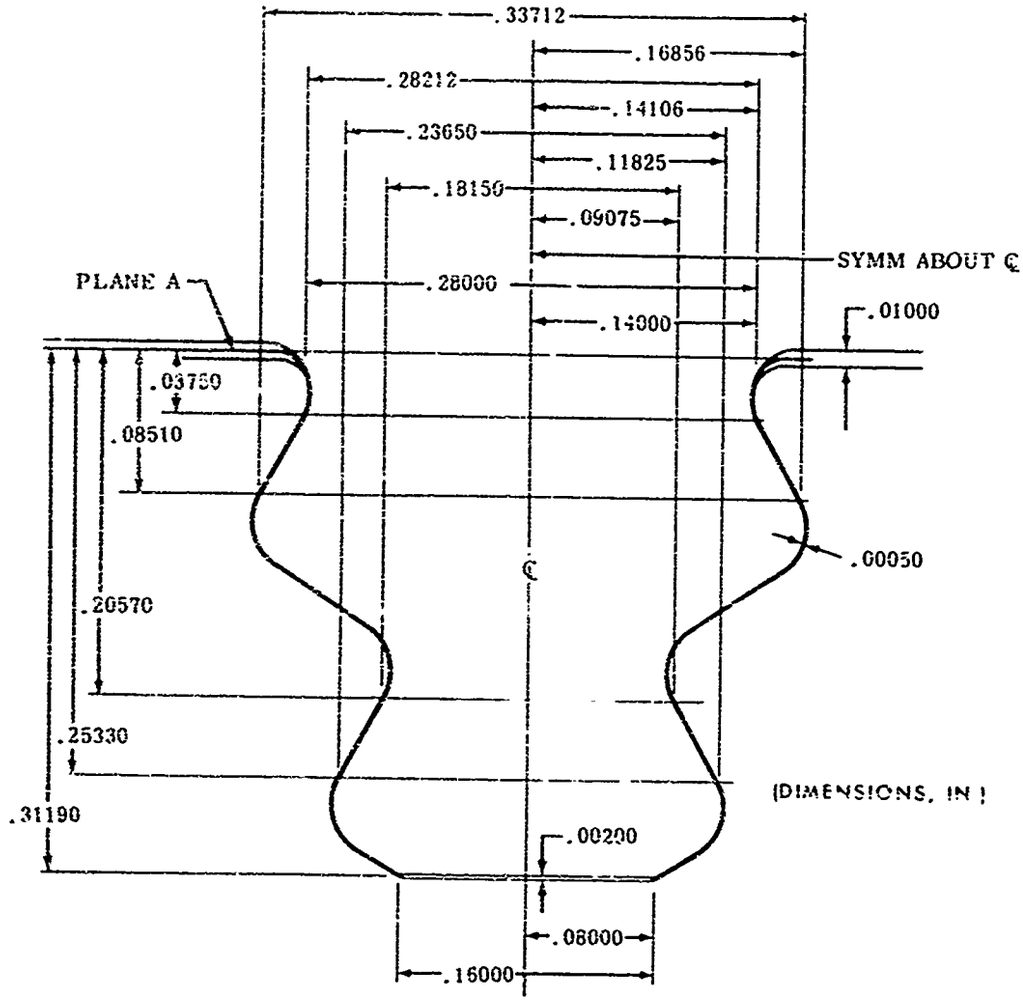

Figure 51. Layout of Fir-Tree Rotor Disk/Blade Attachment.

measurements were made.

The loading frame with the model in place in the polariscope field is illustrated in Figure 53.

Load was applied by adding water to the initially counterbalanced tank shown. This was transmitted to the model through the lever-fulcrum arrangement and a set of calibrated force rings that were instrumented to give readings of the loads on each blade. The force rings had a capacity of 200 pounds each and, with the attendant instrumentation, were capable of giving load readings to within ±0.5 pound over the entire load range. A fourth force ring of 700-pound capacity served as an added check on the total load. The force rings were threaded, which permitted equalization of load on each of the blades.

Because of the low fringe orders developed in the model at the load range of interest, attempts were made to use a quartz wedge compensator to determine fractional fringe orders. However, the high-stress gradient in the region of maximum stress resulted in a loss of distinctiveness in the fringes. As a result, this approach was abandoned.

In lieu of this, the polariscope was set for light-field, circularly polarized light, and the blade load was recorded when the 1/2- and 3/2-order fringe appeared at the point of maximum stress. Similarly, the loads were recorded on appearance of the first- and second-order fringes with the use of a dark-field polariscope. Such load readings were taken over a number of load and unload cycles of the specimen. The time between cycles (i.e., recovery period) was generally greater than 1 hour.

Finally, as an additional experiment, the model was loaded to arbitrary values in the desired load range, and the fringe values were determined at points of maximum stress to an accuracy of approximately 1/25th of a fringe.

PHOTOELASTIC RIG TESTING

Upon application of the load to the model, the lower lobes engaged first, and it was not until the blade load reached a value of 26 pounds that the upper lobes began to assume load (Figure 54).

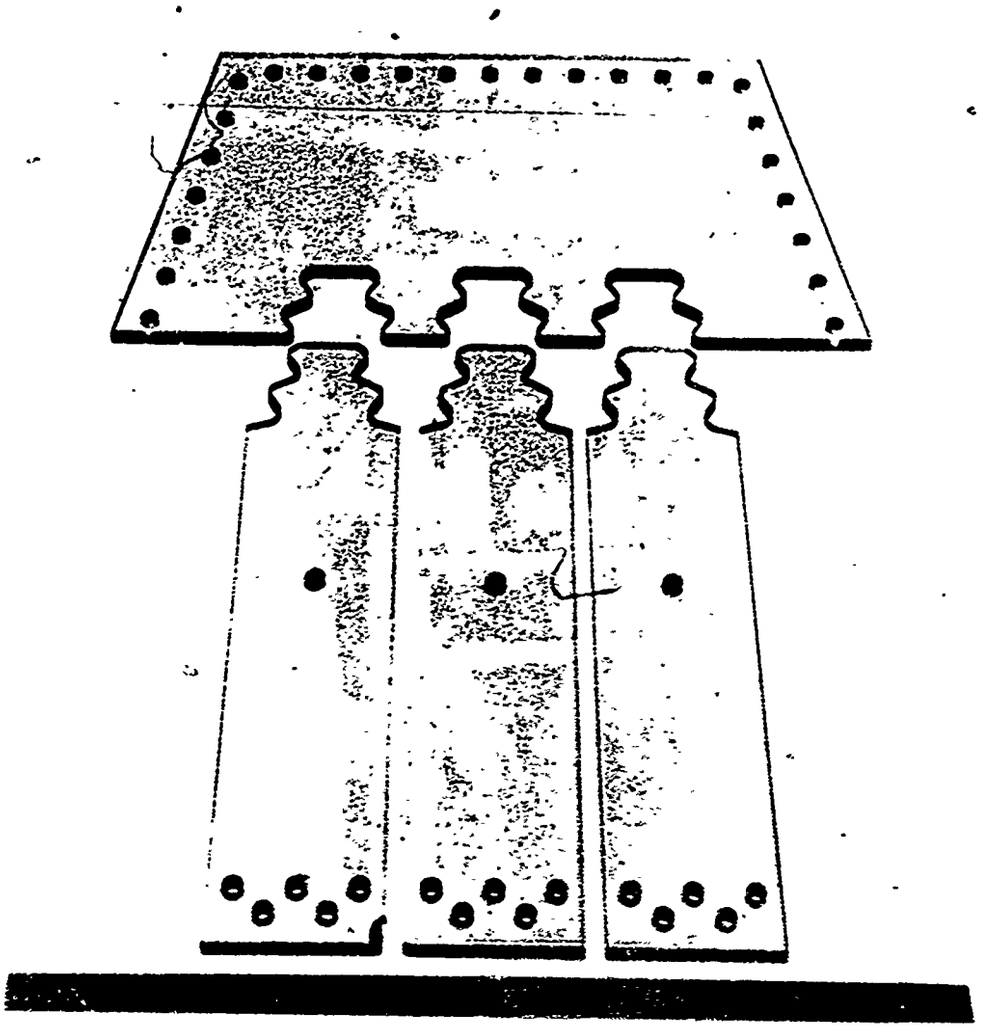

Figure 52. Photoelastic Test Model of Fir-Tree Attachment.

Figure 53. Photoelastic Test Setup of Fir-Tree Attachment Model.

Figure 54. Photoelastic Fringe Pattern Illustrating Higher Load Carried by Lower Lobes (Dark Field).

When both sets of lobes were engaged, the fraction of the total blade load carried by each set of lobes was unknown. Hence, an arbitrary average stress was defined across the minimum section between the two pairs of lobes and between the upper lobes and the blade proper as the ratio of total blade load to the corresponding minimum section area. Reference is made to the stress concentration factor (SCF), which is defined as the ratio of the maximum to the average stress, as an "apparent" or "effective" SCF. Maximum stresses in all cases were obtained from the photoelastic patterns at each load.

Results obtained for the first set of tests for the blade section between the upper and the lower lobes are given in Table XIII.

TABLE XIII. SCF BETWEEN UPPER AND LOWER LOBES

Fringe Order	Blade Load (lb)	Maximum Stress (psi)	Average Stress (psi)	Apparent SCF
1/2	16.3	170	75.8	2.24
1	34.1	340	158.8	2.14
3/2	58.4	510	272.0	1.87
2	82.0	680	382.0	1.80

Maximum deviations of individual load measurements from the average for each set of readings at a particular maximum stress level were less than 12 percent, and average deviations were of the order of 5 percent. Results given in Table XIII apply only to the case where the upper lobes do not make contact with their mating surfaces until the blade load exceeds F_o = 26.1 pounds in the model.

Analogous results of the second tests for the section between the upper lobes and the blade are given in Table XIV. Load values are accurate to within ±0.5 pound, and fringe values are accurate to within 0.04 of a fringe.

TABLE XIV. SCF BETWEEN UPPER LOBES AND BLADES				
Fringe Order	Blade Load (lb)	Maximum Stress (psi)	Average Stress (psi)	Apparent SCF
1.00	38.6	340	114	3.00
1.37	56.4	466	166	2.81
1.88	80.2	640	236	2.71

Typical fringe patterns from which the data were obtained are shown in Figures 55 and 56. Again, it should be noted that the results given above are applicable only to tolerances existing in the dimensions of the fabricated model used.

Figure 55. Typical Dark-Field Photoelastic Pattern at High Load.

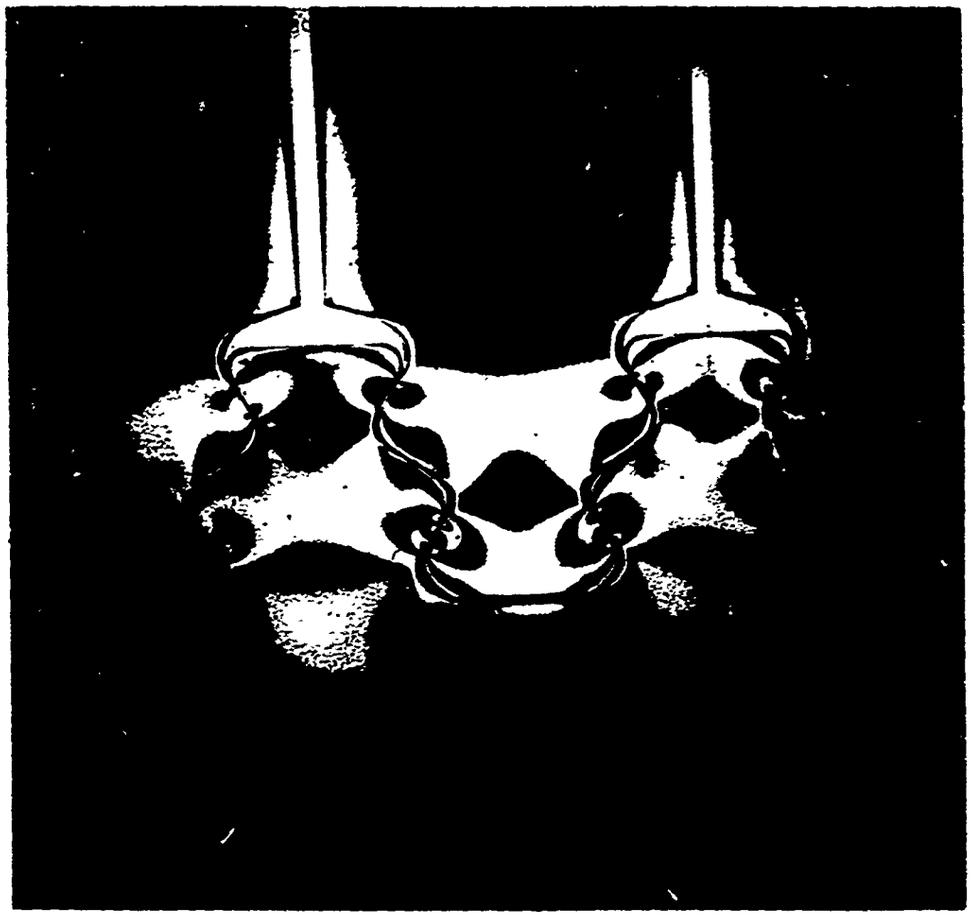

Figure 56. Light-Field Photoelastic Pattern Corresponding to Internal Load Range.

When the full blade load was carried by the lower lobes for loads less than or equal to F_o, and further loads were shared by the upper and lower lobes, then

$$SCF = K_a = \frac{\sigma_m A}{F_o + C(F - F_o)} \quad \text{for } F > F_o \tag{32}$$

and

$$K_a = \frac{\sigma_m A}{F} \text{ for } F < F_o \tag{33}$$

where F = total blade load

A = cross-sectional area (0.215 sq in.)

C = fractional load carried by lower lobes when both lobes were active at all times

σ_m = maximum stress at section for blade load, F

For fringe order 1/2, $F < F_o$ and Equation (33) were applicable, and for this case the apparent and true stress-concentration factors were identical. For the remaining cases, Equation (32) may be written in the forms

$$K_a \left[F_o + C(F_1 - F_o)\right] = \left(\sigma_{m_1} A\right) \tag{34}$$

$$K_a \left[F_o + C(F_{3/2} - F_o)\right] = \left(\sigma_{m_{3/2}} A\right) \tag{35}$$

$$K_a \left[F_o + C(F_2 - F_o)\right] = \left(\sigma_{m_2} A\right) \tag{36}$$

where the subscripts 1, 3/2, and 2 refer to the data for the corresponding fringe order. By eliminating C from the above equations, three equations for K_a were obtained:

$$K_a = \left[\sigma_{m_1} (F_2 - F_o) - \sigma_{m_2} (F_1 - F_o)\right] \frac{A}{F_o} (F_2 - F_1) \tag{37}$$

$$K_a = \left[\sigma_{m_1} (F_{3/2} - F_o) - \sigma_{m_{3/2}} (F_1 - F_o)\right] \frac{A}{F_o} (F_{3/2} - F_1) \quad (38)$$

$$K_a = \left[\sigma_{m_{3/2}} (F_2 - F_o) - \sigma_{m_2} (F_{3/2} - F_o)\right] \frac{A}{F_o} (F_2 - F_{3/2}) \quad (39)$$

which yielded, respectively, K_a = 2.34, 2.34, and 2.28. The average value obtained from the four sets of data gave K_a = 2.30. By using this value of K_a (2.30) in Equations (34), (35), and (36), C = 0.714, 0.670, and 0.674, respectively, for an average value of C = 0.686.

A fairly comprehensive picture of the stress levels expected to develop at the blade section between the upper and lower lobes for a variety of fits at the fir-tree joint has evolved. Thus, Equation (32) may be written

$$K_{eff} = \frac{\sigma_m A}{F} = K_a \left[R + C(1-R)\right] \quad (40)$$

where $R = F_o/F$ = fraction of total load at which the upper lobe first became engaged.

The effective stress concentration factor as defined by Equation (40) varied linearly with R from a value of 1.59 at R = 0 to 2.30 at R = 1.0. The maximum stress developed in the prototype at operating speed (i.e., blade load of 2500 pounds) is given as a function of R in Figure 57.

The fractional load between appearances of fringe orders 1, 3/2, and 2 was divided between the upper and lower lobes in the ratio C:(1-C). Thus, there was an independent measure of K_{eff} at R = 0. The average value so determined was K_{eff} = 1.52 as compared with the 1.59 value calculated previously.

A similar calculation for K_{eff}, the effective stress concentration factor between the upper lobes and blade, gave an average value for R = 0:

$$K_{eff} = 2.46$$

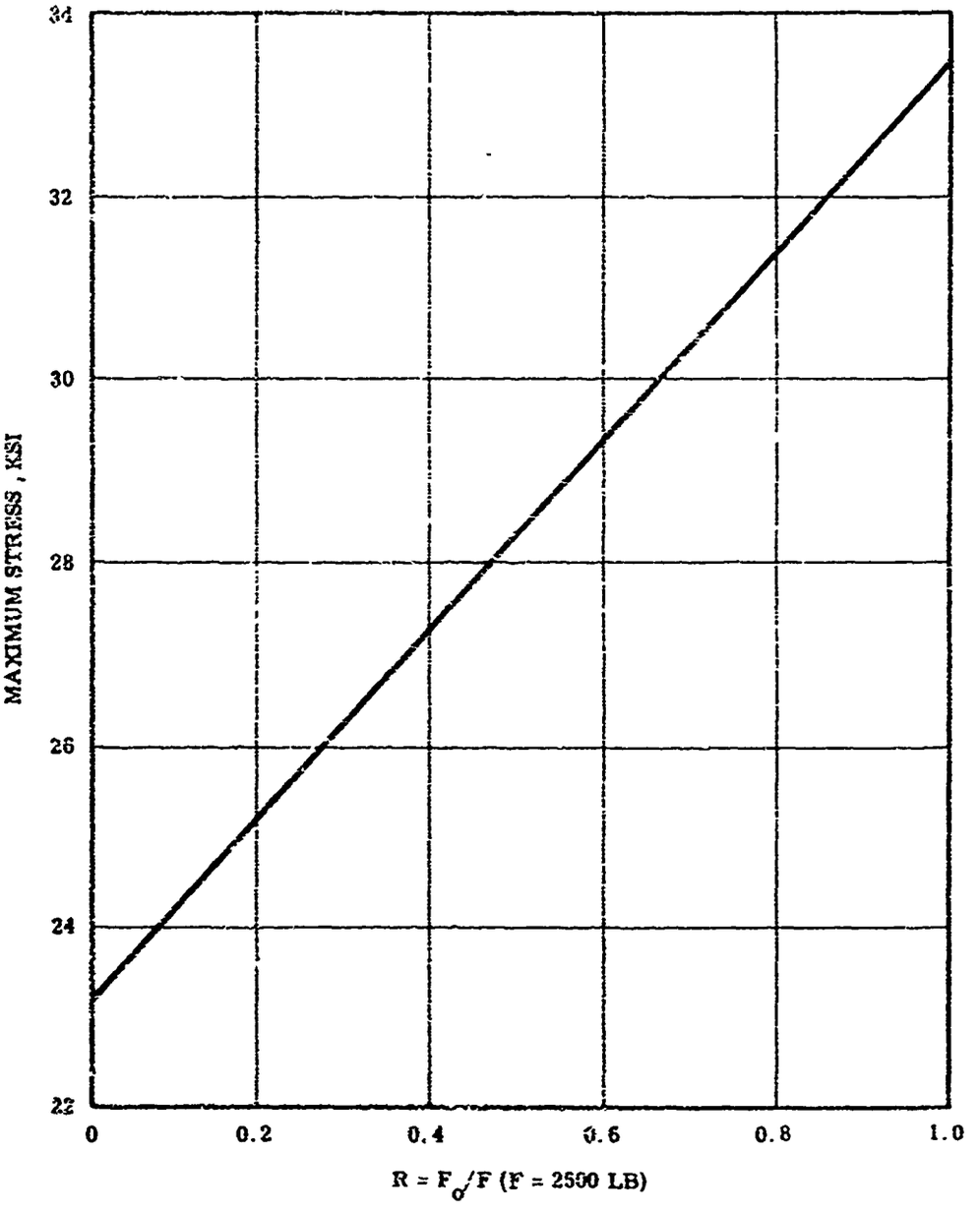

Figure 57. Maximum Root Stress Versus Fractional Load (Upper Lobe).

With simultaneous engagement of both sets of lobes, a maximum stress of 22,600 psi was expected at this section in the prototype (beryllide) blade.

The results of this photoelastic stress analysis of the fir-tree connection between the blade and hub of the 2400°F turbine wheel indicated the following:

1. With simultaneous engagement of all lobes of the fir tree, the lower lobes would carry 68 percent of the total blade load. This fraction of the total load may be reduced slightly in the prototype because of the camber on the outer boundary of the outer hub lobes.

2. The maximum stress between the upper and the lower blade lobes (23,100 psi) was about 2 percent higher than that between the upper lobe and blade proper (22,600 psi) at R = 0. This difference was less than the possible experimental error. By using the experimental value K_{eff} = 1.52 rather than the experimental value 1.59, a value 2 percent lower (rather than 2 percent higher) was obtained. With the change in stiffness due to the camber mentioned above, it was probable that for R = 0 the maximum stress would be slightly higher between the upper lobe and the blade than elsewhere in the fir-tree joint.

3. The results formed a basis for a comprehensive experimental stress-analysis program leading to improved design and establishment of allowable tolerance limits for inspection.

4. It further appeared to be desirable to investigate stress conditions resulting from nonsymmetric engagement of upper and lower lobes. This could also be accomplished through the proper use of shims.

In addition, analysis of the data indicated that the first blade model either behaved nonlinearly at low loads or had initial edge stresses introduced during machining. Further, the most recent measurements of the modulus of elasticity of beryllide had lowered the model load for similitude with the prototype to this range, which made behavior at low loads of even more significance. Therefore, a new blade model was made, and the behavior under low loads was investigated.

The stress distribution in the elements of the fir-tree configuration under load depended markedly on the deformation accompanying the load. The maximum stresses in the blade varied with the load in a nonlinear and discontinuous manner in the model tests.

Steel shim stock was placed between the disk and the upper blade lobes to ensure loading of only the upper lobes. The load was slowly applied, and the fringe order at the fillet above the upper lobes was determined at approximately every 5-pound increment of load, to a maximum total of 35 pounds.

During loading, it was noticed that the increment of fringe order accompanying the load increase from 22 to 27 pounds was of a larger magnitude than the fringe order over equal load increments. Therefore, the load was reduced from 35 to approximately 22 pounds to give an additional check measurement of the fringe order at that load. All of the load was then removed, and the specimen fringe order was again zero, as at the start of the load cycle.

The test data were then reduced to give absolute fringe order as a function of load, and the results were plotted as shown in Figure 58. The data defined two apparently separate curves. Equally surprising was the difference in fringe order at a 22- to 23-pound load obtained on the loading-versus-unloading cycle.

The only explanation for the phenomena described above is that the load distribution at the loaded blade-disk interface changes suddenly (i.e., discontinuously) at a load somewhere between 22 and 27 pounds on loading and at some load below 23 pounds on unloading. The discontinuity is caused by sticking and slipping of one contacting surface against the other.

There was again some evidence of the stick-slip process when the shims were moved to give contact at the lower blade lobes only. However, this occurred at smaller load increments, and it was possible to plot a continuous curve for maximum stress versus load as shown in Figures 59 and 60. These latter curves also indicated bending of the blade in addition to the tension. This is shown by the difference in stress at the two fillets between the lower and upper blade lobes.

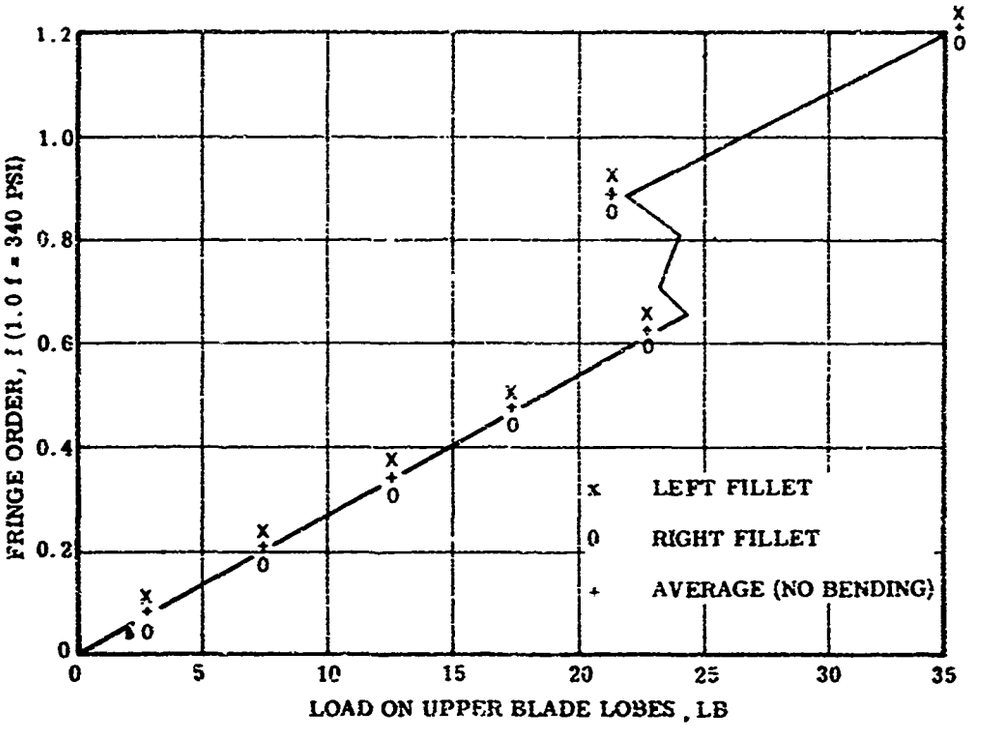

Figure 58. Model Stress Above Upper Blade Lobes (Load on Upper).

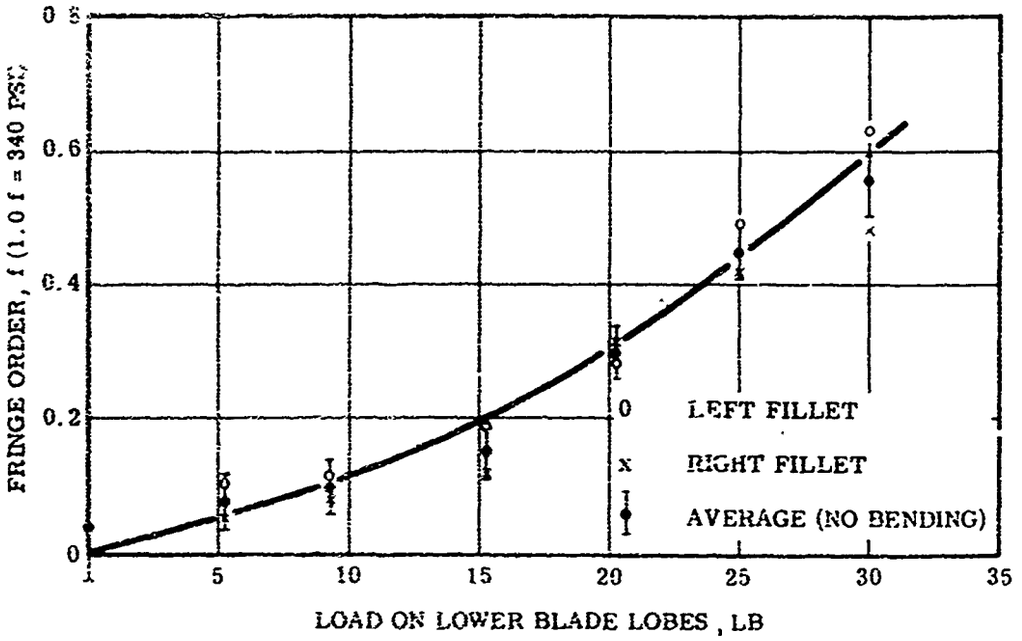

Figure 59. Model Stress Above Upper Blade Lobes (Load on Lower).

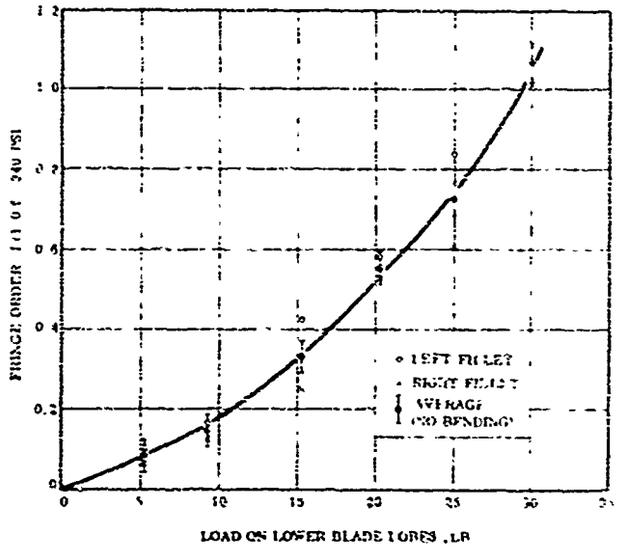

Figure 60. Model Stress Between Upper and Lower Blade Lobes (Load on Lower).

The nonlinearity of maximum fillet stress as a function of load is due to the influence of elastic deformations on stress distribution in the fir-tree configuration. Thus, in addition to geometrical similitude of the photoelastic model and its prototype, there must be similitude in load distribution if photoelastic data are to be applicable to the turbine itself.

When the relationship between the applied model load P_m and the prototype load P_p was derived, it was recognized that, should deflections influence load distribution, a further problem could arise with regard to its applicability for the following reason: in the model, both the disk and the blade were of the same material (CR-39), having a value $E_m = 3 \times 10^6$ psi; while in the prototype, the disk was of IN-100 ($E_p = 24 \times 10^6$ psi) and the blade was of beryllide ($E_p = 39 \times 10^6$ psi). This became a real problem when interpreting the results obtained in terms of prototype stress levels to be expected.

In contrast, the result for the disk (Figure 61) is singularly linear. The probable explanation for this is that during the slipping process, all of the relative motion occurred between the blade and the shim, so that the load distribution on the disk model remained ostensibly unchanged.

The redistribution of load in the prototype may be expected to differ from that in the model for two reasons: (1) the difference in elastic modulus of the blade and disk materials and (2) the vibration of the engine during loading, which may eliminate the stick-slip process (the change in load distribution would be a continuous process).

Despite the limitations of the model studies, useful design information may nevertheless be obtained from the photoelastic results.

The prototype stresses were calculated at the three critical fillet sections in the blade and disk on the assumption that both the blade and disk material was IN-100 and recalculated on the assumption that the material was beryllide. These stresses were plotted as functions of the percent of full load (2500 pounds) carried by the upper and lower lobe pairs in Figures 62 and 63. The discontinuity shown in Figure 58 was "faired" out in developing the upper curves in Figure 63.

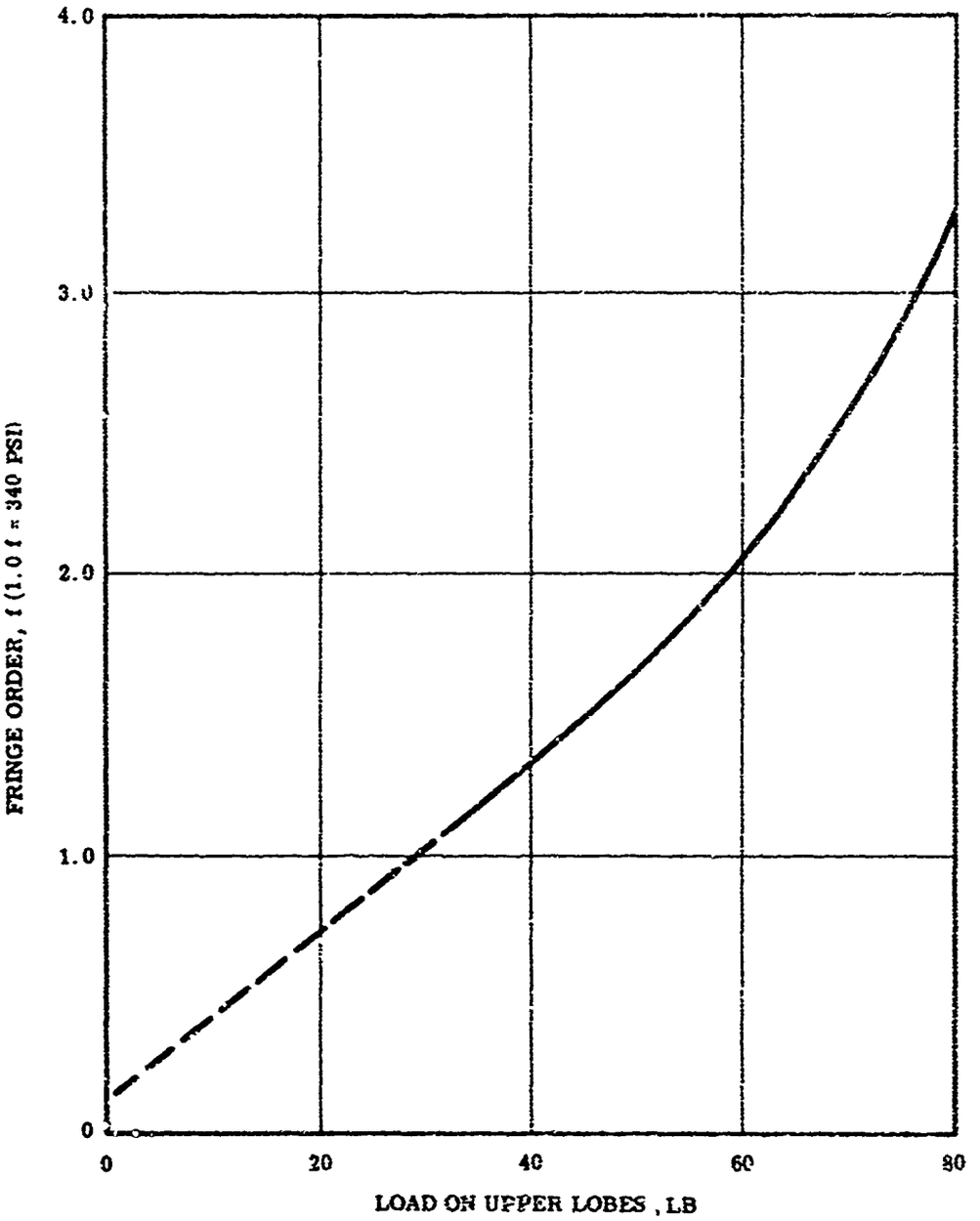

Figure 61. Model Stress in Disk Versus Load in Upper Lobes.

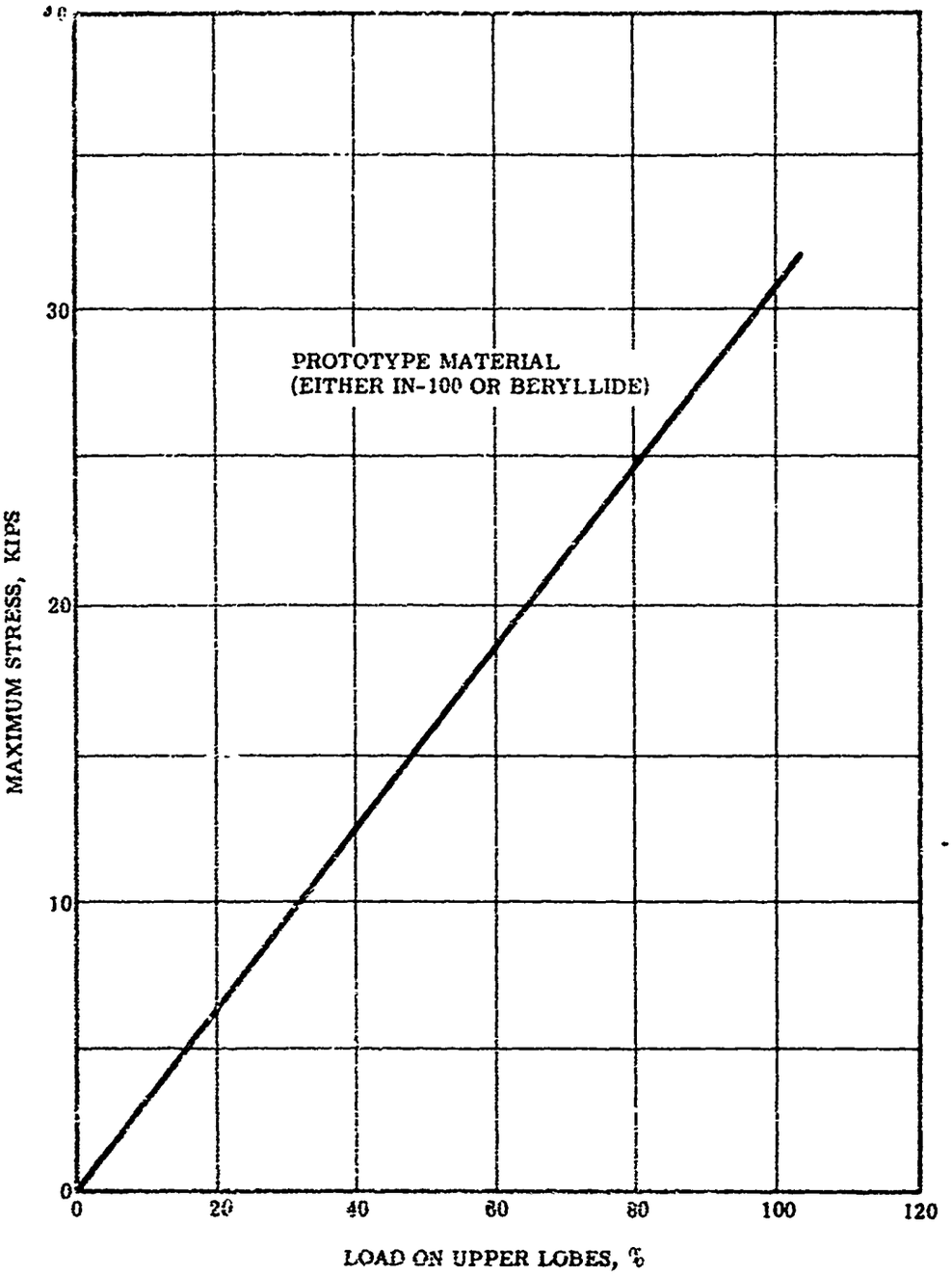

Figure 62. Maximum Disk Stress Versus Percentage of Load Carried.

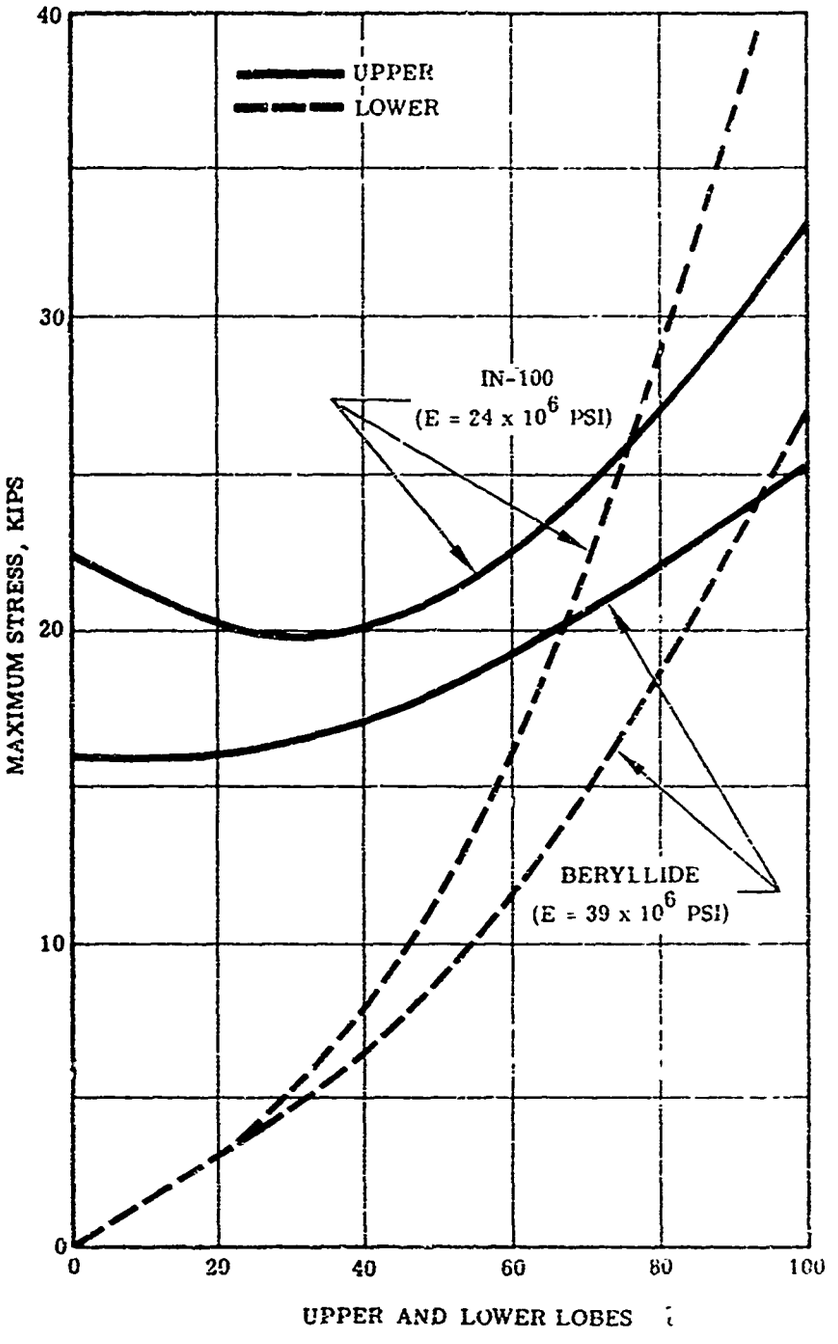

Figure 63. Maximum Blade Stress Between Upper and Lower Lobes and Above Upper Lobes.

The curves of Figure 63 are labeled with regard to similitude with a material having $E = 39 \times 10^6$ psi (beryllide) or one having $E = 24 \times 10^6$ psi (IN-100). For the case of a beryllide blade and an IN-100 disk, the blade stresses would be higher than those shown by the lower curves, and use of the upper curves for design purposes would not be overly conservative.

PHOTOELASTIC TEST CONCLUSIONS

Review of the photoelastic test results revealed that the indicated stresses were somewhat lower than those calculated during the fir-tree attachment design studies. However, as reported in the design studies (Paragraph 3.3.1.2.2), there were a number of minor differences between the fir-tree attachment modeled in the photoelastic tests and the fir-tree attachment analyzed in the design studies. Thus, care was exercised when comparing the stresses from the two studies.

The major contribution of the photoelastic test was the data on the relative effects of tolerances and load sharing between the lobes. This information made the photoelastic testing a valuable tool in establishing the final fir-tree configuration.

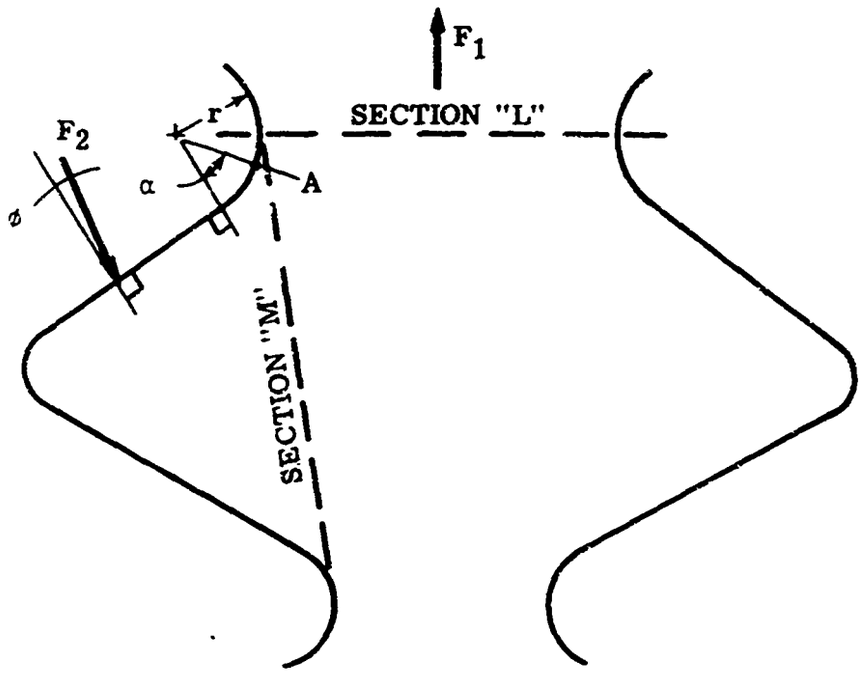

Figure 64. Loading Considered in Fir-Tree Analysis.

APPENDIX IV
THERMAL-CONDUCTION TEST PROGRAM

GENERAL

The tests described in this appendix were conducted to determine the thermal conductance across the interface of the beryllide and IN-100 contacting surfaces in the two-lobe fir-tree disk/blade attachment.

CONDUCTION RIG DESIGN

The instrumented test specimens consisted of two IN-100 cylinders 0.75 inch in diameter over a length of 1.5 to 2.0 inches (Figure 65). The upper specimen had an enlarged section 1.25 inches in diameter at its upper end, which was heated by an induction coil. The lower specimen terminated in a block approximately 4 x 4 x 2.5 inches, in which provision was made for circulating cooling water.

The ends of the specimens away from the enlarged sections were ground to a finish of rms 20-24. Thermocouples were attached to the specimens along the heat flow path. The four thermocouples on the circumference and the thermocouple on the specimen axis at axial stations 0.125 and 0.875 inch from the interfaces (i.e., the specimen ends) served to give a measure of the uniformity of temperature and load, over the specimen cross sections. Additional thermocouples 0.5 inch from the interfaces and at the specimen axis were used in conjunction with the others to measure the axial temperature distribution. The thermocouple installation is shown in Figure 66.

With these two specimens, it was possible to directly measure the interface resistance to heat flow or its reciprocal, the thermal conductance of the interface, as a function of the pressure. However, specimens of the beryllides could not be satisfactorily instrumented and were, therefore, fabricated as thin disks 0.75 inch in diameter and 0.0625 and 0.125 inch thick. These disks were ground-finished on both sides to 16 rms and presented two interfaces with the IN-100 specimens. For comparison, an IN-100 disk 0.125 inch thick was also fabricated and finished to the same rms value.

During the tests, thermal insulation was packed around the specimens over the full length of the 0.75-inch-diameter sections while the specimens were in alignment and under a compressive load of about 200 pounds.

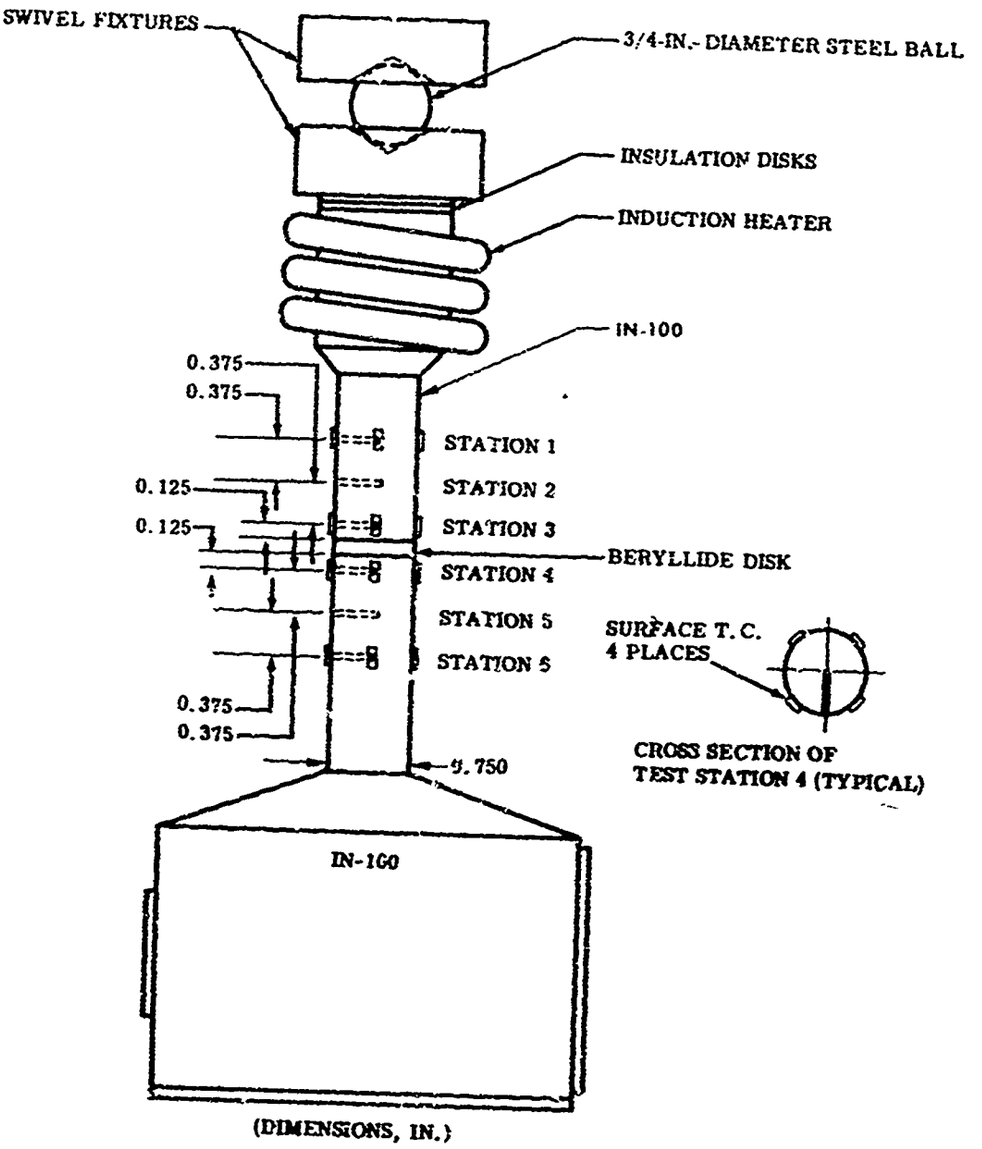

Figure 35. Conduction Rig Test Setup.

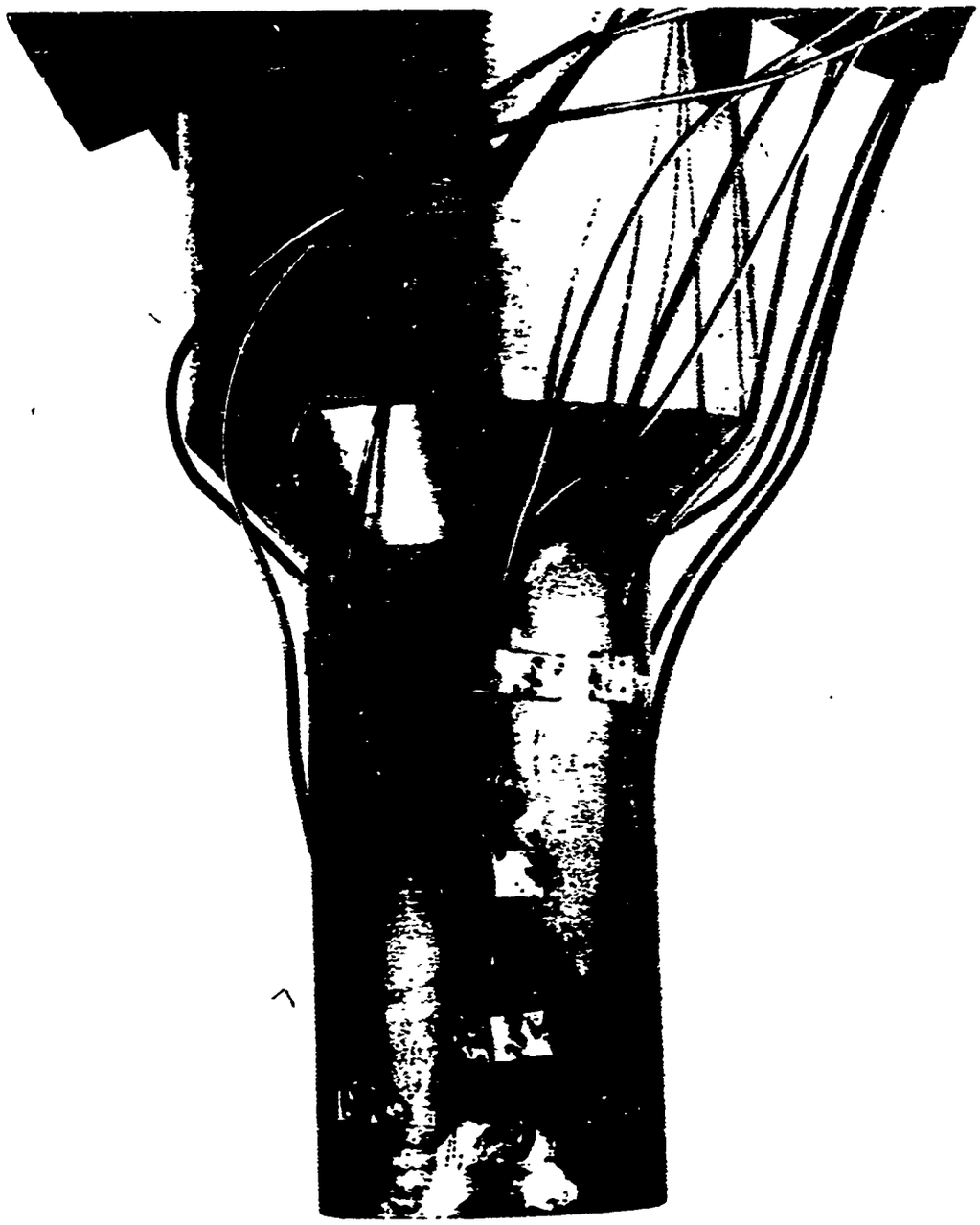

Figure 66. Thermocouple Installation.

CONDUCTION RIG TESTING

Loads were applied to the specimens through a spherical seat loading head by a hydraulic test machine, with power to the induction heating coil supplied by an oscillator. Tests were conducted at interface pressures of 100, 1000, and 2000 psi. Thermocouple readings were taken every 15 minutes until steady-state conditions were reached for each load.

The thermal conductivity variation with temperature for IN-100 is given in Figure 67 and was used to determine the heat flow across the interface. Similar data for beryllide are also given in Figure 67 and were used to calculate the temperature drop across the beryllide disk.

Temperatures measured on the circumference of the specimen at Station 1 were 40° to 50°F higher than those on the axis. A similar difference was observed at Station 6, but with temperatures on the circumference lower than those on the axis. This was due to the shortness of the transition distances between the heat source and heat sink and the instrumented test length of the specimen. However, the variation in temperatures as measured at Stations 3 and 4 was of the order of 10°F in each case, and the average temperatures were within a degree or two of the axis temperatures.

The average interface temperature in the tests with the beryllide disks was 1109°F; with an IN-100 disk, it was 1064°F; and with IN-100 versus IN-100 (a single interface), it was 873°F.

Calculated contact resistances based on the test data are in reasonable agreement with the sparse published values available in the literature for interface temperatures and pressures considered in Table XV.

Differences in contact resistance among the various test configurations were not considered to be large, in view of the individual differences between the characteristics of the contacting surfaces in each test, the differences in relative orientation of tool marks on contacting surfaces, etc.

The thermal contact resistance between IN-100 and beryllide as measured in these tests was roughly one-half as large as the value assumed in the design phases of the uncooled turbine.

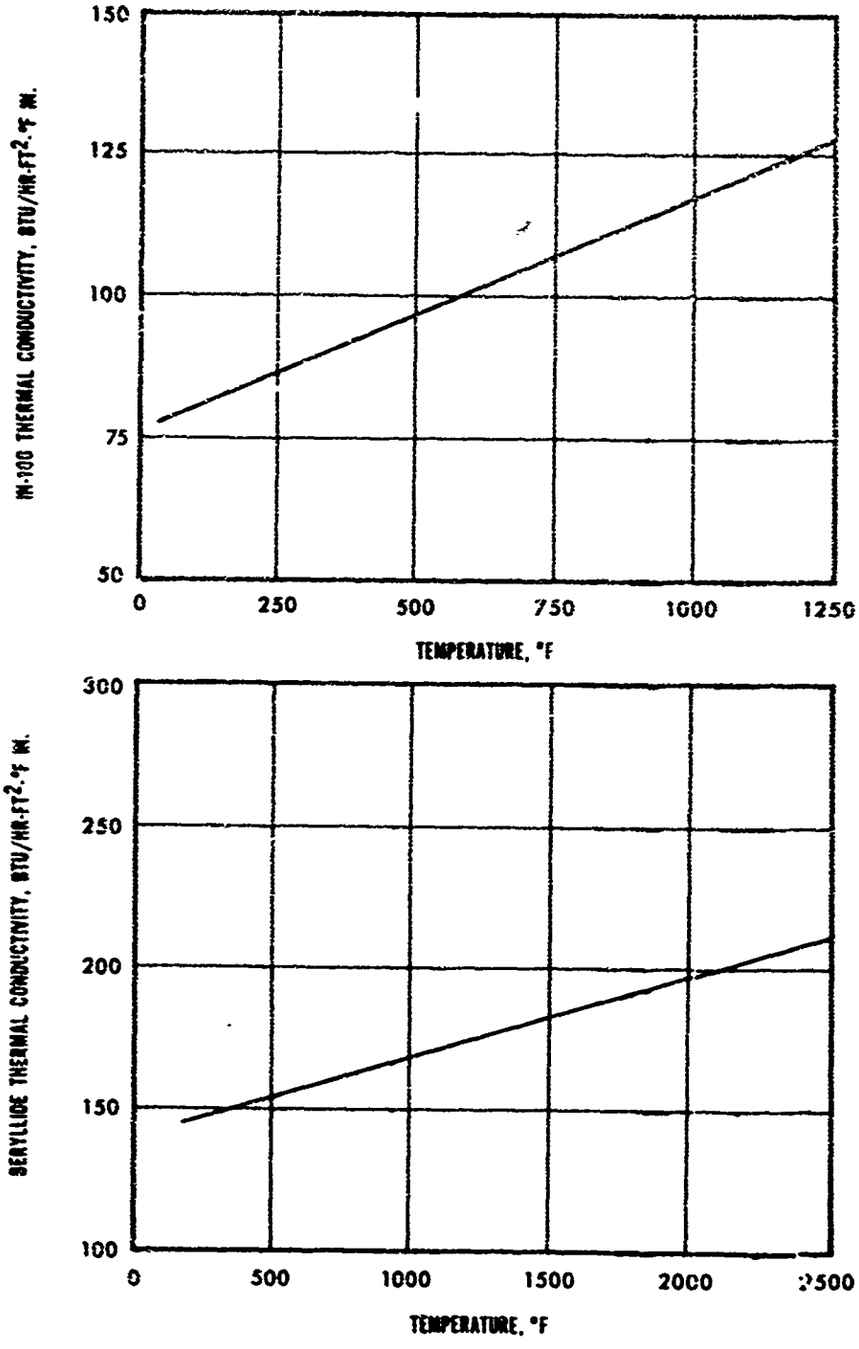

Figure 67. Thermal Conductivity of Beryllide and IN-100.

TABLE XV. COMPARISON OF THERMAL CONTACT RESISTANCE AS MEASURED IN REPORTED TESTS WITH PUBLISHED DATA FOR SURFACES OF APPROXIMATELY SIMILAR RMS VALUES

Material	RMS	Interface Temperature °F	Contact Resistance (Hr-Ft^2-°F/Btu) 1000 psi	2000 psi
Steel/steel*	3-32	180	0.00045	0.00040
Steel/steel*	3-16	600	0.00010	0.00005
Beryllide/IN-100 (avg)	16-24	1100	0.00026	0.00021
IN-100/IN-100	16-24	875	0.00027	0.00023

*Kouwenhoven, W. R., and J. H. Potter, THERMAL RESISTANCE OF METAL CONTACTS, The Welding Journal, Vol. 27, No. 10, October 1948, pp. 515s-520s.

CONDUCTION TEST CONCLUSIONS

The test results indicated that the contact resistance was approximately 50 percent smaller than that estimated and used in the rotor thermal analysis of the final design mechanical studies. However, the estimated contact resistance used for the thermal analysis was so small that further reduction would have had little or no effect on the calculated disk temperatures.

Unclassified
Security Classification

DOCUMENT CONTROL DATA - R & D

(Security classification of title, body of abstract and indexing annotation must be entered when the overall report is classified)

1. ORIGINATING ACTIVITY (Corporate author)

AiResearch Manufacturing Company of Arizona
402 S. 36th Street
Phoenix, Arizona

2a. REPORT SECURITY CLASSIFICATION

Unclassified

2b. GROUP

3. REPORT TITLE

2400°F UNCOOLED TURBINE/MATERIAL PROGRAM
VOLUME II - AERODYNAMIC AND MECHANICAL DESIGN

4. DESCRIPTIVE NOTES (Type of report and inclusive dates)

Final Report

5. AUTHOR(S) (First name, middle initial, last name)

G. E. Lindstrom
J. J. Rebeske
F. Weber

6. REPORT DATE	7a. TOTAL NO. OF PAGES	7b. NO. OF REFS
September 1970	156	3

8a. CONTRACT OR GRANT NO.	9a. ORIGINATOR'S REPORT NUMBER(S)
DA 44-177-AMC-183(T) ✓	USAAVLABS Technical Report 70-32B
b. PROJECT NO. Task 1G162204A01409	
c.	9b. OTHER REPORT NO(S) (Any other numbers that may be assigned this report)
d.	AiResearch GT-8233, Vol. II

10. DISTRIBUTION STATEMENT

This document is subject to special export controls, and each transmittal to foreign governments or foreign nationals may be made only with prior approval of U. S. Army Aviation Materiel Laboratories, Fort Eustis, Virginia 23604.

11. SUPPLEMENTARY NOTES	12. SPONSORING MILITARY ACTIVITY
Volume II of a 3-volume report	U.S. Army Aviation Materiel Laboratories Fort Eustis, Virginia

13. ABSTRACT

This report describes aerodynamic and mechanical design studies conducted to establish the preliminary design of a 2400°F uncooled turbine component. The design activity was conducted concurrently with materials research to define the properties of IN-100 and AiResist 13 and to develop a high-temperature turbine material from intermetallic compositions of beryllide (Volume I). The turbine mechanical design studies were based on estimates of IN-100 and beryllide material properties.

Preliminary design studies were conducted to define a number of aerodynamic designs for efficiency comparisons and blade stress analyses, leading to selection of a candidate turbine design. Preliminary thermal and centrifugal stress analyses were conducted for each disk of the candidate turbine.

The design established for the uncooled turbine was a three-stage axial flow turbine with equal work split among stages. The first- and second-stage blades and vanes were of beryllide material, and the third-stage rotor was to be integrally cast IN-100. Extensive thermal and stress analyses were conducted on first-stage turbine components to evaluate the feasibility of the uncooled turbine design.

The design studies were terminated when it became apparent that the proposed beryllide turbine material lacked sufficient stress-rupture strength for rotor application and did not possess adequate ductility for either stator or rotor application.

DD FORM 1473 REPLACES DD FORM 1473, 1 JAN 64, WHICH IS OBSOLETE FOR ARMY USE.

Unclassified
Security Classification

14. KEY WORDS	LINK A		LINK B		LINK C	
	ROLE	WT	ROLE	WT	ROLE	WT
Uncooled Turbine Design						
Beryllide Turbine Material						